UNIVERSITY OF CALIFORNIA SAN DIEGO

Fabrication and Electromechanics of Piezoelectric Polymer-Ceramic Composite Materials for Wearable Sensing Applications

A dissertation submitted in partial satisfaction of the
requirements for the degree
Doctor of Philosophy

in

Chemical Engineering

by

James Lance Middlebrook

Committee in charge:

Professor Donald J Sirbuly, Chair
Professor Darren J Lipomi, Co-Chair
Professor Shengqiang Cai
Professor Shaochen Chen
Professor James R Friend

2020

The dissertation of James Lance Middlebrook is approved, and it is acceptable in quality and form for publication on microfilm and electronically:

_____

_____

_____

_____
Co-Chair

_____
Chair

University of California San Diego

2020

DEDICATION

To the countless students that I've learned from and grew with over the years - your curiosity and questions are what helped me keep seeking out answers.

TABLE OF CONTENTS

LIST OF FIGURES

ACKNOWLEDGEMENTS

This dissertation would never have been possible without the positivity of the communities that I have found myself surrounded by throughout my life. I would like to extend my unending gratitude to the professors and teachers throughout my life that never ceased to believe in the power of education which inspired me to continue down this path with all of the associated bumps, dips, and unexpected detours. Also they have my appreciation for tolerating my well-intentioned sense of humor even when occasionally mistimed.

I would like to recognize my advisor, Prof. Don Sirbuly, for always asking the questions which brought back the focus to the big picture. Thank you for being endlessly excited to innovate, understand, and execute new ideas. You've promoted a culture of learning, exploration, and support that has lead many of your students down a bright road ahead - we all thank you.

I would also like to thank my committee co-chair Prof. Darren Lipomi and committee members Profs. James Friend, Shaochen Chen, and Shengqiang Cai for your guidance and knowledgeable insight during these final chapters of my graduate career.

The Sirbuly group has been an incredible home to grow intellectually and personally, and I have some of the kindest, well-spirited group members to thank for that. Kanguk Kim, you trailblazer, for setting us down this wild and complicated path. Billy McCall, Cory Heath, Gina La Pierre, and Rohit Subramaniam for believing that compressible foam dreams do come true. Conor Riley, Josh Villanueva, and Qian Huang for each helping tell me how it really is in this world. Yuesong Shi and Beril Polat for your upbeat attitudes and ever entertaining conversations despite the nanowire blues. Spencer Ward whose expert electron wrangling skills along with his steely poker face who has been my intellectual rock throughout these many years - thank you for putting up with me.

The undergraduate researchers that I've been fortunate enough to under my wing throughout my graduate school experience helped craft an atmosphere of discovery (and craft a whole lot of foams). The roles of Yoonhwan Cho, William Wei, Andrew Wan, Stuart Sardo, Andrew Wong, Matthew Levesque, Jeffrey Brodie and Jeffrey Chen were each invaluable in conducting the countless

trials that went into developing our materials and findings. Thank you for listening to my various fun facts, safety talks, and lab report advice.

My collaborators including Wei Zhu, Henry Hwang, and Natalie Lawrence from the Chen lab were instrumental in succeeding in our projects; your outside perspectives and expertise were ever appreciated. Mickie Finn and Sam Edmunds of the Lipomi group, thank you for always being up for talking about the moment's latest. Experiencing the innovation ever present with the NextWave Ventures family, past and present, was an incredible opportunity for me to take part in, and I wish them the best in their pursuits.

I would finally like to thank Terri, Suzie, and my parents who have all been some of my greatest champions, and helping give me the resolve and the guidance (sometimes the same guidance multiple times..) to let me be able to see the path towards a bright future. Your love and caring has shaped me in a way to always strive towards the future while taking the time to live in the present with those around me.

Chapter 2, in full, is a reprint of the material as it appears in ACS Applied Materials & Interfaces 2016. James L. Middlebrook & Kanguk Kim, Jeffrey E. Chen, Wei Zhu, Shaochen Chen, and Donald J. Sirbuly. The dissertation author was the primary investigator and author of this paper.

Chapter 5, in part, is being prepared for submission: Middlebrook, J and Sirbuly, D. *Accessible Piezoelectric Testing Suite for Composite Sensors in Wearable Applications*. The dissertation author was the primary investigator and author of this paper.

Chapter 6, in full, is being prepared for submission: Middlebrook, J, Wei, W., Cho, Y. and Sirbuly, D. *Electrospun polymer-ceramic piezoelectric composite nanofiber mats for sensing applications*. The dissertation author was the primary investigator and author of this paper.

VITA

2014	B.S. in Chemistry, *summa cum laude*, California Polytechnic State University
2017	M.S. in Chemical Engineering, University of California San Diego
2020	Ph.D. in Chemical Engineering, University of California San Diego

PUBLICATIONS

Middlebrook, J., Kim, K., Chen, J., Zhu, W., Chen, S., and Sirbuly, D. "Tunable Surface and Matrix Chemistries in Optically Printed (0–3) Piezoelectric Nanocomposites". *ACS Applied Materials & Interfaces* 2016 8 (49), 33394-33398.

Middlebrook, J., Wei, W., Cho, Y. and Sirbuly, D. "Electrospun polymer-ceramic composite nanofiber mats for piezoelectric sensing applications". *In preparation.*

Middlebrook, J. and Sirbuly, D. "Accessible Piezoelectric Testing Suite for Piezoelectric Composite Sensors for Wearable Applications". *In preparation.*

TEACHING ASSISTANCE

- NANO 120A: Nanoengineering System Design I: *Winter 2020, Winter 2019, Winter 2018*
- NANO 102: Foundations in Nanoengineering: Chemical Principles : *Fall 2019, Fall 2015*
- NANO 201: Foundations of Nanoengineering I: Introduction to NanoEngineering: *Fall 2018*
- CENG 101C: Mass Transfer: *Spring 2016*
- NANO 203: Nanoscale Characterization: *Winter 2016*

ABSTRACT OF THE DISSERTATION

Fabrication and Electromechanics of Piezoelectric Polymer-Ceramic Composite Materials for Wearable Sensing Applications

by

James Lance Middlebrook

Doctor of Philosophy in Chemical Engineering

University of California San Diego, 2020

Professor Donald J Sirbuly, Chair
Professor Darren J Lipomi, Co-Chair

Piezoelectric ceramics, which have the ability to interconvert between mechanical and electrical energies, have been applied for decades in fields such as mechanical sensing, short range actuation, or charge generation. However, the brittle and inflexible nature of these bulk ceramics has made it challenging for these materials to be applied as wearable electronics or flexible sensing technologies. While conventional piezocomposites involve intricate machining, including 'dice-and-filling' methods, these materials still present significant mechanical disadvantages.

This dissertation discusses the creation and study of polymer-ceramic composite materials which are able to be carefully shaped, compressed, or flexed to fit a large range of sensing applications in the wearable sensors space. Several routes that were explored for creating and improving

these materials include optically printed 3D structures with tuned surface and matrix chemistries, compressible foam composite materials, and electrospun nanofiber nonwoven mats. The optically printed piezoelectric composite materials discussed in Chapters 2 and 3 offer us some understanding of the importance in chemically controlling the interface between the piezoelectric components and the matrix. This allows us to innovate and improve a piezoelectric composite foam material by introducing covalent linking between its nanoparticle additives and polymer as discussed in Chapter 4. While the porous foam composites act as effective sensors of impacts and other high-strain events, measuring low-strain interactions, such as heart rate is challenging. Addressing the need for more accessible routes to experimentally assess these types of composite materials and the strains and strain-rates involved in events like breathing, walking, or impact detection, Chapter 5 demonstrates a more accessible, purpose-built characterization suite. Through creating a porous electrospun piezoelectric ceramic-polymer mat device as shown in Chapter 6, we're able to leverage the advantages of a porous, flexible composite while achieving a sensing threshold capable of direct biosensing.

Using these varied morphologies of structures, foams, and mats, we are able to tailor these materials for a given application and begin to understand and overcome the mechanical hurdles found in this emerging composite space.

Chapter 1

Introduction

Piezoelectric ceramics, which have the ability to interconvert between mechanical and electrical energies, have been applied for decades in fields such as mechanical sensing, short range actuation, or charge generation. However, the brittle and inflexible nature of these bulk ceramics has made it challenging for these materials to be applied as wearable electronics or flexible sensing technologies. While conventional piezocomposites involve intricate machining, including 'dice-and-filling' methods, these materials still present significant mechanical disadvantages.

This dissertation discusses the creation and study of polymer-ceramic composite materials which are able to be carefully shaped, compressed, or flexed to fit a large range of sensing applications in the wearable sensors space. Several routes that were explored for creating and improving these materials include optically printed 3D structures with tuned surface and matrix chemistries, compressible foam composite materials, and electrospun nanofiber nonwoven mats. The optically printed piezoelectric composite materials discussed in Chapters 2 and 3 offer us some understanding of the importance in chemically controlling the interface between the piezoelectric components and the matrix. This allows us to innovate and improve a piezoelectric composite foam material by introducing covalent linking between its nanoparticle additives and polymer as discussed in Chapter 4. While the porous foam composites act as effective sensors of impacts and other high-strain events, measuring low-strain interactions, such as heart rate is challenging. Addressing the need

for more accessible routes to experimentally assess these types of composite materials and the strains and strain-rates involved in events like breathing, walking, or impact detection, Chapter 5 demonstrates a more accessible, purpose-built characterization suite. Through creating a porous electrospun piezoelectric ceramic-polymer mat device as shown in Chapter 6, we're able to leverage the advantages of a porous, flexible composite while achieving a sensing threshold capable of direct biosensing.

Using these varied morphologies of structures, foams, and mats, we are able to tailor these materials for a given application and begin to understand and overcome the mechanical hurdles found in this emerging composite space.

1.1 Piezoelectric Effect

The piezoelectric effect can be summarized as the ability for a material to be able to interconvert between mechanical strain and an electrical polarization. Found to occur even in common materials such as bone [1] and quartz [2], piezoelectric materials utilize this effect to act as balances such as in a quartz crystal microbalance [3], generate a spark via an ignitor on a stovetop [4], or even perform ultrasound as the electroceramic in an ultrasound wand [5]. Piezoelectric materials have in common a lack of inversion center or not having a center of symmetry in their material unit cell as well as being dielectric materials. When they are mechanically strained, this lack of symmetry causes an asymmetric charge distribution to occur, with one part of the unit cell being more positive, and the other side more negative, generating a dipole and an electric field - an example of the direct piezoelectric effect. In contrast for a symmetric material, a mechanical strain would lead to a more or less charge dense material, but no change in the polarity of the material. The converse piezoelectric effect takes place when an electric field is able to cause a mechanical deformation across a piezoelectric material. Examples of the barium titanate neutral unit cell and polarized unit cell can be seen in Figure 1.1.

Piezoelectric sensors operate via the piezoelectric effect where a stress on the material is

able to create a polarization which is collected at and sensed through electrodes. For all elastic materials, a stress, T_i, will cause a strain, S_i, in a material as related by the elastic compliance, s_{ij} (Equation 1.1). As strain and stress are symmetric tensors and as a convention, Voigt notation is used to show the contracted matrix forms of the following relations rather than the higher order tensors.

$$S_i = s_{ij} * T_i \tag{1.1}$$

In piezoelectric materials, this stress is also able to generate an polarization electric charge on the material, a dielectric displacement, D, due to a material's lack of center of symmetry. This can be related to the stress through the piezoelectric charge coefficient, d_{ij} (Equation 1.2), with units of coulombs/Newton, where *i* refers to the axis of stress applcation (e.g. x, y, or z principle axes) and *j* refers to the axis of polarization or alignment of the piezoelectric material. The d_{33} value can be referred to as the longitudinal piezoelectric charge coefficient and d_{31} can be referred to as the transverse piezoelectric charge coefficient [6].

$$D_i = d_{ij} * T_i \tag{1.2}$$

Piezoelectric materials are also capable of the converse piezoelectric effect where strain, S_i , can also be generated by an applied electric field, E_i , also related by piezoelectric charge coefficient, d_{ij}, with the alternative units of meters/volt (Equation 1.3).

$$S_i = d_{ij} * E_i \tag{1.3}$$

As the mechanical and electrical properties of these materials are interconnected, we can combine Equations 1.2 and 1.3 to yield the general equations of state which describe tensor relationship that couple strain, stress, electric field, electric displacement (Equations 1.4 and 1.5) where the superscription of stress or electric field represents the holding of those values constant

[7]:

$$D_i = d_{ij} * T_i + \varepsilon_{ij}^T * E_i \tag{1.4}$$

$$S_i = s_{ij}^E * T_i + d_{ij} * E_i \tag{1.5}$$

While the piezoelectric charge coefficient, d_{ij} is useful for comparing materials, especially those meant to actuate, the piezoelectric voltage coefficient, g, can be useful for describing materials' ability to generate voltage, though is less often presented. The piezoelectric charge and voltage coefficients are related by the relative permittivity of the material, K, as shown in Equation 1.6, with ε_0 representing the permittivity of free space:

$$g_{ij} = d_{ij}/(K * \varepsilon_0) \tag{1.6}$$

These relations serve as the basis from which we can begin developing piezoelectric composite sensors and devices. In the next sections, how these coefficients arise and can be manipulated in materials and composites will be covered.

1.2 Piezoelectric Materials & Composites

Industrially and in the research field, the majority of piezoelectric materials are crystalline such as single-crystal lead magnesium niobate/lead titanate (PMN-PT) [8] or the polycrystalline domained lead zirconate titanate (PZT). As mentioned, a unifying property of piezoelectric materials is their lack of centrosymmetry while allows for a polarization of the unit cell in response to strain as well as the converse. Crystalline materials can be organized by their Bravais lattice, crystal system, and crystallographic point groups into thirty-two crystal classes [9]. Piezoelectric, ferroelectrics, and pyroelectric properties are given rise due to the lack of inversion center for several of those groups as well as the symmetry levied by the varied point groups of symmetry [10].

Mixed ceramics or polycrystalline materials like PZT or barium titanate (BTO) do not have any long range symmetry as created, even if their individual Perovskite unit cells are in the

piezoelectrically active tetragonal phase. The individual crystal domains are piezoelectric, but the effect is canceled out by the randomly oriented neighboring crystals that are just as likely to negate the effect as reinforce. These crystal domains can be reoriented along to realign their polar axes to work together in a process known as poling or polarization. By heating the ceramics close to their Curie temperature and applying an electric field comparable to a material's coersive field, the ferroelectric domains can shift to align their polar axes with the direction of the electric field.

Piezoelectric composites and multiphase solids can be described by the interconnectivity of their constituents as described in detail by Newnham [11]. In the scope of this work, (0-3), (0-3)*, and (3-3) composites are generated and studied. In Chapters 2 and 3, the optically printed nanocomposites contains individual nanoparticles fully encapsulated by a matrix material (0) with full connectivity to all sides (3), a 0-3 composite. In Chapters 3 and 4, the compressible foam composite material contains individual nanoparticles encapsulated by a matrix material (0) along with gas filled void areas encapsulated by a matrix material (0) with full connectivity to all sides (3), a (0-3)* composite. While the compressible foam composite is triphasic and could be more accurate described with a triphasic notation, it is common to abbreviate it as a (0-3) composite as the additives and voids have no repeating connectivity individually or to other. In Chapter 6, electrospun nanofiber non-woven mats are maintained as a interconnected three-dimensional sheet (3) with an adhesive with full connectivity to the mats and electrodes (3), a 3-3 composite.

While each component of a composite material is able to have its own properties such as dielectric constant, piezoelectric charge coefficient, or Young's Modulus, the overall composite may have values somewhere in between in the case of independent properties such as dielectric constant, K, known as summed effects. For other values like piezoelectric charge constant, g, which are dependent on each component's dielectric constant and piezoelectric charge coefficient, the combined property can be enhanced, a combination effect. This can be shown as described by Newnham for a (3-1) two-phase composite of a hard piezoelectric electroceramic at a 10% volumetric fraction, ^{2}V, (represented by phase superscript 2) and a softer polymer at a 90% volumetric fraction, ^{1}V, (represented by phase superscript 1), the piezoelectric voltage coefficient, g_{33} can be described with

Equation 1.7 [11]:

$$g_{33} = \frac{E_3}{\sigma_3} = \frac{d_{33}}{\varepsilon_3} = \frac{{}^1V\,{}^1d_{33}^2 s_{33} + {}^2V\,{}^2d_{33}^1 s_{33}}{({}^1V\,{}^2 s_{33} + {}^2V\,{}^1 s_{33}) * ({}^1V\,{}^1\varepsilon_{33} + {}^2V\,{}^2\varepsilon_{33})} \tag{1.7}$$

Simplifying based on comparing the materials' piezoelectric charge coefficient ${}^1d_{33} >>^2 d_{33}$, elastic compliance ${}^1s_{33} <<^2 s_{33}$, and electric permittivity ${}^1\varepsilon_{33} >>^2 \varepsilon_{33}$, we reach Equation 1.8:

$$g_{33} =^1 d_{33}/({}^1V *^1 \varepsilon_3) =^1 g_{33}/({}^1V) \tag{1.8}$$

The low volumetric fraction of the piezoelectric electroceramic causes the composite's g_{33} to be enhanced 10x compared to the ceramic alone exemplifying the ability for composites to concentrate stress.

While the above example was for a (1-3) composite, this effect is still present in (0-3) composites such as those as the optically printed piezoelectric composites of Chapters 2 and 3 as well as the compressible foam piezoelectric composites of Chapter 4 and 5. A similar direct evaluation of (0-3) composites is less straight forward due to the unique ordering and interactions that can occur between the various components of the material. As will be shown in Chapter 2, the intermolecular bonding, or lack there of, can have a large impact on the piezoelectric properties of the bulk material, even at the same volumetric percentages of each component. More complicated composites such as the foam-based compressible piezoelectric materials can also be challenging to evaluate theoretically as the presence of polymer, voids, piezoelectric material, and other additives with less controlled geometries leads to many of these materials' research being driven more experimentally than bulk piezoelectric ceramics or dice-and-fill composites.

Composites of porous ferroelectric materials also show a strong departure from their bulk counterparts in terms of their remanent polarizations, saturation polarizations, and coercive fields. For porous barium titanate ceramic materials created through a pollen templating method, a porosity of 50% caused a three fold decrease in the remanent and saturation polarizations and three-fold increase in the coercive field from 2.3 kV/cm to 7.2 kV/cm [12]. While the piezoelectric charge or

voltage coefficients were not evaluated in that work, the increase in porosity also caused a decrease in the dielectric constant due to the lower loading of barium titanate, a highly dielectric material, per volume.

The field of piezoelectric polymers also can include amorphous, semi-crystalline, and void charged polymers [13]. In addition to the aforementioned morphologies, many techniques and methods have been developed to a wide range of geometries and connectivities in piezoelectric materials. With the growing popularity of techniques such as electrospinning to cast polymers and composites, the materials toolkit has expanded rapidly to include materials such as polyurethanes, polylactic acid, collagen, and polystyrene [14, 15] which could be used as a matrix material. Piezoelectric materials such as poly(vinylidene fluoride) (PVDF), barium titanate composite nanofibers, and lead zirconate titanate composite nanofibers can also be directly electrospun as a 1D material [16, 17, 18]. Freeze casting can also be used to created a (2-2) connectivity lead zirconate titanate material [19]. As the ability to create, cast, or spin materials improves, so too will the ability to create these piezoelectric composite materials.

1.3 Modeling Piezoelectric Composites

The sometimes complex composition, geometries, and resulting electromechanical properties of piezoelectric composites can make modeling materials like the (0-3) optically printed structures of Chapters 2 and 3, the compressible foams of Chapters 4 and 5, and the electrospun materials of Chapter 6 challenging. This is in part due to the use of bulk properties whereas the properties of nanoparticle electroceramics and their nanocrystalline domains may deviate [20]. While models still need do not fully consider the role of surface modification can play in the transfer of stress through a composite [21, 22]. Insights into the design and function of these materials can still be made, however, from the existing models.

Moody *et al*. proposed a model for polyurethane foams which had been molecularly-doped with high dipole molecules such as 2-chloro-4-nitroaniline, benzoic acid, and 2-bromo-6-

methoxynapthalene [23]. Their approach a constant total aligned dipole moment that would polarize a bulk material as it compressed. By treating each polar dopant molecule as a dipole that collects charge at the electrodes in response to strain, this model treats the system similar to a piezoelectric electret [24]. This work yielded materials that had piezoelectric charge coefficients, d_{33}, as high as 244 ± 30 pC/N though as the small molecule dopants were free to rotate in the matrix, the material's piezoresponse decreased by over 80% in less than forty-eight hours.

Persano *et al.* created electrospun poly(vinylidenefluoride-*co*-trifluoroethylene) [P(VDF-TrFE)] aligned nanofibers and fabricated them into a piezoelectric sensor which was compared with a transverse piezoelectric analytical model [16]. By considering the relevant elastic (c_{ij}), piezoelectric (e_{ij}), and dielectric (k_{ij}) constants for the array of one-dimension nanowires, the voltage generated by the nanofiber array could be show as follows in Equation 1.9:

$$V = \frac{\bar{d}}{\bar{k}} * L_{eff} * p \tag{1.9}$$

where $\bar{d} = e_{31}/c_{11}$, $\bar{k} = k_{33} + e_{31}^2$, and p is pressure. $\bar{d}/\bar{k}$ at a value of 0.14 V*m/N was found to allow for the model to agree with experimental data though the elastic, piezoelectric, and dielectric constants were not measured.

Furukawa *et al.* proposed a model for (0-3) piezoelectric composites, or as they describe a two phase system with piezoelectric spherical inclusions [25, 26]. One of their results is the modeling of a composite material's piezoelectric charge coefficient, d, as a function of the volumetric percentage of piezoelectric component, ϕ, that material's piezoelectric charge coefficient, d_2, and the local field, ε, and stress, c, coefficients as shown in Equation 1.10. The inactive phase is presented by a 1 subscript while the active, piezoelectric component is represented by a 2 subscript.

$$d = \phi * \frac{5c_2}{(3c_1 + 2c_2 - 3\phi(c_1 - c_2)} * \frac{3\varepsilon_1}{(2\varepsilon_1 + c_2 - \phi(\varepsilon_1 - \varepsilon_2)} E * d_2 \tag{1.10}$$

While the Furukawa model is effective for dilutely dispersed coefficients in an incompressible material, another model proposed Wong et al. expands this work by being able to consider

composites with higher loading by considering the interactions between piezoelectric inclusions [27].

1.4 Piezoelectric Device Characterizations

In a wearable piezoelectric sensor, the main measurand is typically a voltage or charge output. The piezoelectric composites of this work had their piezoresponse measured directly or via a charge amplification circuit in response to an applied stress by a droptest or a voice coil linear actuator.

The impact sensing abilities of the devices presented in this work were measured by a purpose-built droptest setup or with a voice coil linear actuator setup. A drop tower was constructed that allowed the sample to be suspended between insulating layers of acrylic below a weighted droprod. A prestraining force (2 N) was used to keep the stack in full contact. The open circuit voltage output was monitored via a digital oscilloscope (Rigol, DS1054Z) or a digital acquisition unit (DAQ, National Instruments, USB-6212). The electrode opposite the impact (bottom electrode) was the monitored lead and the impacted electrode (top electrode) being the reference. The input peak force and force during the collision event was monitored by a piezoresistive sensor and circuit (Tekscan FlexiForce A201-1 Sensor, FlexiForce Quickstart Board) monitored by a digital oscilloscope (Rigol DS1054Z). A schematic of these measurement setups can be seen in Figures 1.2 and 1.3.

The piezoelectric charge generation ability of the devices was measured in a quasi-static method by a purpose-built charge amplifier and linear actuator setup. The charge amplifier uses a high inner gain and insulation resistance to yield a voltage output proportional to the charge generated by the device. The device was centered below the linear actuator and suspended between insulating layers of acrylic. A prestraining force (2 N) was used to keep the stack in full contact. Forces were applied by the sinusoidally oscillating linear actuator in tests that ranged between 1-5 N in force. The input peak force and force during the collision event was monitored by a piezoresistive

sensor and circuit (Tekscan FlexiForce A201-1 Sensor, FlexiForce Quickstart Board) monitored by a digital oscilloscope (Rigol DS1054Z). The charge-force relationship was calibrated against a known barium titanate ceramic (140 pC/N, Steminc, SMD18T2M511LF) and used to determine the piezoelectric charge coefficient of the sample. A schematic of this measurement setup can be seen in Figure 1.3. The charge amplifier circuit can be seen in Figure 1.4.

1.5 Wearable Sensors and Applications

Composite piezoelectric materials, once fabricated into devices, can be used for many applications including sensing, power generation, actuation [28, 29, 30]. By combining the sensing potential of piezoelectric charge generating materials with higher flexibility, compressibility, or strainability, the applications can be extended into realms that can help better inform ourselves to our world and our interactions with it. While the piezoelectric effect can be an ideal sensing solution for many situations, there are other sensing methods with similar capabilities and well as their own advantages such as piezoresistive sensors, capacitive strain sensors, and triboelectric sensors. Piezoresistive sensors use an external power source to monitor for changes in a material's resistance in response to force and have been used to monitor bodily motion and blood pressure [31, 32, 33, 34]. Capacitive strain sensors, which also use an external power source, are monitored for changes in the capacitance of the material and can be used for monitoring muscle movement and as a humidity sensor [35, 36]. Triboelectric sensors rely on differing materials' affinities for contact electrification where friction is able to mediate the charge transfer which has allowed them to be utilized as self-powered tactile sensors and respiration detection [37, 38].

Compared to these other sensing modes, piezoelectric sensors have the advantage of being self-powered via the piezoelectric direct effect. Triboelectric sensors also do not require external powering, but the friction and oftentimes contact separation mediated effect may be challenging to accommodate in many sensing scenarios. Not only are piezoelectric devices self-powered, but the direct effect also allowed them to act as power generators. This can be described by the

electromechanical coupling factor, k, as seen in Equation 1.11:

$$k^2 = \frac{\text{mechanical energy converted to electrical energy}}{\text{input mechanical energy}} \tag{1.11}$$

It is possible to improve the power generation capabilities of piezoelectric composites by incorporating other charge transfer events such as triboelectricity. The generated currents can be increased by several magnitudes, into the microwatt range, to create a micro or nanogenerator [39]. While the electrical power generation can has improve substantially by incorporating triboelectric contributions, the device now requires mechanical separation and re-engagement or friction required may lead to an accelerated aging or shorter device life span, a disadvantage of triboelectric devices.

While the piezoelectric component of these composites can be made from many electroceramics including lead zirconate titanate ($PbZr_{1-x}Ti_xO_3$,PZT) and barium titanate ($BaTiO_3$, BTO), BTO is offered preferred in wearable sensors due its improved biocompatibility compared to the toxic, lead-containing PZT despite BTO's typically lower piezoelectric performance [40, 41].

1.6 Outline of the Dissertation

In this thesis, we introduced in Chapter 1 the goals behind creating composite piezoelectric devices, what gives rise to the piezoelectric effect, how a composite can alter the electromechanics of the material, as well as some of the applications and obstacles to these devices. In Chapter 2, we will take a look at how the polymer component and interfacial chemistries can be tuned in optically printed polymer-ceramic composite materials in order to improve and tune device electromechanics. Parameters such as nanoparticle size, linker molecule, and matrix stiffness create a variety of different combinations of device robustness and electrical output. In Chapter 3, these optically printed materials are used in the unique application of being evaluated as a took to help study the interactions between the human body and a space suit as a sensing layer in the lining of the suit. In Chapter 4, the progression of foam-type piezoelectric polymer-ceramic composite materials is explored from foundational works using a silicone matrix to a newer generation of

polyurethane based materials with advantages in performance and processability. In Chapter 5, we will explore the challenges and solutions to creating and characterizing composite materials in this space. A more accessible characterization suite has been developed and is discussed here that allows for the more rapid development and assessment of these devices ability to react to strain rates and forces as well as their ability to create voltage and charge. In Chapter 6, an electrospun piezoelectric ceramic-polymer composite nonwoven mat is developed that is able to begin sensing not only high-strain rate events similar to its foam-based cousins, but also minute events such as the human heart rate. The ability for these mats to act as a scaffold for other enhancing additives is also assessed.

1.7 Figures

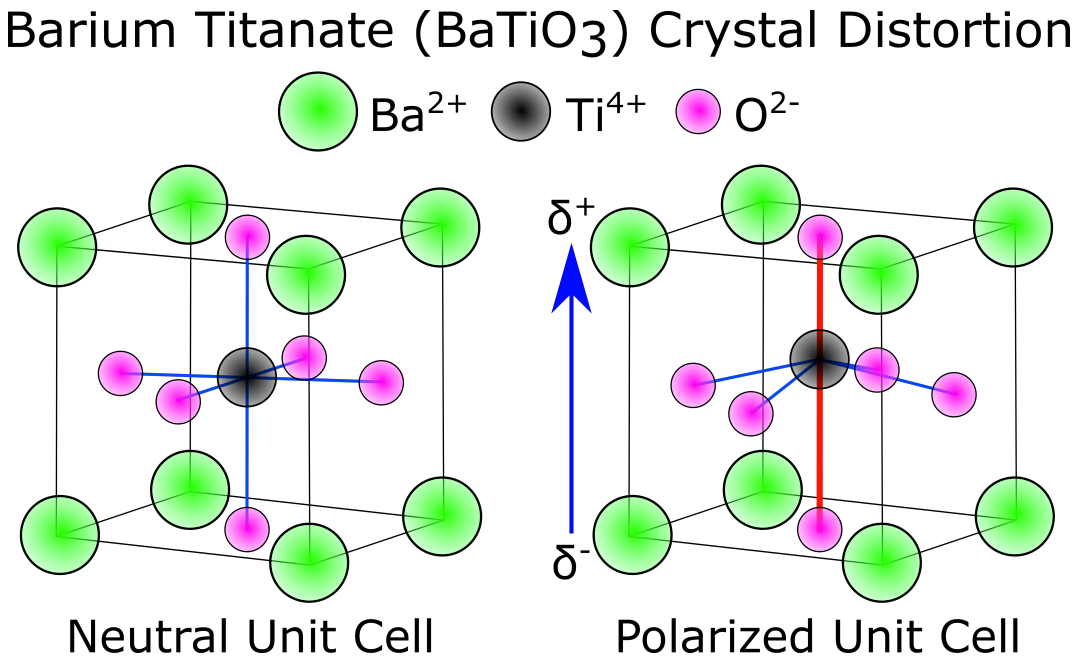

Figure 1.1: *Barium Titanate Unit Cells and Crystal Distortion*
The cubic, neutral phase of barium titanate (left) and the elongated tetragonal phase (right). The polar axis of the tetragonal phase is highlighted in red along with the resulting polarization of the unit cell in blue.

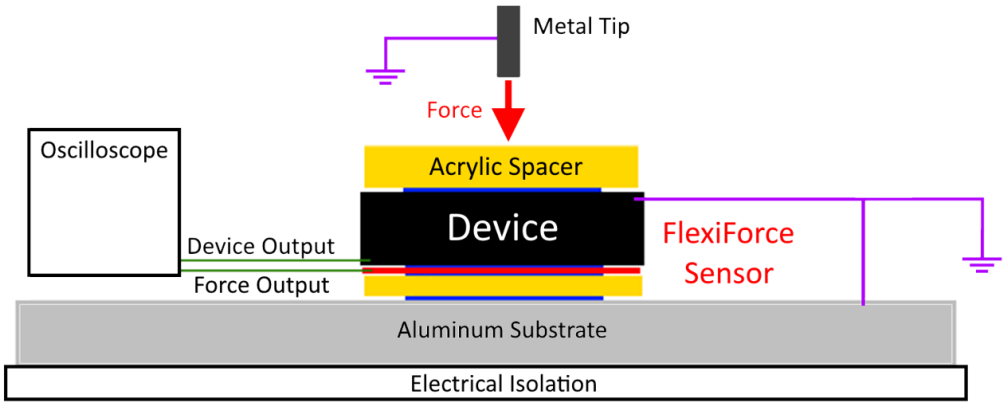

Figure 1.2: *Droptest Measurement Schematic*
A schematic of the droptest setup used to measure impact forces and device output in response to impact forces. FlexiForce Sensor was made up of a Tekscan FlexiForce A201-1 Sensor and a FlexiForce Quickstart Board with both the force measurement as well as the device voltage output monitored by a Rigol DS1054Z digital oscilloscope.

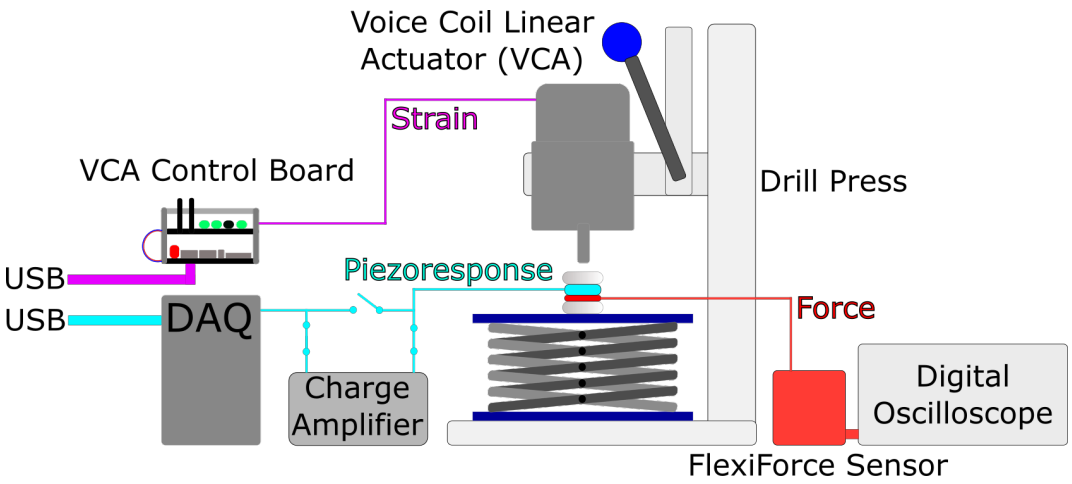

Figure 1.3: *Voice coil linear actuator based piezoelectric testing suite*
A voice coil linear actuator seated rigidly in a drill press stand with variable height is suspended over a laboratory scissors jack testbed. A test-stack of an acrylic spacer, piezoresistive force sensor, piezoelectric sample of interest, and acrylic spacer is held together in intimate contact with a pre-straining force under the voice coil linear actuator. The piezoresponse of the sample is send to a charge amplifier then a digital acquisition unit (DAQ) for piezoelectric charge measurements or directly to the DAQ for voltage measurements. Force measurements are taken by a FlexiForce A201-1 sensor coupled to a FlexiForce Quickstart board monitored by a digital oscilloscope. Positional data on the voice coil linear actuator is collected by its control board in order to provide information on position, stain, velocity, and strain-rate throughout the interaction.

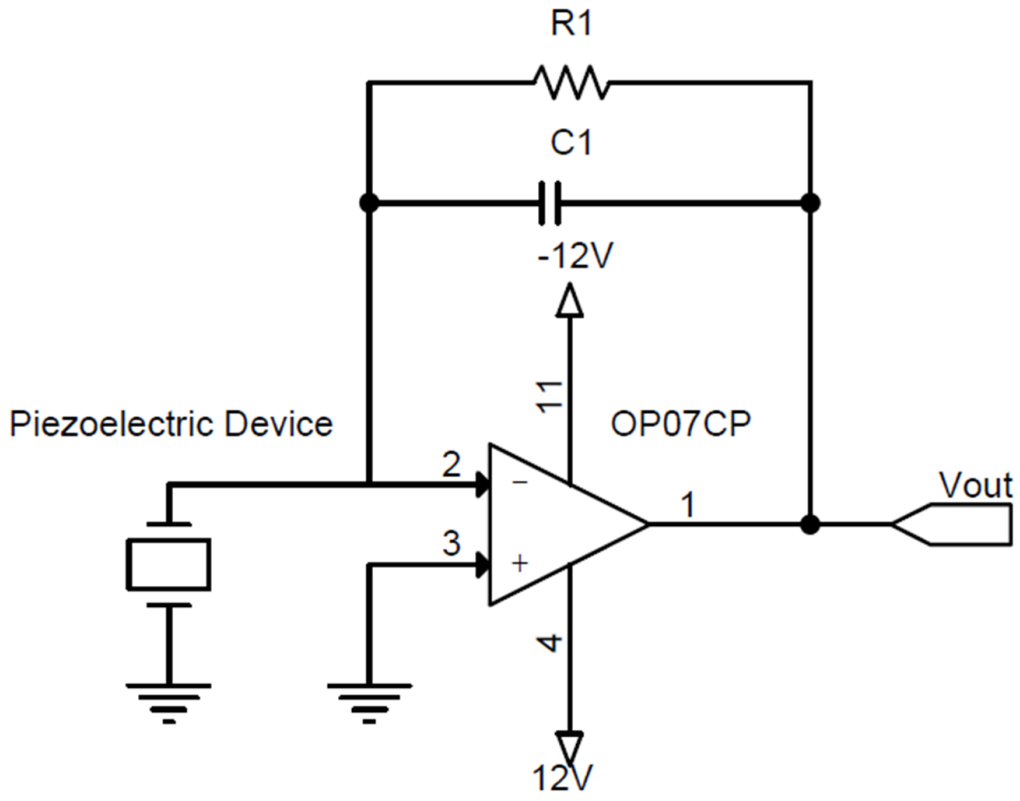

Figure 1.4: *Schematic of a Charge Amplifier Circuit*
Charge amplfier circuit for collecting a piezoelectric device's charge output on the circuit's capacitor, C1 = 100 pF. The circuit's resistor, R1 = 20M■, results in a RC time constant for the circuit, τ, of 2 ms and a cutoff frequency, $f_c = (2\pi\tau)^{-1}$ = 79.6 Hz.

Chapter 2

Tunable Surface and Matrix Chemistries in Optically Printed (0–3) Piezoelectric Nanocomposites

2.1 Introduction

In this work, the impacts of varying surface modification, matrix parameters, and fabrication conditions on the performance of optically printed (0-3) piezoelectric polymer nanocomposites are examined. For example, we find that a 75% reduction in nanoparticle edge-length boosted the piezoelectric coefficient (d_{33}) by over 100%. By optimizing the composition and fabrication conditions, 10% by mass loading barium titanate nanocomposites are able to yield d33 values of $\sim$ 80 pC/N compared to $<$ 5 pC/N when parameters are not optimized. With a more complete understanding of how to enhance the performance of (0-3) piezoelectric polymer nanocomposites, these materials should find use in a wide range of applications.

Piezoelectric materials and their ability to couple mechanical and electrical energy forms have played important roles in applications such as nanogenerators [42, 43]), sensors [44, 45], and ultrasonic transducers [46, 47]. Conventional inorganic piezoelectric materials such as lead zirconate

titanate (PZT) are most commonly used in the form of large, bulk electroceramics due to their high piezoelectric coefficients.7 However, this bulk electroceramic implementation restricts these materials' applications due to inherent limitations such as poor mechanical flexibility, brittleness [48, 49, 50], and in the case of PZT, the presence of lead which limits biological applications [40]. Piezoelectric polymers, such as polyvinylidene fluoride (PVDF), have been proposed as candidates to help circumvent these issues, but their piezoelectric coefficients are typically an order of magnitude less than that of ceramic-based piezoelectric materials [51]. While both ceramic and polymer piezoelectrics have their advantages and disadvantages, piezoelectric nanocomposites have garnered significant attention as an alternative material that bridges the gap between bulk electroceramics and pure polymer piezoelectrics by providing moderate piezoelectric coefficients while retaining mechanical flexibility and biocompatibility. These nanocomposites typically take the form of one-dimensional piezoelectric ceramics such as nanowires or rods embedded in a polymer matrix, known as a (1-3) composite [13, 52], or nanoparticles suspended in a matrix, a (0-3) composite [53, 54, 55, 56]. As the potential for these composite materials grows to fill this void in modern piezoelectrics, it is important to explore the ability to control the ceramic-polymer interface and the effects from changing the properties of the polymer matrix [57, 58].

In previous work we demonstrated that piezoelectric (0-3) nanoparticle-polymer composite materials could be optically printed in three dimensions (3D) using barium titanate (BT) nanoparticles suspended in a photoliable polymer solution [59]. Through the use of a digital projection printing (DPP) method, we were able to selectively crosslink regions of the solution using ultraviolet (UV) light and a photopolymerizable polymer such as poly(ethylene glycol diacrylate) (PEGDA). As the polymer crosslinks under light exposure, the BT nanoparticles are encased in the matrix, allowing feature sizes as a small as 5 μm to be reproducibly fabricated. It was also demonstrated that grafting acrylate containing surface groups, such as 3-(trimethoxysilyl)propyl methacrylate (TMSPM), onto the BT enhanced the stress-transfer efficiency by an order of magnitude [59]. These linkers are a critical component to understanding how to tune the performance of piezoelectric nanocomposites since they significantly increase the inorganic-polymer interfacial interaction. In

this work, we examine a wide parameter space, including different linker molecules, changes in the polymer's molecular weight, microstructure size, and nanoparticle size, to obtain a more complete understanding on how to better engineer piezoelectric polymer nanocomposites. While the BT-PEDGA system is studied here, the findings should be universal for other nanoparticle-photopolymer systems.

2.2 Linker Molecules

There is a strong relationship between the piezoelectric output of optically printed composite materials and the piezoelectric nanoparticles' ability to mechanically couple to the matrix. Larger electrical outputs are the result of a stronger interaction between the active piezoelectric crystal and the stresses acting on the polymer. As previously shown, the presence of the TMSPM linker group on the BT nanoparticle surface is far more effective in producing a piezoelectric output compared to unmodified nanoparticles entrapped in a pure polymer matrix or even a nanocomposite doped with carbon nanotubes to enhance the mechanical properties. In order to better understand the role of these chemical linker molecules in transferring mechanical stress, TMSPM modified particle composites were compared against composites containing particles functionalized with linker variants, 3-(trimethoxysilyl)methyl methacrylate (TMSMM) and 3-(methoxydimethylsilyl)propyl methacrylate (MSPM) (Figure 2.1a). These variants were chosen to closely mimic the chemical nature of TMSPM, but alter the number of silyl ether (Si-O-R) groups, which act as binding sites to the nanoparticles. or shorten the central carbon chain, which influences the degrees of freedom between the BT and the polymer matrix. In addition, the impact of polymer stiffness was examined by changing its molecular weight. Polymers such as PEG have been shown to become stiffer as the molecular weight is decreased [60].

In order to test the piezoelectric properties of the nanocomposites with various linker molecules and polymer molecular weights, linker-modified BT piezoelectric nanoparticles were incorporated into PEGDA composite thin film devices. The composites were fabricated with each of

the different linkers (TMSPM, MSPM, TMSMM) as well as with varied PEGDA molecular weights. The materials' piezoelectric charge coefficient (d_{33} – which measures the induced polarization along the 3 direction parallel to the polarized axis while the stress is applied along the same axis) were then measured through an in-house built quasi-static d_{33} meter (data summarized in Figure 2.1b). A schematic for the force sensor circuit used to measure forces simultaneously with the electrical outputs can be found in Figure 2.8. Both MSPM and TMSMM functionalized composites exhibit lower piezoelectric coefficients compared to those modified with TMSPM despite the subtle differences in the molecular structures of the linkers. The role of the linker molecules is to form strong links between the matrix and the piezoelectric nanoparticle, and the small differences between the linker molecules can lead to variations in the stress-transfer efficiency. In the case of TMSMM, the shorter central carbon chain places the acrylate group in closer proximity to the silyl binding sites where the nanoparticle is linked. This pulls electron density away from the Si-O-BT bonds resulting in a lower bond strength; translating to a lessened ability to efficiently transfer mechanical stress from the polymer matrix to the piezoelectric ceramic and a lowered piezoelectric coefficient. For MSPM, the reduction in the number of silyl ether groups produces a weaker linkage between the BT nanoparticle and polymer matrix thus also lowering the mechanical-to-electrical energy conversion efficiency. Surprisingly, there is nearly a 3x enhancement observed in the piezoelectric coefficient for the lowest polymer molecular weight. Atomic force microscopy measurements show that the stiffness of the PEGDA increases from 252 MPa for the 750 Da polymer to 3.74 GPa for the 258 Da polymer. Increasing the polymer stiffness reduces the mismatch in hardness between the nanoparticle and polymer. This translates to a matrix that can transfer more of the applied stress to the piezoelectric nanoparticles by reducing the number of unproductive deformation modes (e.g., polymer expansion orthogonal to the applied stress) found in softer matrices.

2.3 3D Printed Microstructure Effects

While there is a strong piezoelectric dependence on chemical factors, other parameters such as the size and shape of the 3D printed microstructures can also influence the piezoelectric response. For example, the area fraction of the piezoelectric polymer in the printed materials can be controlled by tuning the light exposure (Figure 2.2). Using the same optical mask such as a honeycomb pattern, multiple structure variations can be constructed by increasing the UV exposure time. For example, the honeycomb linewidth can be increased by $\sim 40\%$ by lengthening the UV exposure from 1.0 seconds to 1.6 seconds. This slight change in the area fraction results in a $\sim 67\%$ decrease in the d_{33} value. All of these hexagonal arrays were printed using the 256 Da PEGDA, but similar trends were observed for the other nanocomposites. The drop in the mechanical-to-electrical energy conversion efficiency for the larger area fractions is likely caused by an increase in the effective elastic modulus. Although the exact same composite is being used, the microstructure of the additionally exposed patterns is less capable of transferring stress to the entrapped nanoparticles and therefore shows a lower charge coefficient compared to the lower area fraction structures. This could be due to the increase in active area or an increase in the crosslink density in the region. It is important to note that the amount of charge generated by the printed films under a load is directly related to the strain rate and the rate of charge-loss in the composite. Therefore, a higher strain rate will produce a larger amount of charge on the surface of the piezoelectric given that the samples being compared have the same rate of charge-loss. This effect is observed in the printed microstructures by reducing the amount of active material in the array.

2.4 Nanoparticle Size Effects

One of the major challenges for optically printing structures with small feature sizes, yet a large volume (e.g., thicker), is creating pre-polymerized composite solutions that have high optical transparencies. The PEGDA, or other photocurable polymers, have fairly low absorption coefficients; however, the BT nanoparticles can significantly attenuate light propagation through

the composite due to large optical scattering and/or absorption. These light-matter interactions can distort the optical image and cause aberrations in the printed structures past depths of ~ 300 μm when an above exposure method (i.e., light has to penetrate previously printed regions to access the new layer being printed) is used. While other exposure methods such as extruding the structure away from the light source can be used to circumvent this issue, the light-matter interactions can be mitigated through the composition of the composite. Lower mass loadings ($< 10\%$) are required to achieve adequate optical transparencies with the 80 nm nanoparticles, which limits the amount of active piezoelectric particles that can be used and thus the piezoelectric properties. However, the implementation of smaller BT nanoparticles reduces light-matter interactions to allow higher mass loadings while retaining the optical transparency required for printing. In addition, smaller nanoparticles enhance the interfacial area between the BT and the polymer matrix, which should also contribute to a more efficient stress-transfer efficiency. To investigate the effects from nanoparticle size we compared the optical properties of composites made with 80 and 20 nm edge-lengths (Figure 2.3a). From the transmission experiments it is clear that there is nearly a 7x decrease in the extinction (at 365 nm) going from a printed film loaded with 10% of the larger nanoparticles to the same mass loading with the smaller nanoparticles. In fact, there is only about a 5% drop in the transmittance when a pure PEGDA film is loaded with 1% of the small nanoparticles compared to a $\sim$30% drop with the 80 nm nanoparticles. The maximum spatial resolution that can be achieved with the system is $\sim$1 μm using the pure PEGDA. This requires a transmittance at 365 nm of $> 65\%$ which is only achievable with the smaller nanoparticles. If high spatial resolution is required with the composites, along with larger BT loadings, photoinitiators with longer wavelength absorptions maxima (> 500 nm) can be used.

Testing the piezoelectric performance of the smaller nanoparticle composites showed an immediate trend with the smaller nanoparticles outperforming the larger nanoparticles for every mass loading tested (Figure 2.3b). All materials were poled under the same conditions (10.2 MV/m at 135°C for 4 hours), had identical thicknesses (25 μm), and similar electrode designs. An enhancement of $\sim$100% is observed for the 20 nm particle composite loaded at 10%, which implies

there are contributions from surface area and the number of grafting sites per unit volume. When the charge coefficient is plotted versus the log of the BT surface area per volume of composite (Figure 2.3c), there is a clear indication that the matrix-nanoparticle interfacial area is one of the most significant parameters that influences the piezoelectric performance. The materials tested with a 0.5% mass loading of 80 nm nanoparticles did not show any measurable signals suggesting that a surface area to unit volume ratio of 0.2 μm-1 is the threshold for area per unit volume. piezoelectric behavior in these composites. While the piezoelectric coefficients do increase with larger mass loading percentages, it is expected that the logarithmic trend ceases at higher mass loadings due to larger particle-particle interactions which limits the nanoparticle-polymer interactions and lowers the stress-transfer efficiency. In addition, successfully printing films with larger mass loadings is difficult due to the increased optical scattering and absorption which prevents complete photocrosslinking. Understanding and optimizing these nano-interfacial effects is critical for pushing the performance limits of piezoelectric polymer nanocomposites, and optical printing should play a major role in advancing these materials.

2.5 Conclusions

In this work, we have demonstrated that the piezoelectric performance of optically printed (0—3) piezoelectric nanocomposites is strongly dependent on parameters such as surface linker chemistry, matrix mechanical properties, and nanoparticle size. With continued investigation on the strengthening and maximization of the stress-transfer efficiency at the inorganic-organic interface, it should be possible to fabricate composite materials with properties that exceed their ceramic monolith counterparts with less active material. Finally, optical printing with UV-curable polymers has been shown to be an ideal platform to systematically study and tune the piezoelectric properties of nanocomposites and offers one of the only routes to high precision, rapid, and 3D fabrication of piezoelectric polymers.

2.6 Methods

2.6.1 Barium Titanate (BT) Nanoparticle Synthesis and Surface Modification

80 nm BT particles were synthesized via a hydrothermal reaction similar to those found in literature [61]. Barium hydroxide [$Ba(OH)_2$; Sigma Aldrich, 98%], titanium butoxide ($Ti(O(CH)_3CH_3)_4$ [$Ti(BuOH)_4$; Sigma Aldrich, 97%], and diethanolamine ($NH(CH_2CH_2OH)_2$ [DEA; Fisher Scientific, laboratory grade] were used as the starting materials without further purification. $Ti(BuOH)_4$ (25 mmol) and 4M ammonia solution (3.5 mL) were added to ethanol (10 mL). This was combined with DI water (12.5 mL) containing $Ba(OH)_2$ (37.5 mmol). The solution was allowed to stir for five minutes after which DEA (2.5 mL) was added. This was allowed to stir for five minutes before being transferred to a PTFE lined stainless steel reactor which was heated to 200 °C for 16 hours. The reactor was then cooled to room temperature and the white precipitate was collected and washed 5 times with ethanol and 5 times with DI water. It was then dried at 80 °C for 24 hours yielding the final product of 80 nm BT nanoparticles. The dried nanoparticles were functionalized with 3-trimethoxysilylpropyl methacrylate (TMSPM) using similar grafting strategies to those carried out on silica surfaces [62]. TMSPM (1 mL) in ethanol (50 mL) was pH adjusted to 4 with an acetic acid solution (1 mL glacial acidic acid in 9 mL DI water). BT nanoparticles (0.6 g) were added to the TMSPM solution and sonicated for 24 hours. The particles then separated by centrifugation, cleaned with 5 washes of ethanol, and dried to yield the final product. TMSMM and MSPM modifications were performed similarly. The particles were confirmed to be $\sim$80 nm in size with scanning electron microscopy (Figure 2.4) and their tetragonal structure observed via X-ray diffraction (Figure 2.5). FTIR spectra (Figure 2.6) and thermogravimetric analysis (Figure 2.7) were also performed to confirm linker modification.

20 nm BT nanoparticles were synthesized via a hydrothermal reaction similar to those found in literature [63] and the resulting surface modification of oleic acid was exchanged for TMSPM [64]. Barium nitrate [$Ba(NO_3)_2$; Sigma Aldrich, 99.95%], sodium hydroxide [NaOH;

Alfar Aesar, 98%], butan-1-ol [$HOCH_2CH_2CH_2CH_3$; Alfar Aesar, 99.9%], titanium butoxide [$Ti(O(CH_2)_3CH3)_4$; Sigma Aldrich, 97%], and oleic acid [$CH_3(CH_2)_7CH{=}CH(CH_2)_7COOH$; Alfar Aesar, 99%] were used as the starting materials without further purification. $Ba(NO_3)_2$ (1 mmol) and sodium hydroxide (12.5 mL) were dissolved in DI water (5 mL). This was combined with a separate solution of butan-1-ol (5 mL) containing titanium butoxide (1 mmol) and oleic acid (2.5 mL). The solution was allowed to mix for ten minutes before being transferred to a PTFE lined stainless steel reactor and heated at 135 °C for 18 hours. The reactor was then allowed to cool to room temperature. The white precipitate was collected and washed with 5% acetic acid once followed by five washes of ethanol before being dispersed in toluene yielding 20 nm barium titanate nanoparticles capped with oleic acid. The particles were confirmed to be 20 nm in size with scanning transmission electron microscopy (see Figure 3.3b). In order to exchange the oleic acid ligand for TMSPM, toluene (50 mL) containing BT particles (100 mg) was mixed with triethylamine (2.5 mL), DI water (0.05 mL), and TMSPM (0.5 mL). Heptane (50 mL) was added and the solution was sonicated at 50 °C for 5 hours. The particles were then isolated by centrifugation, washed with ethanol, and dried under vacuum to yield the final product.

2.6.2 Optical Printing and Film Preparation

Irgacure 651 was added as the photoinitiator to PEGDA (258 Da, 575 Da, or 750 Da) at a concentration of 1 weight %. The TMSPM (or other linkers) modified BT nanoparticles were added to the PEGDA solutions and sonicated for 24 hours. The solution was injected between two conductive indium doped tin oxide (ITO) coated polyethylene terephthalate substrates (Thor Labs) which were spin coated with a layer of polymethyl methacrylate (1 micron) to prevent shorting. A layer of cured PDMS (125 μm) was used as a spacer for the top and bottom electrodes. Electrical wires were connected to the electrodes using silver epoxy, and the film was cured under a 365 nm UV lamp for 15 minutes. The films were polarized for 24 h at 120°C with a constant field of 10.2 MV/m that was maintained until the sample reached room temperature. The piezoelectric properties of the polymers were characterized using a home-built charge amplifier and a commercially available force

sensor (Tekscan, A201-1). To generate printed features, the sonicated PEGDA solution containing the BT nanoparticles was exposed to 365 nm UV light through a digital photomask as previously described [59]. The printed microstructures could then be transferred and sandwiched between similar electrodes as those used for the thin films.

2.7 Acknowledgments

Chapter 2, in full, is a reprint of the material as it appears in ACS Applied Materials & Interfaces 2016. James L. Middlebrook & Kanguk Kim, Jeffrey E. Chen, Wei Zhu, Shaochen Chen, and Donald J. Sirbuly. The dissertation author was the primary investigator and author of this paper.

2.8 Figures

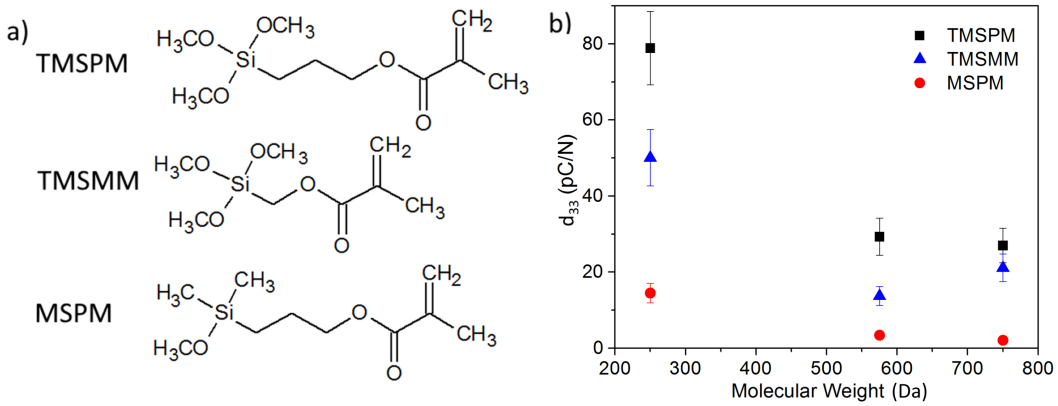

Figure 2.1: *Linker Molecule Structures and Impact on Device Piezoresponse*
a) Structures of methacrylate silane molecules used to functionalize the surface of the BT nanoparticles including 3-(trimethoxysilyl)propyl methacrylate (TMSPM), 3-(trimethoxysilyl)methyl methacrylate (TMSMM), and 3-(methoxydimethylsilyl)propyl methacrylate (MSPM). b) Piezoelectric coefficients (d_{33}) for unstructured PEGDA thin films (125 μm thick) with a 10% mass loading of 80 nm BT nanoparticles. The BT was surface functionalized with TMSPM (square), MSPM (circle), or TMSMM (triangle). The PEGDA molecular weights used were 258 Da, 575 Da, and 750 Da.

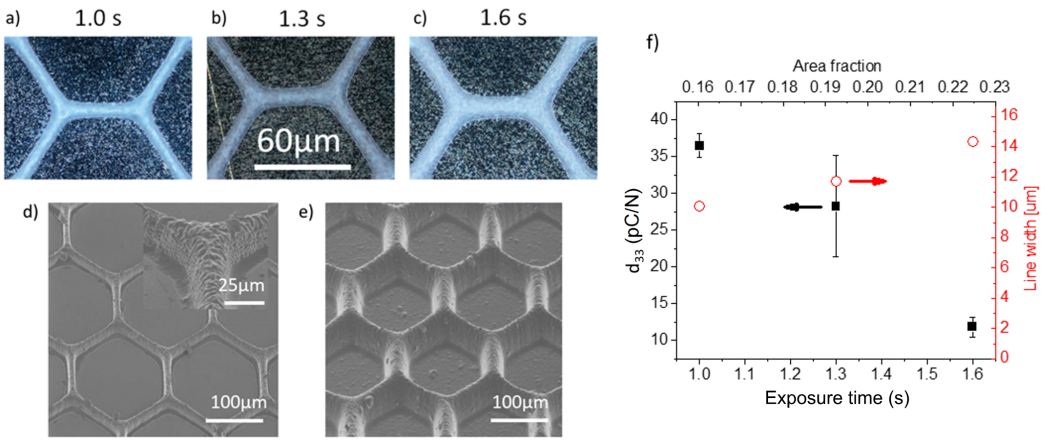

Figure 2.2: *Optimal Images and Piezoresponse of Printed Honeycomb Arrays*
Optical images of honeycomb arrays printed with UV exposure times of a) 1.0 second, b) 1.3 seconds, and c) 1.6 seconds. Scanning electron micrographs of the patterned structures produced with UV exposure times of d) 1.0 second and e) 1.6 seconds. f) Measured d_{33} coefficients and linewidths of the honeycomb arrays as a function of exposure time/area fraction.

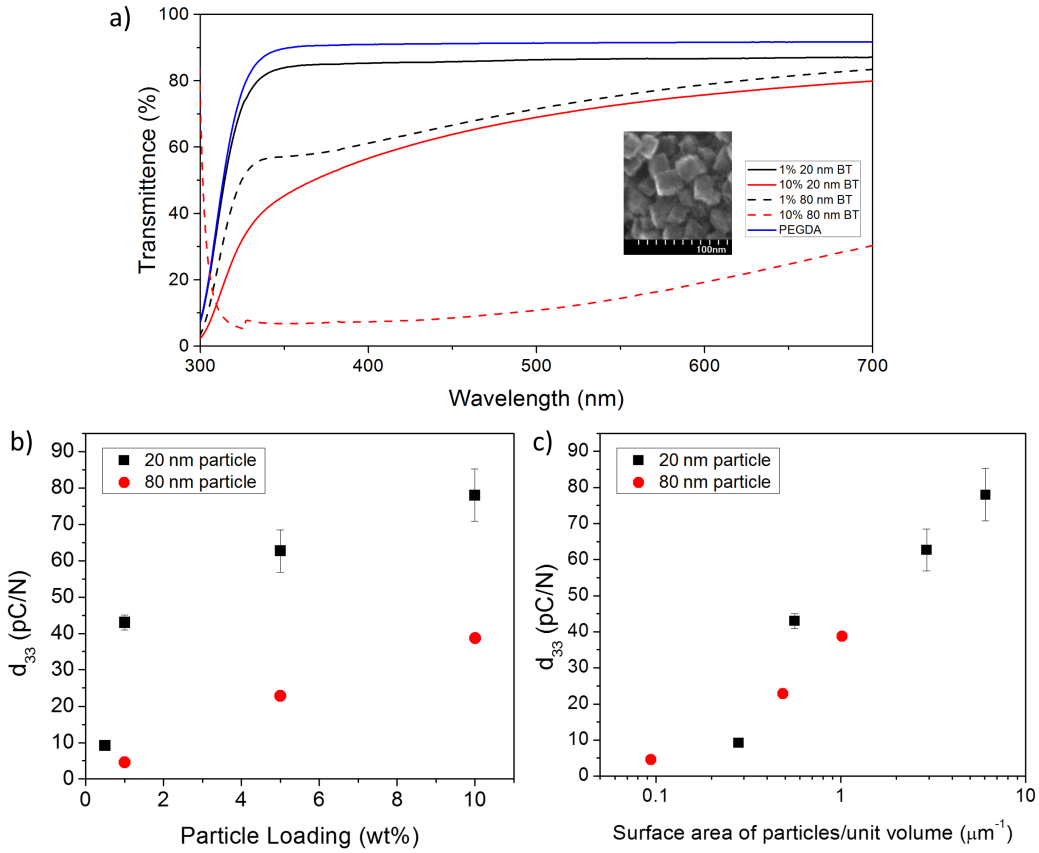

Figure 2.3: *Optical Extinction Spectra and Piezoresponse for Composites 20 nm or 80 nm Barium Titanate Nanoparticles*

a) Optical extinction spectra for 10 μm thick PEGDA composite films with 1% or 10% particle loading by weight of 20 nm or 80 nm BT nanoparticles with inset of scanning transmission electron microscope image of as-made 20 nm BT nanoparticles. b) Piezoelectric coefficients (d_{33}) as a function of a) particle loading percentage for 20 nm barium titanate nanoparticles (square) and 80 nm barium titanate nanoparticles (circle) in 25 micron PEGDA film devices and c) as a logarithmic function of particle surface area per unit volume.

2.9 Supplemental Figures

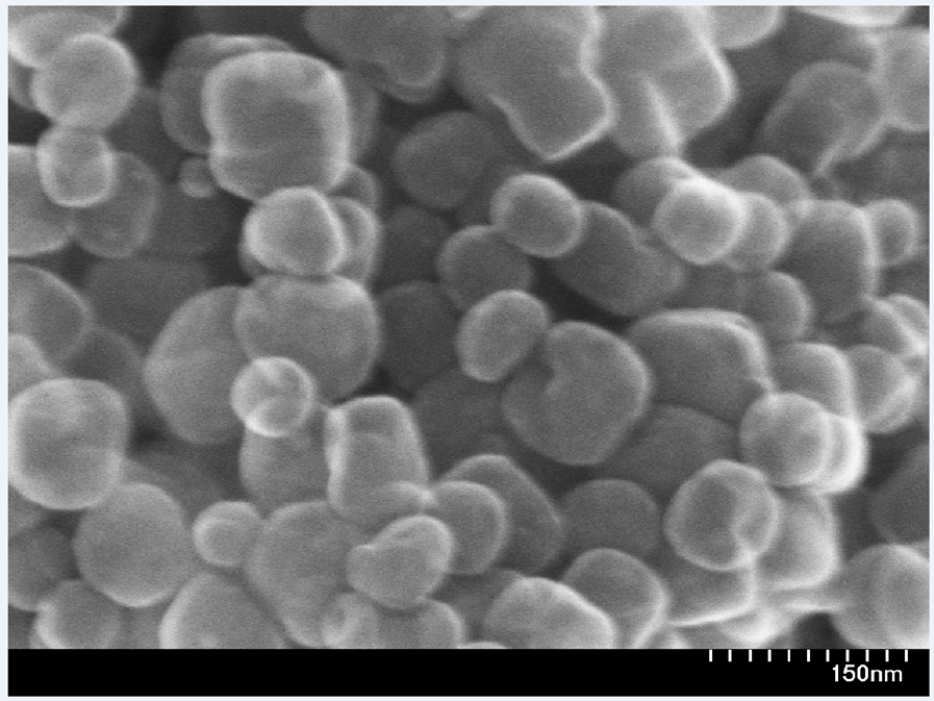

Figure 2.4: *Scanning transmission electron (STEM) image of as-made 80 nm BT particles*

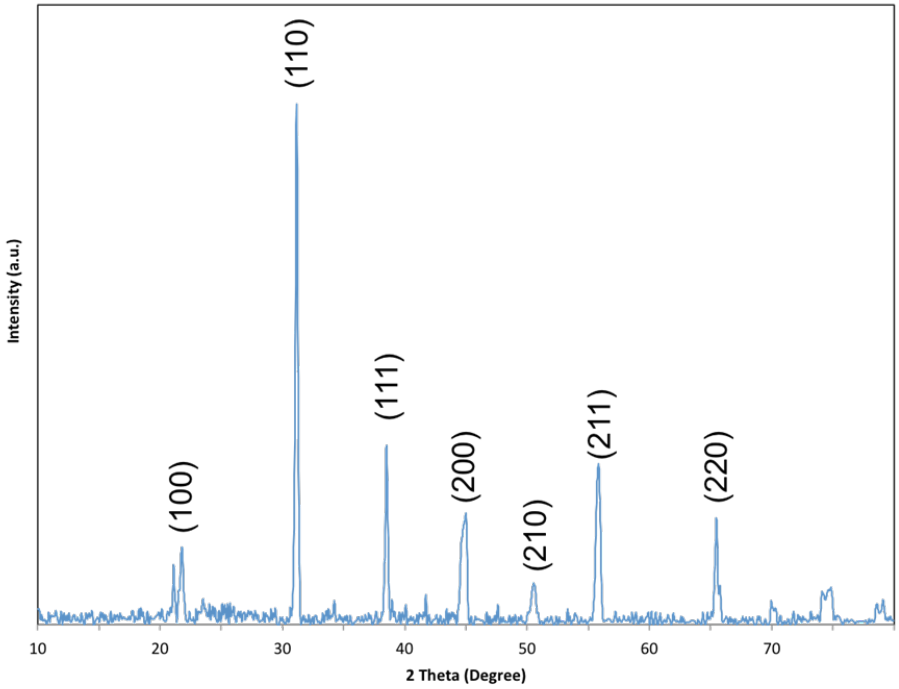

Figure 2.5: *X-ray diffraction spectrum of synthesized 80 nm BTO particles*

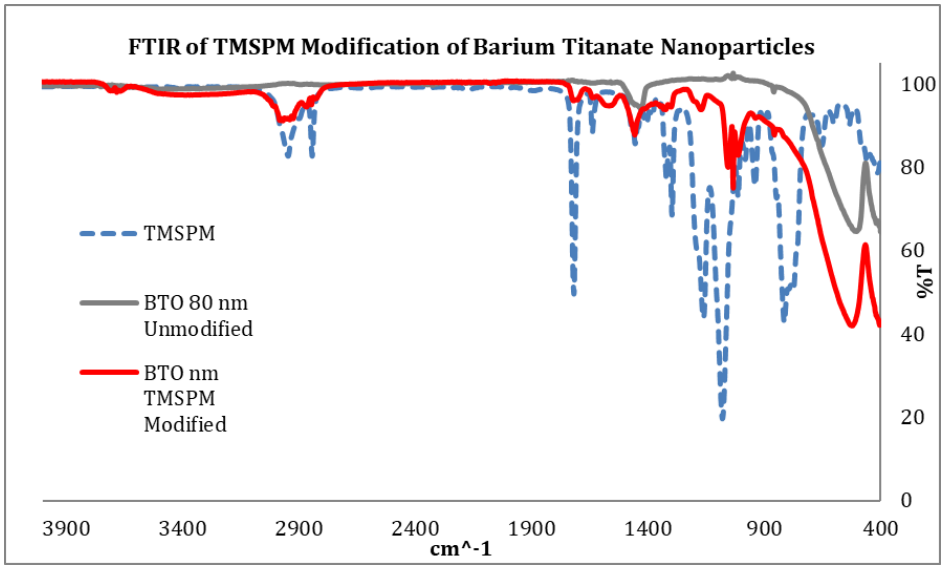

Figure 2.6: *Fourier transform infrared spectra of Barium Titanate Particles and Linker Molecules*
Fourier transform infrared (FTIR) spectra of BT particles, TMSPM, and BT particles functionalized with TMSPM which shows the successful modification of the particles.

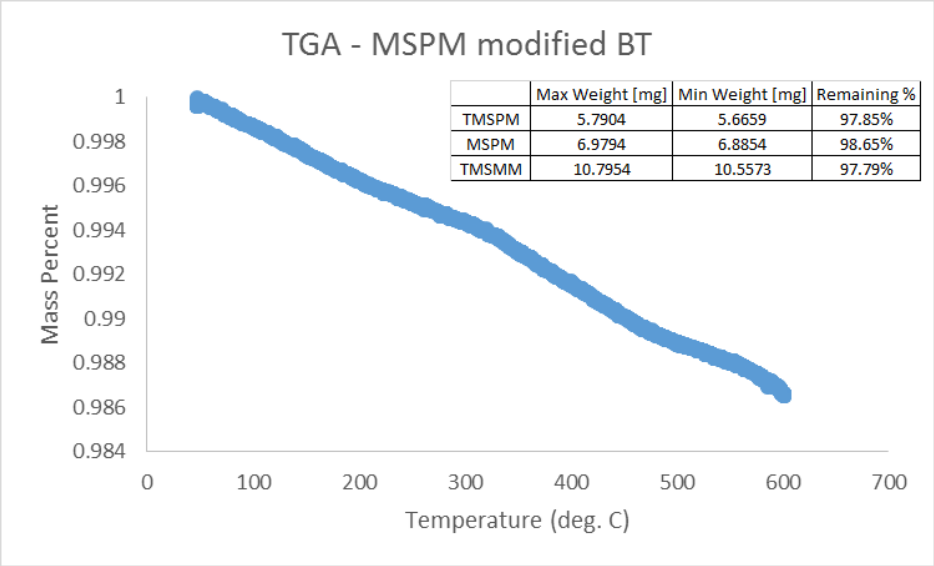

	Max Weight [mg]	Min Weight [mg]	Remaining %
TMSPM	5.7904	5.6659	97.85%
MSPM	6.9794	6.8854	98.65%
TMSMM	10.7954	10.5573	97.79%

Figure 2.7: *Thermalgravimetric Analysis of Linker-modified BT Nanoparticles*
Representative hermogravimetric analysis (TGA, Perkin Elmer Pyris) scan of MSPM-modified BT nanoparticles. Inset: Summary of TGA scans for TMSPM, MSPM, and TMSMM modified BT particles from room temperature to 600 °C.
Samples were run under the following parameters: Nitrogen carrier gas, 20.0 mL/min Hold for 1.0 min at 50.00°C Heat from 50.00°C to 600.00°C at 10.00°C/min
In order to ensure similar surface coverage of the modified nanoparticles, the surface groups were burned away through thermal degradation. The starting and final weights can be compared to determine the percentage of sample mass that is due to surface organics versus the ceramic which does not degrade in the temperature range. The mass percentage was found to be very similar for the differently modified particles leading us to believe there is similar surface coverage on the BT nanoparticles.

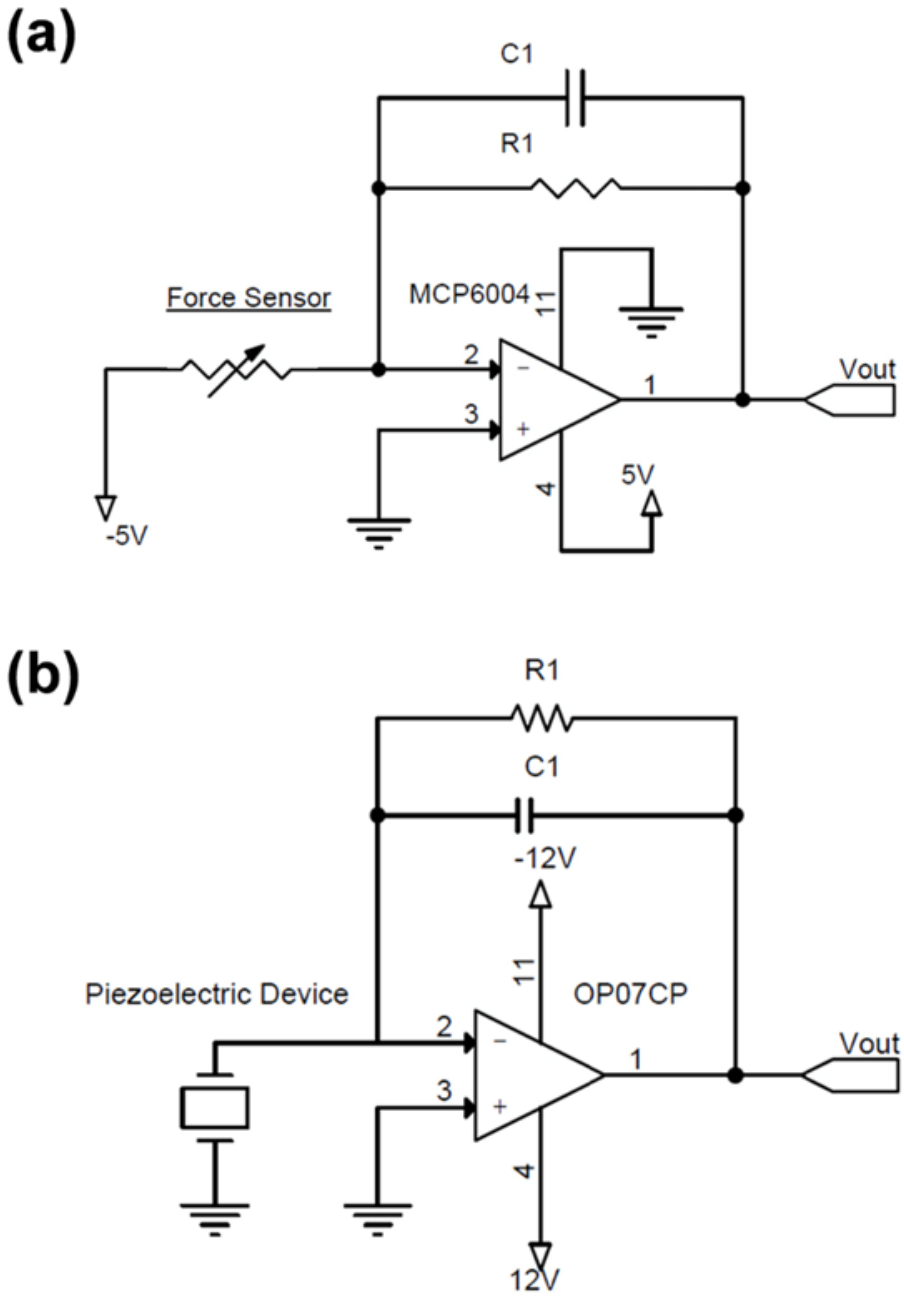

Figure 2.8: *Schematics of Tekscan FlexiForce and Charge Amplifier Circuits*
(a) Schematic of the FlexiForce® sensor (Tekscan) circuit that is placed underneath the printed piezoelectric to record the absolute force being applied to the samples simultaneously with the piezoelectric output. The output voltage of the sensor is tunable by changing the supply voltage and the feedback resistor, R1. The capacitor, C1, was used as the bypass capacitor. The force sensor was calibrated by placing known loads and measuring the voltage output. Under the most sensitive configuration (-5 V supply; R1 = 10 kW) the sensor shows a linear relationship with respect to load above 2 N. (b) Schematic of the charge amplifier used in the home-build piezo-testing apparatus. Charge generated from the sample is transferred to the reference capacitor, C1, which produces an output voltage, V_{out}, that is equal to the voltage across C1 (i.e., $V_c = -Q_{generated}/C1$). For the experiments, a 100 pF reference capacitor and a 20 MΩ feedback resistor, R1, were used allowing the effective piezoelectic coefficient, d_{33}, to be calculated from $d_{33} = V_{out} \times 100\ pF/F_{applied}$.

Chapter 3

Design and Application of Optically Printed (0–3) Piezoelectric Nanocomposites for Measuring Human–Space Suit Interactions

3.1 Introduction

The optical printed piezoelectric composite materials with tunable matrix and piezoresponse properties that were described in Chapter 2 can be applied effectively in the wearable sensor space. Due to their ability to optically printed to a given geometry and have mechanic properties such as stiffness and flexibility that can shifted to meet a given application, they were identified as an ideal candidate for a proof-of-concept Phase 1 Small Business Innovation Research grant awarded by the National Aeronautics and Space Administration (NASA) for a "Sensor to Measure Space Suit Interactions with the Human Body" (Contract NNX17CJ14P, Topic Code H4.03).

The goals for the project were to identify the ideal combination of materials described in Chapter 2's tunable matrix and nanoparticle system for the application, improve upon the electrode system used for charge collection, and ultimately show an arrayed, flexible sensing platform capable of accurately measuring static and dynamic forces and impacts. The final profile of the array should

allow for the sensors to be integrated into a lining of a space suit at a sensor thickness of less than one millimeter. Additionally, a low power requirement of < 50 mW is needed to power the device.

3.2 Optically Printed Composite

The piezoelectric nanoparticle chemical functionalization that was identified as most suitable for the application was the 3-(trimethoxysilyl)propyl methacrylate (TMSPM) as that was shown to improve composite piezoresponse more than unfunctionalized particles or particles functionalized with other acrylate linker molecules[65].

The optical printing method is capable of crosslinking polyethylene glycol diacrylate (PEGDA) polymers with monomers of different molecular weights. Composites made with PEGDA of molecular weights of 250 Da, 575 Da, and 700 Da were examined for this work. As shown in Chapter 2, crosslinking of shorter monomer causes the cured polymer to be of a higher modulus (stiffness) than longer monomers, a trend opposite for non-crosslinked polymers such as polyethylene glycol [60]. This can be illustrated in Figure 3.1 that illustrates how crosslinking of shorter chains may cause for a stiffer, more linked, final polymer matrix. While the shorter 250 Da PEGDA monomer had been shown to have the highest piezoresponse of these composite variations as shown in Figure 2.7, the high modulus made it too fragile and inflexible to be robustly integrated into sensors for this application.

For barium titanate additives for the composite, different candidate loading percentages of 20, 50 nm, and 200 nm barium titanate nanoparticles were evaluated for the application. As maximizing particle loading percentage and nanoparticle surface area had been shown to improve device piezoelectric charge coefficient, 20 nm particles would be ideal. As the reaction yields of the process described in Chapter 2.6.1 would be too low, the 20 nm particle was determined to be less feasible than more accessible 50 nm commercially produced particles.

Using the process as described in detail in Chapter 2.6.2, 1 cm x 1 cm x 200 micron PEGDA-BTO slabs were optically printed and polarized. A schematic of this process can be seen in Figure

3.1.

3.3 Device Design and Fabrication

In order to harvest the charge output from the sensing material, electroding is a critical step. While many bulk electroceramic materials have screen printed or sputtered metal directly placed onto the material, composite device robustness can be benefited by having an extra layer that is able to protect the composite and also provide an avenue for more easily attaching electrical leads to the stack. Commercially prepared films of polyethylene terephthalate (PET) with a conductive layer of indium tin oxide (ITO) were evaluated (Thor Labs, ITO-PET, sheet resistance of 350-500 ohm/sq) along with gold-titanium sputtered (300 nm, 20 nm) on polyimide film electrodes (Au/Ti @ polyimide). The ability for the sensors to be arrayed as well as complete device thickness were considerations for the final application as well as the electrodes' electrical properties. The ITO-PET film was measured by micrometer to be $\sim$200 microns in thickness while the sputtered polyimide was measured to be $\sim$130 microns which lead to total device thicknesses of at least 600 microns and 460 microns, respectively. As the ITO-PET sheets were conductive across their entire surface, sensing regions would need to be electrically separated. This could potentially be done by scoring the material to attempt to sever the electrical connection, though proved not completely effective. The alternative would be to cut and array ITO-PET electrodes onto a secondary backing, which would further increase device thickness. These problems were not felt for sputtered Au/Ti @ polyimide as masks can be used during the sputtering process to separate sensing regions. Finally, the sheet resistance of the ITO-PET material causes there to be a much higher resistance felt at the electrode than a sputtered metal material. For these reasons, Au/Ti @ polyimide electroding was chosen for the the composite application for measuring human–space suit interactions.

Options for device adhesion layers were also evaluated. Electrically, using a thin layer of the same optically printed material used to make the slab of material would be ideal as the matching properties would be unmatched. Unfortunately, the PEGDA-electrode bond was not strong enough

to support flexure without delamination of the sensor stack from the electrodes. Instead, a thin layer of room-temperature-vulcanizing silicone (Momentive, RTV108) was combined with barium titanate nanoparticles (10% wt BTO/wt %), mixed, then applied to the top and bottom electrodes, leveled to a thickness of 60 microns with a razorblade tape casting method, and then a sample of the polarized optically printed PEGDA-barium titanate material sandwiched between. This allowed for a continuation of the piezoelectric component on the composite from electrode to electrode.

A 2x2 array of sensing devices was chosen as a proof of concept for the arrayability of the devices and for ease of electrical measurements. A schematic of the 2x2 array assembly process, a device assembly sideview schematic, and multiple optical images of the final device array along with thickness measurements can be seen in Figure 3.2.

3.4 Device Characterizations

The 2x2 array was assessed for its ability to give a proportional response to impact forces (i.e. dynamic range), the presence of sensor response crosstalk, and its ability to measure static forces. For measuring the device's dynamic range, a droptest was performed using a droptower and a weighted droprod to apply an impact force to the sample. The input peak force and force during the impact event was monitored by a piezoresistive sensor and circuit (Tekscan FlexiForce A201-1 Sensor, FlexiForce Quickstart Board) monitored by a digital oscilloscope (Rigol DS1054Z). The voltage output from the device was captured without modification by a digital oscilloscope (Rigol DS1054Z). A schematic of the droptest setup used can be seen in Figure 3.3. By collecting data from across multiple impacts and scatter plotting them, we can begin to see the dynamic range of the device of how its voltage output responds to various forces. From the peak-to-peak voltage output and peak force experienced in the impact event, the dynamic range can be shown as seen in Figure 3.4. The sample's output can be represented well for this force range with a logarithmic relation ($R^2 = 0.969$) showing that the device responds nearly linearly but at a larger sensitivity in the 0-30 N range, likely due to other charge transfer events such as triboelectricity which can be

minimized but never eliminated. This curve allows for calibration of the device to be an accurate measure of impact forces while acting as a self-powered sensor. The array was also assessed for cross-talk across sensing regions and under peak

While piezoelectric devices are effective at measuring dynamic forces, charge leakage causes low frequency forces and static forces to be challenging to accurately measure. For this device, an alternative sensing mode as a capacitive sensor was used to measure static forces. By monitoring the capacitance of the device with an external circuit (Texas Instruments FDC2114) as known static forces are applied, a calibration curve can be formed, as shown in Figure 3.5. As shown, a capacitance increase rise of up to 20% is observed for the sample while under static loads of up to 30 N. While this measurement requires an externally powered method to measure the capacitance, it does allow for the device to be capable of non-dynamic forces. As the device acts as a parallel plate capacitor with a capacitance, C, described by Equation 3.1 where ε_0 is the permittivity of free space, k is the relative permittivity of the optically printed slab and adhesion layers, A is the electrode area, and d is the inter-electrode distance. A static force applied to the device will apply a stress, T, which causes a strain, S, and reduction in the inter-electrode distance d, d, according to its elastic modulus, s, as shown by Equation 3.2.

$$C = k * \varepsilon_0 * A/d \tag{3.1}$$

$$S = s * T \tag{3.2}$$

As the forces experienced by the sample likely go beyond its elastic limit, that would explain the logarithmic fit of the curve, though additional measurements of the sample mechanical properties would be needed to confirm. This ability for the device to have a characterized response to non-dynamic forces allows for the device to be an accurate measure of static forces.

3.5 Conclusions

In this work, the tuned optically printed piezoelectric polymer–barium titanate composite was able to be developed into an arrayed force sensor. Leveraging the ability to print extremely thin materials as well as being able to tune the mechanical, optical, and electrical properties of matrix and composite allowed for this platform to be able to be integrated into a space suit lining in order to measure and better understand human–space suit interactions.

3.6 Acknowledgments

This work was conducted under NASA SBIR Contract NNX17CJ14P and the author would like the acknowledge our SBIR co-awardees, Mr. James Phelps, Mr. Carl Edwards, committee member Prof. Shaochen Chen, and his student Natalie Lawrence for their contributions and insight into this project.

3.7 Figures

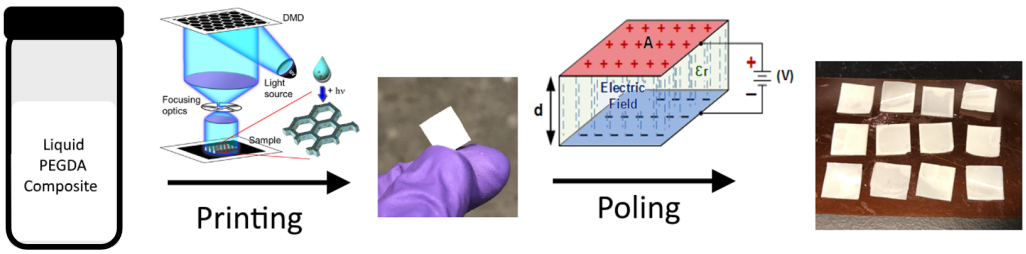

Figure 3.1: *Schematic of Optical Printing Method for Space Suit Sensor Slabs*
Schematic showing the starting material of a PEGDA, 10% wt/wt Barium Titanate (50 nm) composite before photocrosslinking, the crosslinking that occurs during the optical printing process[59], an as printed 1 cm x 1 cm slab before activation by poling, a diagram illustrating the poling process, and an optical image of a dozen optically printed slabs after polarization.

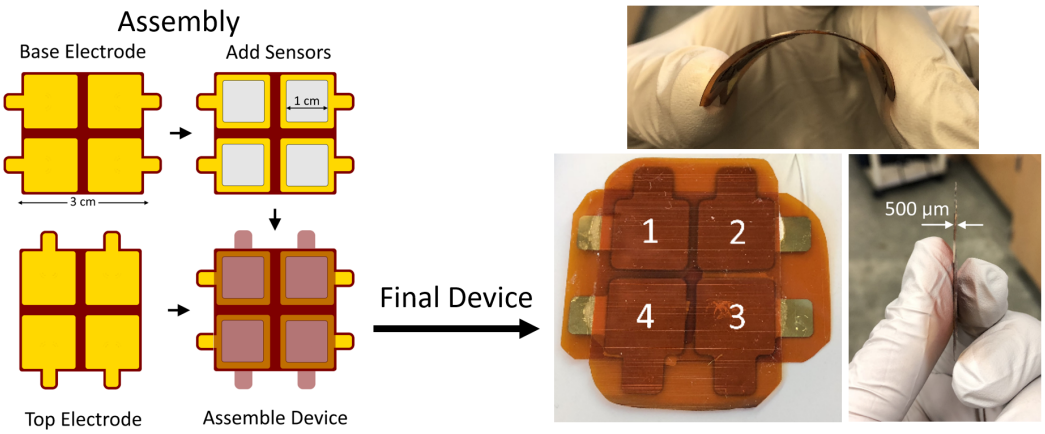

Figure 3.2: *Schematic of 2x2 Arrayed Sensor Assembly and Optical Images of the Sensor Array*
Schematic of assembly steps, silicone adhesion layer omitted. Optical images show curving of the device without failure in order to highlight its flexibility as well as the overall thinness of the sensor array at 500 microns.

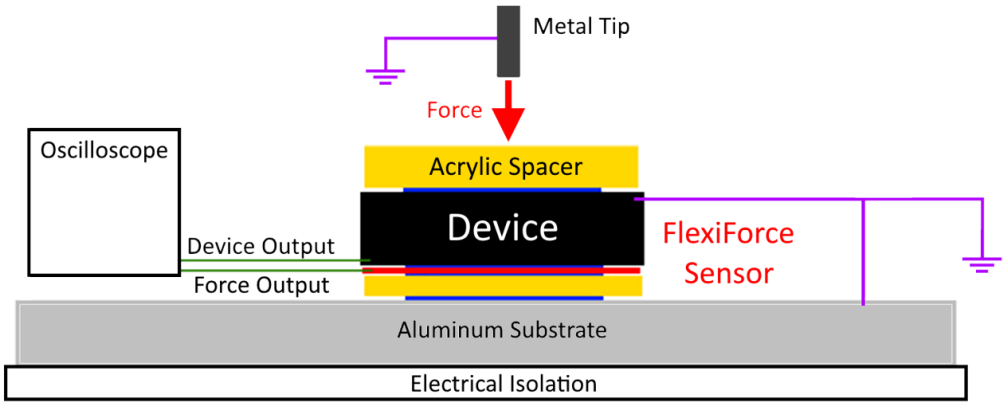

Figure 3.3: *Droptest Measurement Schematic*
A schematic of the droptest setup used to measure impact forces and device output in response to impact forces. FlexiForce Sensor was made up of a Tekscan FlexiForce A201-1 Sensor and a FlexiForce Quickstart Board with both the force measurement as well as the device voltage output monitored by a Rigol DS1054Z digital oscilloscope.

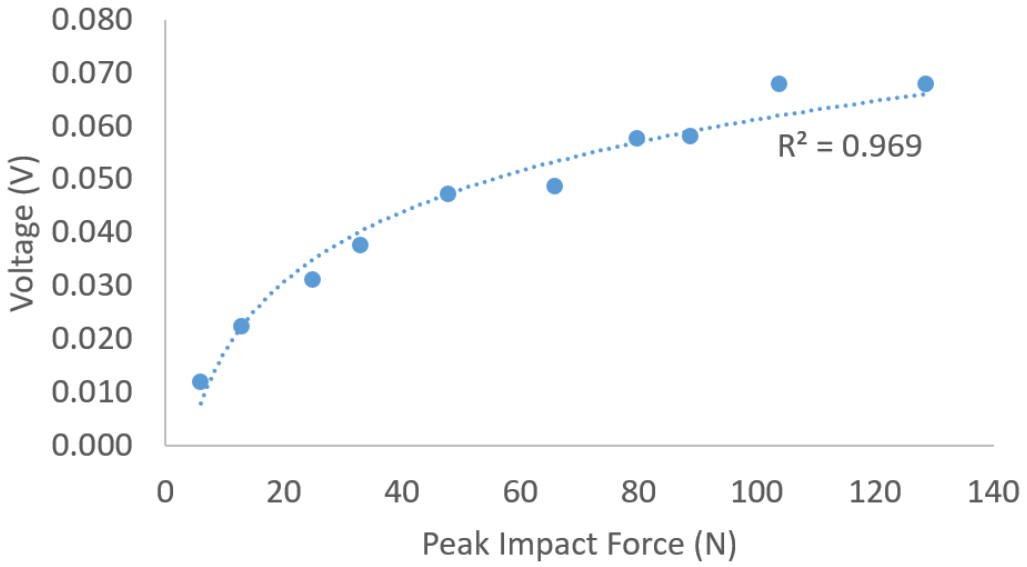

Figure 3.4: *Optically Printed Piezoelectric Nanocomposite Dynamic Range Response to Dynamic Forces*

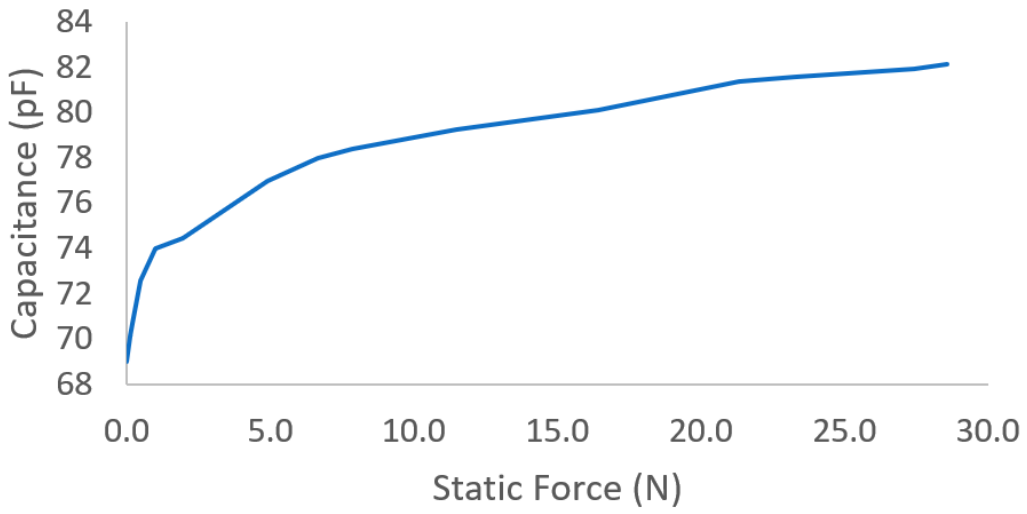

Figure 3.5: *Optically Printed Piezoelectric Nanocomposite Capacitance Change Response to Static Forces*

Chapter 4

Polymer-Ceramic Compressible Foam Piezoelectric Composites

4.1 Introduction

Polymer-ceramic compressible foam materials are large step forward in the ability for applying piezoelectric composite to the wearable space. An obstacle in expanding the applications of bulk electroceramic piezoelectrics has been their inflexibility and challenging processibility of conventional composites such as dice-and-fill (1-3) composites. Through the use of a sugar templating method, creating soft, compressible polydimethylsiloxane-barium titanate composites allowed for low modulus materials with a piezoelectric output that is above most pure polymer piezoelectric materials [66, 67]. While the original platform allowed for the creation of an intelligent, foam based piezoelectric sensor, the materials could be further optimized in order to improve device performance, processability, and robustness. By using the knowledge gained through tuning optically printed materials and expanding our polymeric material choices beyond polydimethylsiloxane, improvements to this sensor platform can be made in a few major ways: adjusting the polymer matrix to tune mechanical properties, create covalent linkages between the nanoceramic and the matrix to improve performance, and revisiting the device construction to improve robustness.

Several types of foam and highly porous piezoelectric materials and composites have been the focus of research in recent years, highlighting the interest in the space. Unique compositions including polypropylene ferroelectrets, molecularly doped polyurethane, and pure ceramic foams [24, 23, 68].

As a sensing platform, these materials and devices show promise due to their ability to sense forces and impacts while being flexible, compressible, and a tunable Young's modulus of elasticity as low as 30 kPa. The wearable technology market is projected to grow over the next few years at a compound annual growth rate of 15.9% [69], more the doubling in size every 5 years. With this growth, there is continued interest to expand what can be sensed and acted upon so that people can try to live healthier, fitter, or more informed lives. One way that wearable technologies can accomplish that is being able to more seamlessly integrate themselves into the products that we interact with on the daily basis. Polyurethane based polymer-ceramic compressible foam piezoelectric sensors have a tunable modulus to that is able to match the properties of products such as footwear, biomedical monitoring systems, and seating.

4.2 Polymer Considerations

The original platform was designed with a sugar templating method of polydimethylsiloxane (PDMS) in order to create a PDMS-barium titanate foam (U.S. Patent 20160181506A1 [67]). By crushing sugar and combining with PDMS into a paste or dough, the material can be cured into various shapes and then the sugar boiled out. While this was effective in creating the porous final material, high and low sugar loadings could cause issues with the final material. High sugar loadings ($> 70\%$ sugar by volume) could cause the material to be overly porous and too delicate to be effectively fabricated into a final device. Lower sugar loadings ($< 50\%$) could lead to regions where sugar could not be effectively accessed and removed during the boiling step – similar to a closed cell foam. Combined with the labor intensive nature of the multiple soaking steps that each material puck needed and the high cost of PDMS compared to other polymers, improving the polymer matrix

could serve many purposes. Two alternative polymer systems that were identified to host the next generation of this compressive foam polymer-ceramic sensing platform were ethylene-vinyl acetate (EVA) and polyurethane (PU) due to their capabilities to self-foam, reduced cost, and ubiquitous use throughout wearable sectors of interest including clothing, footwear, and furniture.

Ethylene-vinyl acetate (EVA) composite foam samples were created via a third party (Dexcorp) and assessed for their ability to be fabricated into devices. The composition of the foam was tuned to be 10% by weight barium titanate nanoparticles (200 nm, US Research Nanomaterials, Inc), 1% by weight carbon nanotubes (multi-walled, US Research Nanomaterials, Inc), with the remainder being EVA. One step in the fabrication process is polarizing (poling) the material at 110 $^{\circ}$ C, and 3.3 kV/ mm electric field in order to align the crystal domains of the barium titanate ceramic component. At poling temperatures, the EVA foam undergoes a significant shrinking, stiffening, and densification converting it from a compressible, flexible foam to a material more akin to hockey puck and limiting its further application as a host polymer for the platform.

Polyurethane (PU) composite foam samples were created with a composition of 10% by weight barium titanate nanoparticles (200 nm, US Research Nanomaterials, Inc), 1% by weight carbon nanotubes (multi-walled, US Research Nanomaterials, Inc), with the remainder being polyurethane (Smooth-on FlexFoam-iT! 17 lb/ft^3 two part polyurethane mix). These polyurethane based composites were compatible with the poling process and could be successfully fabricated into sensing devices. Polyurethanes can be formed in a reaction between diisocyanate and a polyalcohol typically catalyzed by an amine to form a urethane linkage. Similar to Chapter 2's method of covalently linking the PEGDA to barium titanate nanoparticles during the photopolymerization of the polymer, the urethane polymerization reaction is able to bond the barium titanate nanoparticles into the matrix. Through an oxidation reaction, the natively hydroxalized surfaces of the as-received barium titanate become fully hydroxalized. This surface is then able to participate in the reaction behaving chemically similar to the polyalcohol. This will serve enhance the composite device's output compared to the PDMS or EVA based system where particles are encapsulated but not linked into the matrix as shown by surface/interface effect modeling for a piezoelectric nanoparticle in a

polymer matrix under compression waves [70]. Some additional evidence of this can be seen in scanning electron microscopy (SEM) images in Figure 4.1 that suggests a distortion of the local matrix surrounding the barium titanate nanoparticles in the PU composite while no such distortion was observed for EVA composites. As this could just be a charging effect of the SEM, further studies would be needed to verify the covalent linking inside the PU based composite.

Polyurethane's components, diisocyanate and polyalcohols, can each be tailored in order to adjust the final polymer's mechanical properties [71]. As an example, increasing the length of the softer polyol component of the polyurethane can act to stiffen the final polymer [72]. Additives known as blowing agents can also be incorporated which can cause the polymer to create void spaces. In this work, a water additive component was a part of the commercial polyurethane mix which is used to react with isocyanate in the polymer components to outgas carbon dioxide and create the porous polymer. The porous nature of these materials allows for stress to concentrate at junctions in the material which can cause an enhancement in piezoelectric response as shown experimentally [66] and via a finite element analysis [73].

4.3 Device Fabrication

With a polymer matrix selected, the composite material can be created. Based on the desired final weight percentages, additive components like barium titanate nanoparticles or carbon nanotubes can be added to one or more of the polymer precursors. High energy mixing methods such as planetary centrifugal mixing and sonicating can be helpful in dispersing the materials throughout the prepolymers. Due to the high density of ceramic nanoparticles, it is common for the material to begin settling out within hours of mixing. Molds can be assembled at this stage with the desired dimensions if the material is to be cast. Laser cut acrylic vented molds worked well for PDMS and PU composite casting of pucks. Once cast, the material should then be poled at an elevated temperature under an electric field. Due to reductions in Curie temperature with barium titanate particle size, a lower poling temperature (105-110 deg C) than those used for the

polarization of bulk polycrystalline barium titanate may need to be used [20]. A poling field is excess of the coercive field of the ferroelectric component of the composite is generally ideal for fully polarizing the composite, though fields below the dielectric breakdown of air may be needed to avoid void charging or damaging the material. The coercive field for barium titanate nanocrystal thinfilms has been reported 1.2 kV/cm [74] as high as 7.2 kV/cm for a 50% porous barium titanate ceramic [12], well below the dielectric breakdown of air at 38 kV/cm [75]. Typical poling voltages used in the exploration of this work were $\sim$35 kV/cm.

In order to harvest the charge output from the sensing material, electroding is a critical step. While many bulk electroceramic materials have screen printed or sputtered metal directly placed onto the material, composite device robustness can be benefited by having an extra layer that is able to protect the composite and also provide an avenue for more easily attaching electrical leads to the stack. Commercially prepared films of polyethylene terephthalate (PET) with a conductive layer of indium tin oxide (ITO) were evaluated (Thor Labs, ITO-PET, sheet resistance of 350-500 ohm/sq) along with gold-titanium sputtered (300 nm, 20 nm) on polyimide film electrodes (Au/Ti @ polyimide). For robustness and scalability, ITO-PET electrodes were generally used as they were able to be bound to the material with a room temperature vulcanizing silicone that was razerbladed onto each laser cut electrode to a thickness of $\sim$60 microns before adhering. This prevented the most common method of device failure, delamination.

4.4 Device Characterizations and Limitations

As the main application for these devices is monitoring the voltage output in response to impact forces, a droptest tower as previously described in Chapter 3 was used.

Comparing the electrical piezoresponse of these polyurethane based foams to their PDMS counterparts, we can see a large improvement in the electrical performance from 2.5 V, peak-to-peak, at 20 N of peak force[66] to 10.8 V, peak-to-peak, at 21.4 N of peak force, an improvement in the voltage output of 330%. The polyurethane device sample's voltage response as a function of

peak input force can be seen in Figure 4.2.

While the devices described in this work are capable of generating electrical potentials at voltages as high as 15 V, the current generated is on the order of 10 nA, causing the net power generated to be very small in comparison to the mechanical work applied to the devices. This can be described by the electromechanical coupling factor, k, as seen in Equation 4.1:

$$k^2 = \frac{\text{mechanical energy converted to electrical energy}}{\text{input mechanical energy}} \tag{4.1}$$

These materials have been observed to ouput approximately 150 pJ of electrical energy in response to a 5 mJ impact creating a k value of approximately 1.7E-4, several orders below PZT's electromechanical coupling factor of 0.67, a far more efficient interconverter of electrical and mechanical energy [76]. This could be do to the viscoelastic nature of these polymer-ceramic piezoelectric composite materials where energies can be more easily dissipated through mechanisms that do not result in high electrical energy output via the direct effect [77]. This may also explain why the converse effect is challenging to observe for these materials. As an experiment to test this, a high energy, broadband chirp signal voltage was sent to a piezoelectric composite across the high kHz through MHz range. No observed actuation of the material was had, likely due to the low volumetric loading of piezoelectric material causing it to be unable to activate the bulk to resonate. For the same reasons that these materials are able to stress concentrate through the softer polymer matrix to enhance cause their high piezoelectric response relative to the piezoelectric loading percentage may be why the converse effect is hampered.

While all poled piezoelectric polycrystalline ceramics will slowly depolarize as their crystal domains reorient randomly, typically as a logarithmic function of time [7]. While longterm studies of these compressible foam based piezoelectric composites will need to be done to monitor their aging properties, it is the belief that the nanoparticle size and covalent linking of the electroceramic to the matrix will allow for a longer effectiveness compared to other materials such as molecularly doped foam materials with a piezoresponse halflife of 20.7 hours [23]. A short term study was performed on PDMS based foam composite materials that did not have this covalent linking. The

piezoresponse was monitored at a set force for 312 hours after polarization for a barium titanate nanoparticle (200 nm, 10% wt/wt %) sample, a carbon nanotube sample (1% wt/wt %), a silicon dioxide nanoparticle sample (200 nm, 10% wt/wt %), and a pure PDMS sample with no additives as shown in Figure 4.3. The barium titanate containing sample had a higher signal output at every measurement while the other controls stayed mostly together. The overall voltage response varied between trials for unknown reasons, but the data normalized to the PDMS control (Figure 4.3b) shows the aging of the polymer-barium titanate relative signal to 48.6% above the PDMS sample after 312 hours.

Hysteresis curves for a barium titanate nanoparticle (200 nm, 60% wt/wt%, 1 mm thickness) polyurethane foam composite material at 85 Hz and a PZT ceramic (APC 841 PZT, 1 mm thickness) device were evaluated via a Sawyer-Tower circuit as seen in Figure 4.4. Due to the large thickness and equipment limitations, only a low peak field strength of 30-40 V/mm was achieved. Even at these lower field stengths, the tilting of the hysteresis curve is observed compared to the bulk ceramic, as seen in other porous piezoelectric materials [12].

4.5 Conclusions

Compressible foam piezoelectric materials are capable of providing unique sensing solutions to the wearable space. From the initial work with polydimethylsiloxane, substantial improvements in performance, processability, and tunability have been shown by modifying the composition of the foam material and continuing to develop the integration of the material into sensing devices.

4.6 Figures

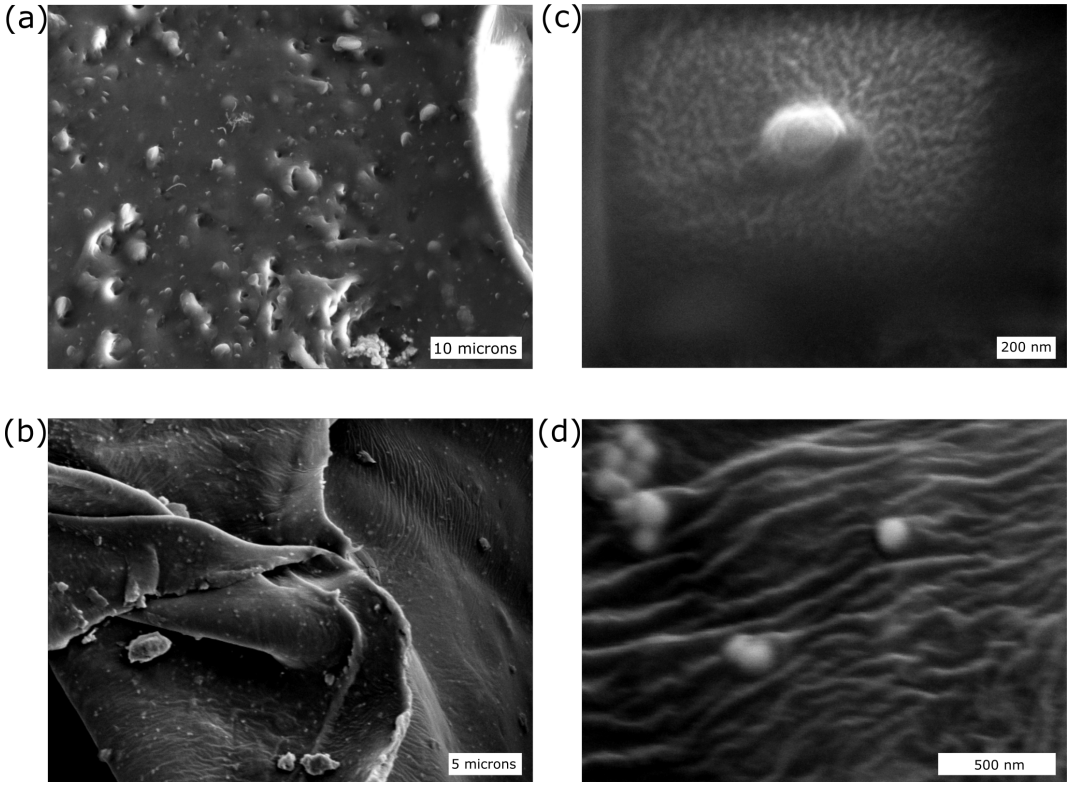

Figure 4.1: *Scanning electron micrographs of polyurethane and ethylene-vinyl acetate based foam barium titanate composites*
Scanning electron micrographs of (a,b) polyurethane and (c,d) ethylene-vinyl acetate (EVA) based foam barium titanate composites. In (a) individual carbon-nanotubes along with individually dispersed 200 nm barium titanate articles are visible. In (d), nanoparticles are seen aggregated on the surface of the EVA

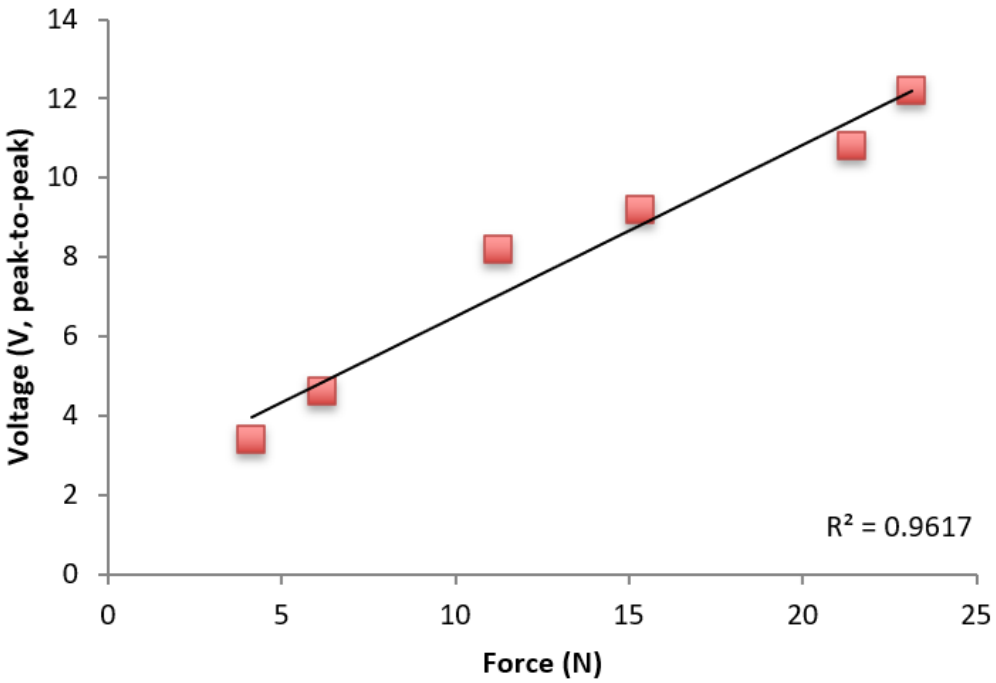

Figure 4.2: *Dynamic range of polyurethane-barium titanate foam piezoelectric composite devices*
Droptest piezoresponse of polyurethane-barium titanate foam piezoelectric composite devices as a function of peak impact force.

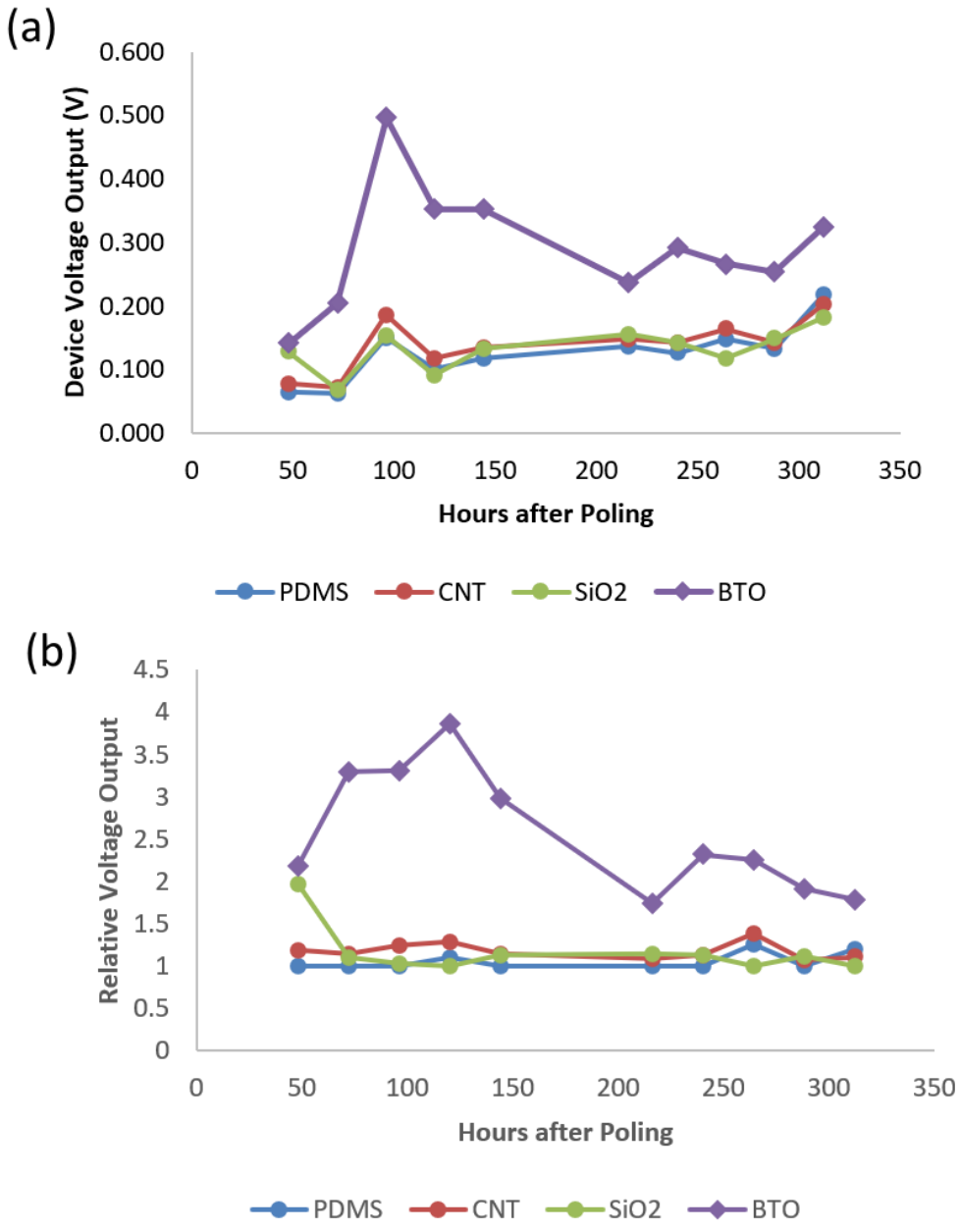

Figure 4.3: *Droptest piezoresponse aging for polydimethylsiloxane-based composite devices*
Droptest piezoresponses for pure polydimethylsiloxane (PDMS) compressible foam sample (Blue), compressible PDMS foam sample with a carbon nanotube additive (1% wt/wt %, Red), compressible PDMS foam sample with a silicon dioxide nanoparticle additive (200 nm, 10% wt/wt %, Green), and a compressible PDMS foam sample with a barium titanate nanoparticle additive (200 nm,10% wt/wt %, Purple) measured across 312 hours after poling.

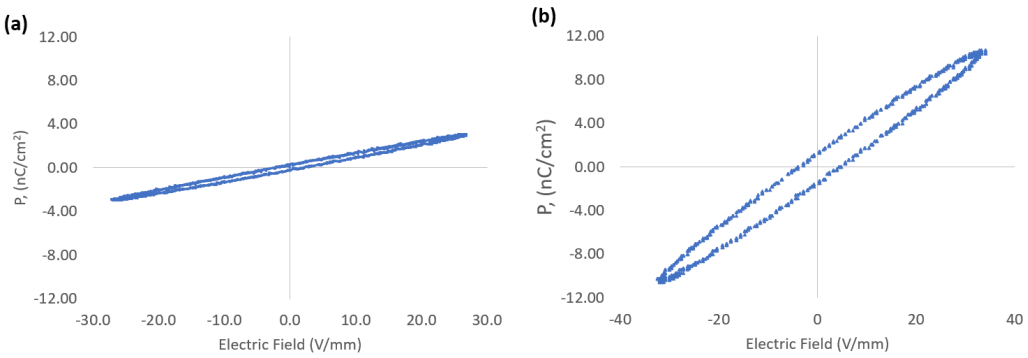

Figure 4.4: *Ferroelectric hysteresis curves for barium titanate-polymer foam composite device and PZT device* Ferroelectric hysteresis curves for (a) barium titanate nanoparticle (200 nm, 60% wt/wt%, 1 mm thickness) polyurethane foam composite material at 85 Hz and (b) PZT ceramic (APC 841 PZT, 1 mm thickness) at 54 Hz as measured by a Sawyer-Tower Circuit.

Chapter 5

Accessible Piezoelectric Testing Suite for Composite Sensors in Wearable Applications

5.1 Introduction

There is a growing interest for the use of piezoelectric composite materials to be used in the wearable space, but conventional equipment to attempt to characterize and develop these devices can be cost prohibitive. In this section, we explore a more cost-effective, purpose-built testing suite designed to allow for the characterization of these materials under a variety of conditions that better model our real world. Through the use of a voice coil linear actuator system as well as force, voltage, and charge measurements, we are able to more accessibly assess these materials' uses in the wearable space. A schematic of the bench-top testing system can be seen in Figure 5.1.

Considerations for position, force, charge, and voltage data collection and processing will be discussed as well as the methods and reasoning behind the chosen routes for data collection. While many programs are able to process the output files collected, MATLAB was used in the development of the testing suite and the associated MATLAB files may be provided upon request to

the author.

5.2 Linear Actuation and Strain Measurement

The most unique and helpful feature of this characterization setup if the use of a Voice Coil Linear Actuator manufactured by BEI Kimco (Model DK-LAS16-23-000A-P01-4E Developer Kit) which allows for a rapidly responding strain to be applied with a resolution of 10 μm. Compared to systems that would offer similar control for the strains (0-0.8 ε), frequencies (0-20 Hz), and forces (0-10 N) of interest for these materials, this linear actuator system is more accessible in that it is more cost effective and occupies only a benchtop footprint of roughly 1 sq. ft.

Other methods used to strain composite materials are most typically either droptest methods [66, 78] where a deadweight is dropped from a height to apply an impact force or a small oscillatory, force such as those used in Berlincourt type d_{33} PiezoMeters (such as PiezoTest's Model PM100 d33 PiezoMeter System). Droptests are heavily constrained in their ability to interact with samples in that they are only able to apply their force as accelerated by gravity and decelerated by the sample's modulus which can lead to very high or low strain values depending on the mass of the dropped object and the height from which it is dropped. The droptest method is more commonly used for soften, compressible piezoelectric composites or other piezoelectric materials that will not be damaged by the energy of the impact. Piezoemeters on the other hand are typically designed to only apply a very small strain, typically in the microstrain range. This had lead to this tool being ubiquitous for the measurement of conventional electroceramics materials where the larger strains that composite sensing materials are often subjected to would shatter their bulk counterparts. Piezometers have still been used to assess softer, composite materials though the piezoelectric charge coefficient values yielded for these microstrain measurements may differ from those when a composite is being strained at $> 10\%$ as piezoelectric coefficients begin to deviate under higher stains [7].

The voice coil actuator (VCA) system is an useful way to apply strains and forces to

piezoelectric composites as every interaction is able to be carefully controlled and monitored in order to assess the position, velocity, strain, strain-rate, and force of the interaction due to the VCA's onboard monitoring. This is coupled with MotionLab software by Ingenia to allow for those values to be collected, packaged, and exported to be processed as .csv files.

The position and values yielded by the VCA are some of the the most useful information provided by the linear actuator and software as that allows us to monitor in real-time the actuations between the linear actuator and the sample. After calibrating the known position of the linear actuator head and sample thicknesses, we are able to translate the position values into strain values and strain-rate values. As mentioned in Chapter 4, strain-rate can be a notable measurement due to the high charge leakage observed by this family of materials. A sufficient strain-rate is needed in order for charge generation to outpace the loss to result in a more measurable signal, typically dependent on the material's time-constant, τ. This particular VCA is able to measure its position to the nearest 1.6 microns via a digital, though, as measured above, the position can be controlled to a resolution of 10 microns.

The most significant characteristic for this system is the ability to design unique and relevant linear actuation curves that model real-world interactions where wearable sensors may be used. The 10 micron resolution can be used to simulate everything from a high speed impact to the compression that a shoe sole may feel during a step to the minute deflections that occur on skin due to a human heart pulse waveform. While oscillatory interactions are the simplest to implement, multi-stage interactions that simulate the multi-step pressure pulses from a heart beat could be simply created and implemented by the linear actuator system.

The velocity and force values provided by the linear actuator can be helpful in evaluating linear motion loops, though the Ingenia velocity measurements use an averaging algorithm that causes it to not be suitable for the 10-15 millisecond interaction. The force measurements, while useful for using the VCA applying a static force, are less useful for the rapid force measurements. Calibrated as received, the on-board force measurements are too low of resolution compared to other technologies to be of help in assessing the forces involved in the interaction between the linear

actuator and the sample.

While the voice coil linear actuator is a helpful tool there are other instruments that can be used for this process such as droptests, pneumatic systems, and other commercial electromagnetic slider automation systems. Droptests are a common method to apply an impact or strain to a material on account of the simplicity of the technique as has been used throughout the field for applying low to moderate amounts of force (1-100 N) [66, 78, 79]. Despite the simplicity, carefully selecting a dropweight and height can result in a large set of relevant data, though the deceleration and thus the strain-rate will be dependent only on the material's properties. This can make it challenging when looking for more controlled events such as those experienced by wearable sensors. Pneumatic and gun-type linear collision systems have also seen use when repeatably straining materials, though these also struggle with controlling the interaction [80, 81, 78]. The gold standard in this field is a high-end fatigue testing equipment setup such as the Instron ElectroPuls system which is capable of both accurately applying and observing strains across a variety of forces and rates. While these systems are able to perform a wide range of linear actuations, the large footprint and expense of these machines makes them inaccessible to many researchers. While more commonly found in many industrial settings for fatigue testing, these high speed dynamic testers are typically too niche to be found in many universities, even those with robust material characterization centers. An additional hurdle to conventional linear actuator systems such as the Instron is coupling in device output sensors into the sample stack as well setting up and maintaining the additional equipment needed for simultaneous measurement of electrical responses.

While there are many routes for applying a strain to material, measuring the resulting strain can still be challenging. If the system does not have a linear encoder capable of reporting accurate positioning values ($\sim$ 1 micron) at a sufficiently high sampling rate ($>$ 1 kHz) throughout the short interaction time ($\sim$ 5 ms), an additional set of equipment would be needed. One of the strongest technologies for this task is laser doppler imaging that can be found in commercial products such as LMI Technologies' Gocator 3D Laser Point Profile Sensors or those found in laser doppler vibrometry systems. While these systems can be effective at measuring applied strains at sufficient

frequency, maintaining a clear view of the sample in the region of actuation can be an obstacle, as can the cost of these systems.

5.2.1 Linear Motion Data Processing

Using the Ingenia MotionLab software, a linear motion curve can be set and monitored in real time. Using the Scope function of MotionLab, a difference between the designed motion curve and the actual motion curve should be observed due to the sample impeding the linear actuator's planned path. The linear actuator is designed to begin to apply addition Using the Scope function, the linear actuator position data is able to be sampled at as high as 1 kHz and exported in a .csv format. As mentioned earlier, while the MotionLab software provides velocity information, the averaging used smooths in a way that makes it unhelpful in characterizing the impact velocities over the 10-15 ms that the sample interaction takes place.

Once the positional data (P) is taken in, methods to identify when the linear actuator interacts or impacts with the sample. Taking the first and second derivatives of the position as a function of time (abbreviated as dP, d2P) allows us to look for changes in the velocity and the acceleration of the linear actuator. By identifying the points of peak deceleration in the second derivative of position with respect to time, the regions of impact can be identified. This is done through the 'findpeaks' MATLAB function and a threshold set as a multiple of the standard deviation acceleration values. Depending on the speed of the interaction, this threshold may need to be shifted in order and a minimum time separation of events implemented in order to capture the events of interest and avoid false events. For lower strain rate events, alternative methods such as manually flagging events may be needed as the velocity and acceleration shifts may be too shallow to adequately identify the events. Depending on the sampling rate and speed of interaction, an assessment of the impact velocity, peak strain, and strain rate can be determined. As the Ingenia Software and linear actuator are able to collect 700 ms of positional information at the sample rate of 1 kHz, several interaction events are able to be assessed together and their characteristics compared statistically.

5.3 Force Measurements

Assessing the force applied to a piezoelectric material of device is a critical component in determining their ability to output charge or voltage in response to a force or strain. In this characterization suite, a piezoresistive sensor and analog circuit (Tekscan FlexiForce A201-1 Sensor, FlexiForce Quickstart Board) fed into a digital oscilloscope (Rigol DS1054Z) are used. The FlexiForce sensor can be calibrated with a set of well characterized deadweights along with adjusting the onboard trimpot potentiometer in order to focus the range of the force sensor for the desired range that will be used. A common workflow for calibrating the force sensor is to subject the force sensor to the highest force that it would experience during the interaction, adjust the trimpot to read a 4.5 V output at that force (90% of the maximum output of 5 V for the circuit), then use the weights to calibrate the force sensor for that range to create a Force Input to Force Voltage calibration curve. This force sensor was chosen for its robustness, thin profile which allows it to be placed above and ability to be sampled at a high rate as the force circuit outputs a current proportional to the force applied to the piezoresistive sensor. While a FlexiForce piezoresistive sensor was chosen for this application, other force measurement tools such as load cells would be suitable as long as they are at a sampling rate suitable to fully characterize the interaction. Additionally, it is ideal to be able to sync temporally to the other measurements such as being collected on a common acquisition system.

5.3.1 Force Data Processing

Using the FlexiForce system and digital oscilloscope, we are able to export the force and time data in a .csv format to a program such as MATLAB for processing. Based on the calibration curve established for the current piezoresistive force sensor, the force voltage data (F) can be converted to force data (FN) and the differential taken with respect to time (dFN). While simply using the peak Force over the course of the measurement has often been used as the input force, the linear actuator-sample complete interactions can take place over a much longer period of time

than the total interaction event can be many multiples longer in time than the actual impact event which typically lasts ∼5 ms which is responsible for generating the observed voltage from these samples in this impact velocity range. In order to identify those events, flagging the peak differential force values (dFN) then searching neighboring points for the local peak forces in those regions, and identifying the pertinent time values should yield a more accurate value of the peak force of the interaction. This can then be combined with voltage or charge outputs to provide more accurate values throughout the dynamic interaction. The impact detection effect can help to avoid overestimating impact forces when measuring < 10 N events as shown in Figure 5.2.

5.4 Voltage Measurements

For a piezoelectric wearable sensor, one of the most commonly utilized outputs is the voltage that the device can generate. This is related directly to the piezoelectric charge that is generated though the ultimate voltage output is impacted by the capacitance that the sensor itself has along with downstream electrical components such as cabling and the voltage or charge monitoring equipment. Regardless, many applications prefer to monitor the voltage generated from sensors as it can both simply observed and then acted upon if a certain voltage threshold is met or not. In this characterization suite, a National Instruments USB-6212 digital acquisition (DAQ) unit and a Rigol DS1054Z 50 MHz bandwidth oscilloscope were used to collect voltage data that resulted from interaction events or impacts with the samples.

Both oscilloscopes and DAQ systems are suitable for collecting the voltage output from the device though the complete measurement circuit and monitoring system may result in differences in the observed voltage as well as a difference in noise level. For these specific pieces of equipment, the digital acquisition unit was preferred on account of its superior signal-to-noise ratio and for its ability to record, store, and export data at a higher rate than the on-hand oscilloscope.

In this testing suite, the linear actuator can be set to oscillate and repeatedly provide impacts with the material. This can be seen by the unfiltered device voltage response as a function of actuator

oscillation frequency (1 Hz = 8 mm/sec impact velocity in this case) as seen in Figure 5.3.

5.4.1 Voltage Data Processing

While data processing of voltage data can be one of the more straightforward steps as it can be interpreted as the direct output of the device, noise reduction or signal smoothing algorithms can be commonly used. As these devices are in essence a series of electrodes on long wires, they behave often similar to antennas leading to a high noise floor with multiple layers of overlapping rough noise. For a 10 Hz oscillation event cycle, the monitored voltage includes the device output, a 10 Hz artifact from the linear actuator being closer or further, a 60 Hz power systems artifact, as well as a 8985 Hz artifact likely due to linear actuator electronics.

These artifacts can be removed or limited via appropriate filtering algorithms such as notch filters or Savitzky-Golay filters. The goal of filtering is to remove the noise as much as possible while preserving the real signal of the device. Filtering composite piezoelectric devices can be challenging in particular as the signal output is broadband in nature. A well constructed notch filter can eliminate problematic frequencies effectively, but the Savitzky-Golay filter's smoothing operation is able to effectively reduce noise but also causes a reduction in the observed voltage peaks. Comparing the unfiltered and filtered signals is a critical step to evaluate the success of the filtering as well as the potential overfiltering of device output. The labeled impact of these filtering steps can be seen in Figure 5.4. Once appropriately de-noised, a peak identification algorithm can be used to determine the maximum and minimum voltage for each impact event.

5.5 Charge Coefficient Measurements

While many applications rely on measuring the voltage output of a piezoelectric device, the direct output is actually charge. This charge, after accounting for the capacitance of the total measurement system, will yield a voltage though circuit capacitance often can vary between system setups. As charge generation and the piezoelectric charge coefficients, d_{ij}, are material properties,

they are more often used by researchers and engineers to compare the output of their materials and devices. In order to measure the piezoelectric charge coefficient, resonance, static, or quasi-static methods can be used.

Resonance methods, as covered by the IEEE Standard[82], uses the converse effect of piezoelectrics to excite a response with an oscillating field at the sample's resonant frequency or elastic resonance while measuring the elongation strain of the material. Due to the polymer components of these composites, these minute strains can be challenging to measure accurately compared to bulk electroceramics without laser interfermertry such as in tools like laser doppler vibrometers. Even with access to these tools, other methods for charge measurement maThe material This was evidenced by attempts to activate and observe a foam-based piezoelectric composite with laser doppler vibrometry in the range of 1 Hz to 203 kHz at a voltage of 100 V. While a 30 nStrain or 30 pm surface extension was detected at 31 kHz on a 1 millimeter thickness sample, the associated piezoelectric coefficient at 0.3 pm/V, well below the values determined for the sample with the direct effect. Likely explanations are that the material was not excited at its peak resonant frequency or that the composite's low electromechanical coupling factor makes converse measurements of its piezoelectric charge coefficient challenging.

Static methods are used primarily to orient oneself to the crystallographic axes of a single-crystalline material, and while it is possible to determine charge coefficients with them, maintaining the fields, strains, and boundary conditions required can be difficult [82].

Quasi-static methods are by far the most widely used method for measuring the piezoelectric charge coefficient of piezoelectric composite materials [83, 84, 85, 86]. By the careful application or removal of a known force with the simultaneous capture of the resulting current, a measurement of the of relationship between charge output and stress can be made, a direct measurement of the piezoelectric charge coefficient.

Extremely slow or low-strain rate interactions (< 1 mHz, < 0.1 strain/sec) can be especially challenging for piezoelectric materials to measure due to the leakage current that exist that causes generated charges and currents to dissipate before they build up to more measurable levels [87].

Leakage currents of PVDF-PZT composites have been reported between 1 to 100 nA/cm^2 [88]. The quasi-static method of measuring piezoelectric materials is able to overcome this by capturing the current generated throughout the low-strain interaction. The limiting factor is the time-constant of the charge amplification circuit though sufficiently high impedance components are available to allow for the measurement of mHz events. The quasi-static method is also used in commercial d_{33} meters.

5.5.1 Charge Data Processing

A quasi-static method was used to collect the charge output of the piezoelectric device in a charge amplification circuit as explained by G. Gautschi [89], and as seen schematically in Figure 5.5. The circuit's capacitor, C1, was selected to be 100 pF and the resistor, R1 was selected to be 20 MΩ yielding an RC time constant, τ, of 2 ms. The cutoff frequency, $f_c = (2\pi\tau)^{-1} = 79.6$ Hz allows for the measurement of charge generation events as long a 12.6 ms. As the impact events occur over $\sim$ 5 ms, the circuit is appropriate for measuring the charge generated. The charge amplifier circuit then provides a voltage that is directly proportional to the charge collected on the capacitor which is collected by the DAQ. This voltage is then compared to the reference calibration from a commercial barium titanate electroceramic device; the calibration curve can be seen in Figure 5.6. This is then used to determine the piezoelectric charge coefficient of the sample. A direct integration of the current produced during the interaction would be an alternative and preferred method for determining the charge output of the interaction.

5.6 Conclusions

In order to help fuel the growing interest for piezoelectric composite materials in the wearable sensor space, the proposed system allows for the more accessible characterization of devices. Through the use of a voice coil linear actuator as well as force, voltage, and charge measurements, the piezoresponse of devices can be carefully measured during dynamic events

that better model real world usage by creating strain profiles that model events like breathing and walking. It is the hope that this will allow researchers to more readily be able to characterize and develop sensors when alternative instrumentation is inaccessible.

5.7 Acknowledgments

Chapter 5, in part, is being prepared for submission: Middlebrook, J and Sirbuly, D. *Accessible Piezoelectric Testing Suite for Composite Sensors in Wearable Applications*. The dissertation author was the primary investigator and author of this paper.

5.8 Figures

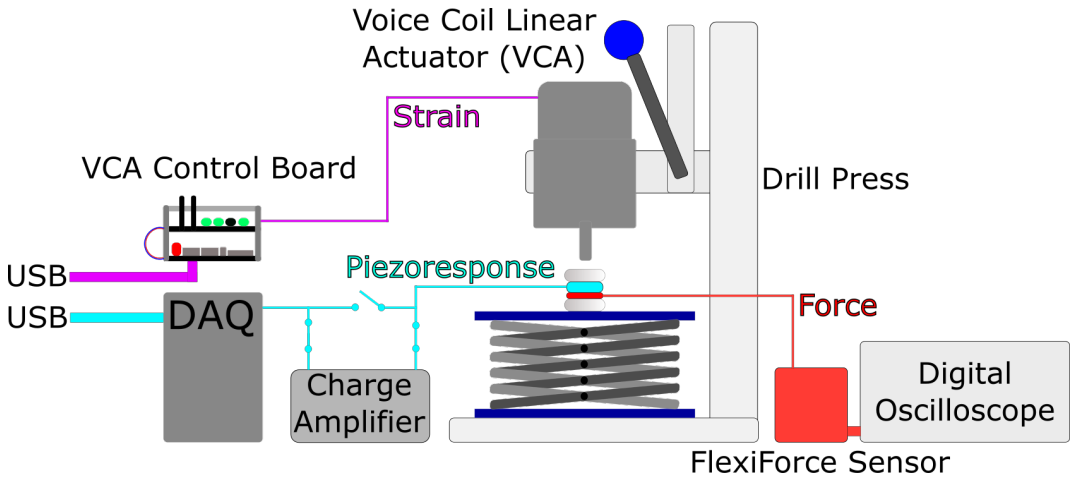

Figure 5.1: *Voice coil linear actuator based piezoelectric testing suite*
A voice coil linear actuator seated rigidly in a drill press stand with variable height is suspended over a laboratory scissors jack testbed. A test-stack of an acrylic spacer, piezoresistive force sensor, piezoelectric sample of interest, and acrylic spacer is held together in intimate contact with a pre-straining force under the voice coil linear actuator. The piezoresponse of the sample is send to a charge amplifier then a digital acquisition unit (DAQ) for piezoelectric charge measurements or directly to the DAQ for voltage measurements. Force measurements are taken by a FlexiForce A201-1 sensor coupled to a FlexiForce Quickstart board monitored by a digital oscilloscope. Positional data on the voice coil linear actuator is collected by its control board in order to provide information on position, stain, velocity, and strain-rate throughout the interaction.

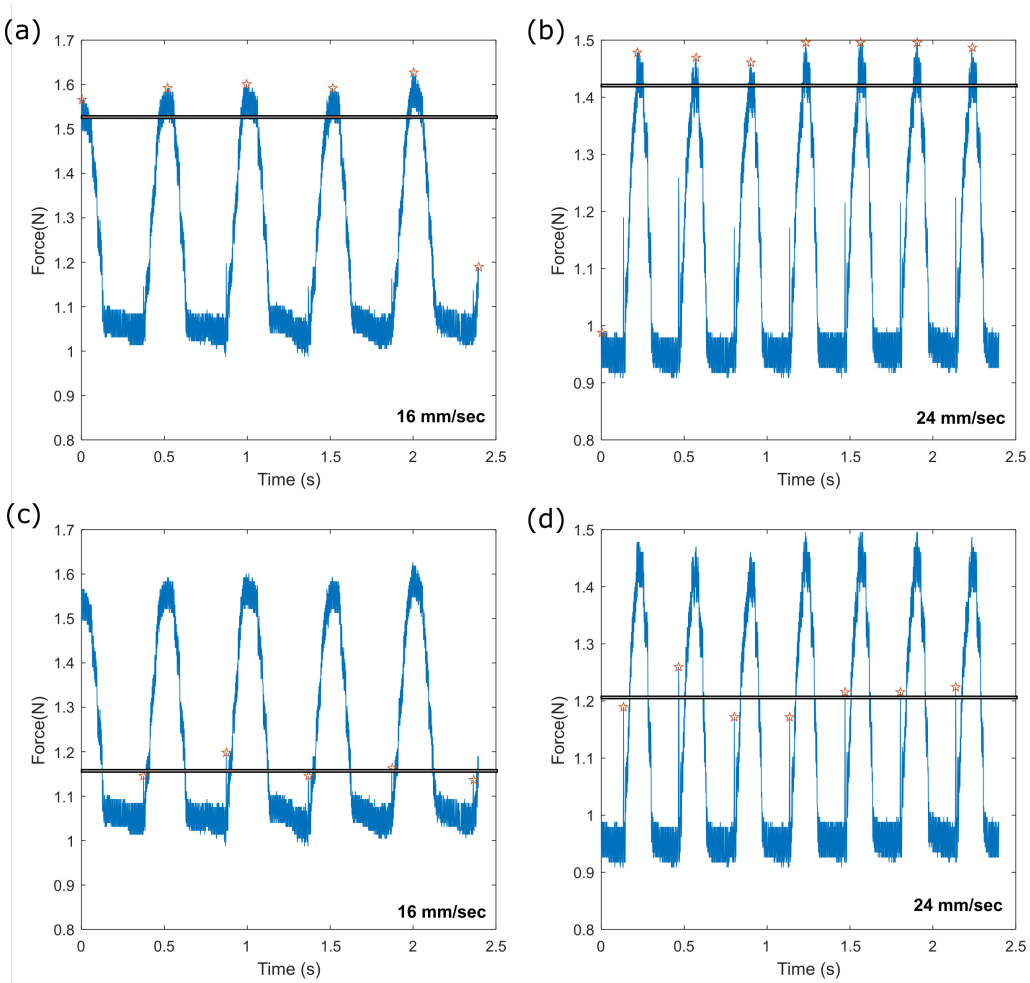

Figure 5.2: *Force detection comparison*
Force curves for interactions with a commercial barium titanate device at 16 mm/sec and 24 mm/sec with two peak impact force detection methods (star) with average detected force (black bar). Curves (a) and (b) look at the local peak force but overestimates the force by selecting the peak compression force rather than the impact force at the start of each interaction. Curves (c) and (d) use the described peak detection method to flag rapid changes in applied force to focus the peak detection algorithm providing a more accurate estimation of the impact force.

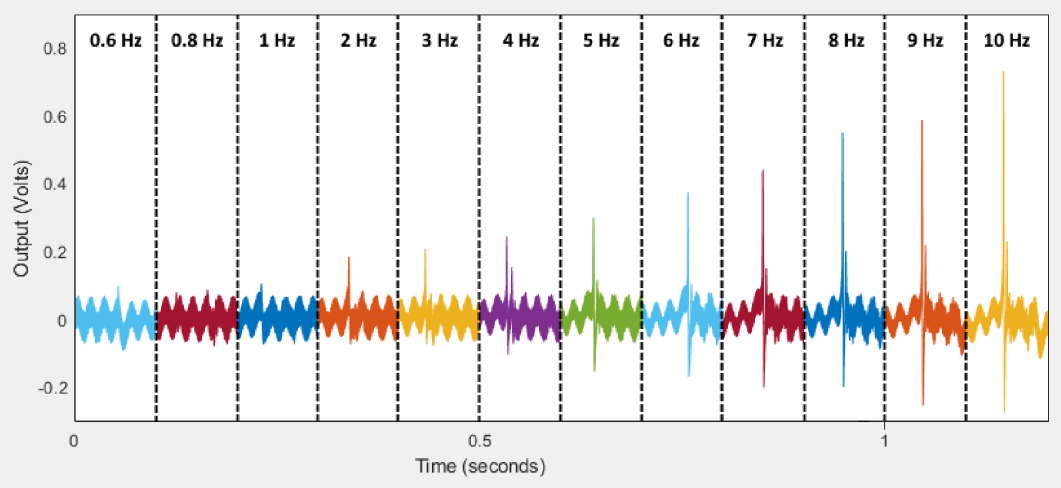

Figure 5.3: *Electrospun piezoelectric device voltage response to changing impact velocity*
Voltage response with no additional filtering. Voice coil linear actuator oscillation frequency for these measurements to be 8 mm/sec of impact velocity per Hz.

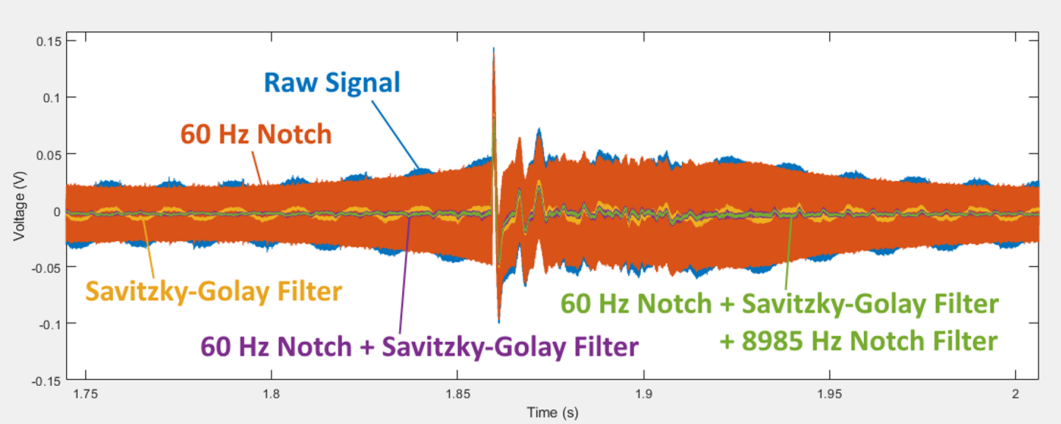

Figure 5.4: *Voltage output filtering*
The impact of filtering data processing steps on a the voltage output of an electrospun piezoelectric device. The original signal (Blue) along with the single after a 60 Hz Notch filter (Orange), a Savitzky-Golay filter (Yellow), the combination of the 60 Hz Notch filter and Savitzky-Golay filter (Purple), and the combination of a 60 Hz Notch filter, a 8985 Hz Notch filter, and a Savitzky-Golay filter.

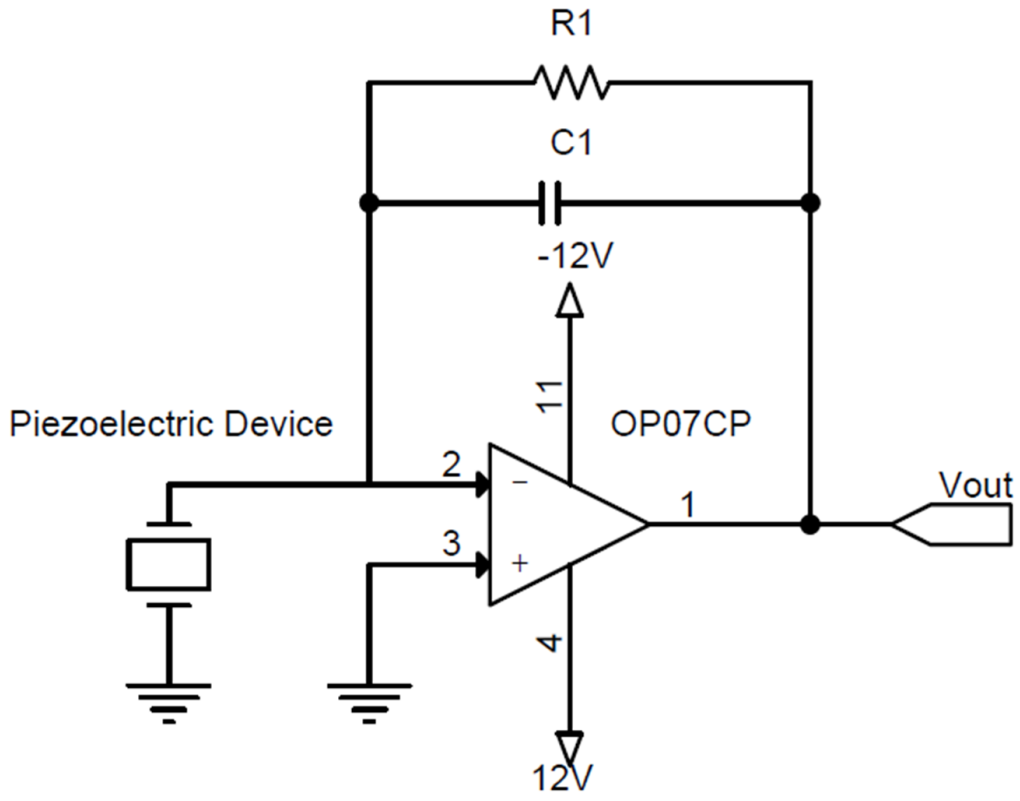

Figure 5.5: *Schematic of a Charge Amplifier Circuit*
Charge amplfier circuit for collecting a piezoelectric device's charge output on the circuit's capacitor, C1 = 100 pF. The circuit's resistor, R1 = 20MΩ, results in a RC time constant for the circuit, τ, of 2 ms and a cutoff frequency, $f_c = (2\pi\tau)^{-1}$ = 79.6 Hz.

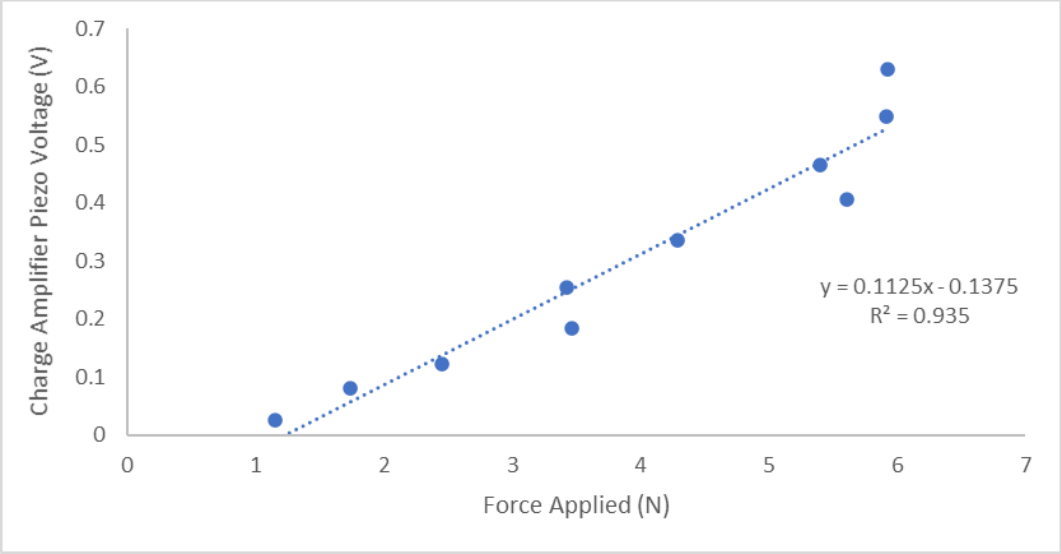

Figure 5.6: *Charge Amplifier Output Reference Calibration Curve*
A piezoelectric charge to force calibration curve created by measuring a commercial barium titanate electroceramic, d_{33} = 140 pC/N, device.

Chapter 6

Electrospun Piezoelectric Ceramic—Polymer Non-woven Mat Devices

6.1 Introduction

Barium titanate-polymer nanofiber non-woven mats are synthesized via electrospinning and fabricated as-spun into piezoelectric sensing devices. The electrospinning process yields a highly porous net-like composite structure that can hold additives such as barium titanate nanoparticles which are sealed in place during the device fabrication process. The non-woven mats are in-plane polarized via the electrospinning process, but performance was increased by re-polarizing the materials axially. Device charge output was collected to yield piezoelectric coefficients d_{31} of -10.5 ± 0.9 pC/N for in-plane polarized devices, though device performance was improved by axially re-polarizing the devices, yielding a d_{33} of 30.8 ± 3.0 pC/N. These devices were also shown to be capable of detecting human heartrate as a self-powered sensor with an electrical output that can be processed via Fast Fourier transform to determine a heartbeat-per-minute value. The porous net-like structure of the mats allows them to be a scaffold for additives to improve properties, shown here as a barium titanate nanoparticle dipcoating process which improved device sensitivity from 1.3 mV/N to 3.1 mV/N. This platform has the potential to expand the use of electrospun barium

titanate-polymer nanofiber devices in the wearable space as a flexible and versatile tool.

There is a growing trend for technology to be part of our everyday lives which is fueled, in part, by advances in wearable sensors and their ability to into our normal routines. Self-powered piezoelectric sensors and nanogenerators have been shown to be able to provide information and energy through impacts, fitness tracking, and biometrics [90, 91, 43]. While conventional, bulk piezoelectric electroceramics are capable of higher outputs than composites, their inflexibility and high moduli make them incompatible with many wearable sensing. There has been interest in exploring piezoelectric composite materials that allow for these useful sensing operations while overcoming the inflexibility and often lead-based nature of conventional bulk electroceramic piezoelectrics. While fully polymer based electrospun materials have already made their way into sensors, this work explores how electrospun barium titanate-polymer composites are able to be created and integrated into a sensing platform. The use of this ceramic-rich piezoelectric composite rather than a fully polymer based material allows for higher piezoelectric coefficients to be attained without losing the key flexibility that allows for expanded applications in the wearable space.

Electrospinning has been shown to a useful technique to form nanofibrous materials and piezoelectric materials [14]. The process, which uses a viscous liquid precursor and a large electric field to jet the fluid through the air, evaporating solvents to yield consistent, well defined nanofibers with controllable diameters and compositions [92]. By carefully developing the precursor and tuning electrospinning parameters, a number of pure polymer or polymer containing composites are able to be formed for applications from reinforcing composites to creating nanogenerators [93, 94, 17].

This work presents another form of piezoelectric composite material for these applications in the form of an electrospun barium titanate-polymer mat that can be easily created, harvested, and prepared into wearable sensors. Previous works have created barium titanate nanofibers through similar methods though the calcination process to remove the electrospinning polymer leaves the materials brittle, limiting applications [92, 17, 95]. By retaining the polyvinylpyrrolidone (PVP), we have produced a flexible non-woven mat of material that can be used as created, or as a porous scaffold to capture other materials as additives to the composite to either enhance or grant additional

properties to the composite. In addition to the materials' ability to generate voltages as a sensor, the figure of merit of piezoelectric charge coefficient, d_{ij}, the ability for the material to generate a charge in response to a stress [7] is also assessed. .

6.2 Methods

Precursor preparation: Barium acetate (1.275 g, Sigma Aldrich, [Ba(C2H3O2)2]) was added to glacial acetic acid (3 mL, Sigma Aldrich) and stirred until completely dissolved, approximately two hours. Titanium butoxide (1.715 g, $[Ti(O(CH_2)_3CH_3)_4]$, Sigma Aldrich, 97%) was added dropwise to the acetic acid solution while rapidly stirred and then allowed to continue to stir an additional 10 minutes. A separate solution was made by dissolving polyvinylpyrrolidone (0.200 g, 1.3 MDa, PVP, Sigma Aldrich) into ethanol (3 mL, Koptek, 99.9%) and then added to the stirred acetic acid solution. The combined solution was allowed to stir for 90 minutes before being loaded into a 3 mL disposable syringe for electrospinning.

Electrospinning: A syringe tip (20 AWG) was fixed to the syringe containing the nanofiber precursor and attached to polytetrafluoroethylene (PTFE) tubing (20 AWG, 0.86 mm ID). The metal section of a separate syringe tip removed, blunted, and attached to the other end of the PTFE tubing. The syringe was fixed to a syringe pump and the tubing threaded into an electrically insulated enclosure. A 30 kV power supply (Bertan Associates Inc. Model 210-30R) was connected to the metal syringe tip suspended in the enclosure and to a vertically oriented and suspended aluminum collection sheet. The syringe tip to sheet distance was set to 6.5 cm. Solution was fed through the tubing at a rate of 0.70 mL / hour. The power supply was then set to 9 kV creating an electric field between the syringe tip and collection sheet of 138 kV/m allowing the solution to electrospin for several hours until sufficient material was collected. The material and collection sheet were allowed to air dry over 48 hours before the barium titanate-polymer mats were harvested via biopsy punch (8 mm, Integra Miltex) yielding 8 mm wide discs of material 220 ± 20 μm in thickness. The morphology of the composites was examined by scanning electron microscopy, the polymer content

was examined by gravimetric analysis, and the crystallography of the barium titanate was examined by X-ray diffraction and Raman spectroscopy showing successful formation of the ceramic with a tetragonal Raman peak (See Supplemental Information).

Dipcoating: For samples that were dipcoated in barium titanate nanoparticles aggregates, dried barium titanate-polymer nanofiber mats were carefully transferred to a solution of barium titanate nanoparticles (1g, 200 nm, US Research Nanomaterials, Inc) dispersed in ethanol (10 mL, Koptek, 99.9%). The solution and mats were gently stirred on a stirplate for 15 minutes allowing for nanoparticle aggregates to settle into the mats. The mats were then removed and allowed to dry in an oven at 50 deg C for 6 hours. The impact of dipcoating on mat morphology and ceramic was examined by scanning electron microscopy and by gravimetric analysis.

Repolarization: Once dried, the barium titanate-polymer nanofiber mats were transferred to a polyimide film lined polarization chamber where samples were polarized under an electric field (4 MV / m, Bertan Associates Inc. Model 210-30R) at an elevated temperature of 110 °C for 16 hours. The electric field was maintained during temperature ramp up and cooldown. This allowed for a reorientation of the barium titanate crystal domains to be parallel to the axis of stress application and the evaluation of the material's d_{33} value. All samples were allowed a minimum of 72 hours after repolarization before any electrical measurements were taken.

Device Fabrication: Electrodes for the devices were prepared by laser cutting polyethylene terephthalate films coated in an indium tin oxide conductive layer to size (Thor Labs, sheet resistance of 350-500 Ω/sq, 200 μm sheet thickness). A two-part thermally cured silver epoxy (Epoxy Technology, EPO-TEK H20S) was then used to anchor connection wires (Bulk Wire, PTFE High Temperature Stranded Wire, 30 AWG) into the conductive film. A thin layer of room-temperature-vulcanizing silicone (Momentive, RTV108) was applied to a top and to a bottom electrode, leveled to a thickness of 60 microns with a razorblade tape casting method, and a sample of the barium titanate-polymer nanofiber mat sandwiched between. Excess silicone was wiped away, and the samples were compressed with 5 N of static force which allowed for the adhesive to penetrate into the porous nanofiber mats for 72 hours while curing in ambient conditions.

Droptest: The impact sensing ability of the devices was measured by a purpose-built droptest setup. A drop tower was constructed that allowed the sample to be suspended between insulating layers of acrylic below a weighted droprod. A prestraining force (2 N) was used to keep the stack in full contact. The open circuit voltage output was monitored via a digital oscilloscope (Rigol DS1054Z) with the electrode opposite the impact (bottom electrode) being the monitored lead and the impacted electrode (top electrode) being the reference. The input peak force and force during the collision event was monitored by a piezoresistive sensor and circuit (Tekscan FlexiForce A201-1 Sensor, FlexiForce Quickstart Board) fed into a digital oscilloscope (Rigol DS1054Z).

Piezoelectric Charge Generation: The piezoelectric charge generation ability of the devices was measured by a purpose-built charge amplifier (or charge meter) and linear actuator setup. The charge amplifier uses a high inner gain and insulation resistance to yield a voltage output proportional to the charge generated by the device. The device was centered below the linear actuator and suspended between insulating layers of acrylic. A prestraining force (2 N) was used to keep the stack in full contact. Forces were applied by the sinusoidally oscillating linear actuator in tests that ranged between 1-5 N. The input peak force and force during the collision event was monitored by a piezoresistive sensor and circuit (Tekscan FlexiForce A201-1 Sensor, FlexiForce Quickstart Board) fed into a digital oscilloscope (Rigol DS1054Z)

Biosensing: The ability for the devices to monitor human heart rate was measured by a differential amplifier setup (A-M Systems, Inc. Model 3000, 1 Hz High Pass, 10 kHz Low Pass) into a Digital Oscilloscope (Rigol DS1054Z). The device was sterilized with ethanol wipes and allowed to air dry. The device was seated on the neck over the carotid artery and held in place with two inches of labeling tape (Fischerscientific Time Tape) which applied a small prestraining force to maintain full contact. The heart rate was then monitored by the device while the subject held still.

6.3 Results

The composite nanofibers yielded by the electrospinning process collected on the aluminum collection plate as a non-woven mat in layers similar to paper products. A single layer could be lifted from the material via a polydimethylsiloxane (PDMS) stamping method to demonstrate how the composite material can be strained under tension (see Supplemental Figure 1). Scanning electron microscopy revealed that the composite fibers were 380 ± 240 nm in width. A biopsy punch of several layers of the collected nanofibers yielded a flexible disc of the nanofiber mat that could be processed into a device. While the polyvinylpyrrolidone (PVP) polymer component could be removed at this stage in order to improve barium titanate grain size and crystallinity, calcined samples proved incredibly brittle and unable to be incorporated into a flexible sensing device. Maintaining the polymer component allows the material to maintain flexibility for wearable sensing operations. For the design of the sensing device, the flexibility and robustness of the interfacing and electrodes were of importance. While there has been significant progress in recent years on making strainable, skin-like electrodes [96], a commercial option of a flexible, transparent electrode of indium tin oxide deposited on polyethylene terephthalate was chosen for its durability and ease of processibility. As delamination of devices is a common source of failure, a room temperature vulcanizing adhesive was used that could be very thinly be spread via a tape casting method, high peel and shear strength (7 kg/cm, 14 kg/cm^2), and low dielectric constant (2.8 @ 60 Hz) [97]. The device was assembled as shown in Figure 1c and 1d, compressed, and cured in place with a total device thickness measured by micrometer to be 650 ± 15 μm.

6.3.1 Piezoelectric Charge Generation

The piezoelectric charge generation of the electrospun nanofiber mat device was measured via a charge amplification circuit that collected and measured the charge output of the devices under an oscillating impact force of 4 N in order to determine a piezoelectric charge coefficient, d_{31}, of 30.8 ± 3.0 pC/N. The inplane-polarized device had nanofibers with barium titanate crystal

domains that were aligned during the electrospinning process similar to previously described methods [98, 99]. As all crystal domains were aligned in-plane, perpendicular to the impacting force, this would qualify this value to be the d_{31} coefficient. This value This was compared with a device whose mat was not repolarized. The inplane-polarized device had nanofibers with barium titanate crystal domains that were aligned during the electrospinning process similar to methods previously reported. [98], allowing the measurement of a its piezoelectrical charge coefficient, d_{31}, of -10.5 ± 0.9 pC/N. The d_{33} value for barium titanate nanofiber mat agrees with previously reported values for calcined barium titanate electrospun nanofibers that had not been incorporated into a device piezoelectric coefficient which had been determined by piezoforce microscopy to be as high as 76 pC/N, increasing with nanofiber diameter [95]. The d_{33} and d_{31} values found for in-plane polarized and repolarized electrospun barium titanate-polymer mat devices have a proportion that is consistent with other values reported for barium titanate piezoelectrics. The piezoelectric charge coefficient reported here is comparable to fully polymer based electrospun sensing devices such as polyvinylidene fluoride (PVDF) with d_{33} = 33 pC/N [100] as well as barium titanate-PVDF and barium titanate-P(VDF-TrFE) composite with d_{33} = 25 pC/N and d_{33} = -25 pC/N, respectively [101, 102].

6.3.2 Dipcoating Process and Droptest Measurement of Impacts

The ability for the porous, net-like structure of the electrospun barium titanate nonwoven mat to be used as a scaffold for additives was tested by dipcoating the mat in an ethanol-barium titanate nanoparticle solution. Barium titanate nanoparticle aggregates were able to physically adsorb onto the surface of the nanofibers resulting in a dry weight increase of the nanoparticle mats of 45 ± 5%. The impact of this step was then measured by testing dipcoated and non-dipcoated mat devices' ability to detect and sense impact forces. Droptests of a weighted droprod onto each device was used to apply forces between 5-75 N at impact while the device voltage output was monitored. The voltage output (peak-to-peak) and peak collision force were plotted for each device to determine the sensor output over the force range, as seen in Figure 2 along with example

voltage and force waveforms over the course of the impact duration (4 milliseconds). While both non-dipcoated and dipcoated devices were successfully able to impact detect, the process improved the device sensitivity from 1.3 mV/N to 3.1 mV/N over the measured force range, an increase of 140%, with high linearity for both with R^2 values of 0.925 and 0.949, respectively. Individual impact response curves at 23 N peak force for each device can be found in the Supplemental Information. The increase in signal can be attributed to the dipcoated sample's increase in barium titanate weight percentage as well as the resulting increase in mat stiffness, both of which have been shown previously to increase nanocomposite piezoresponse [59]. While the addition of piezoelectric material is shown, other materials such as magnetostrictive cobalt ferrite nanoparticles could be added in order to yield a composite with combination properties with magnetoelectric effects [11].

6.3.3 Biosensing of Human Heart Rate

The flexible, robust nature of the electrospun barium titanate-polymer nanofiber mat device allows for it to be used for biosensing applications. This was tested by using it as a heart rate sensor while placed over an at-rest subject's carotid artery while the voltage was passed through a differential amplifier and monitored by a digital oscilloscope. A clear voltage signal in response to the heart rate was able to be observed under these conditions, and a fast Fourier transform was performed to determine the heart rate – in this case, 81 beats per minute. While heart rate sensing has been shown for piezoelectric materials such as a lead zirconate titanate slurry deposited on stainless steel [86], the electrospun fibers of this material could ultimately lead to devices with improved sensitivity. This enhancement in sensitivity compared to other forms of piezoelectric composite materials such as polymer-ceramic foam based composites [66] is consistent with electrospun poly(vinylidenefluoride-co-trifluoroethylene) materials where that are sensitive to pressures as low as 0.1 Pa due to the force concentrating ability of electrospun nanofiber materials [16].

6.4 Conclusions

In this work we have been able to show the production of barium titanate-polymer nonwoven nanofiber mats and their integration into impact and biosensing devices. The charge generation ability for the device was found to be 30.8 ± 3.0 pC/N, and the open-circuit voltage generation force sensitivity was improved 140% by the addition of barium titanate nanoparticle aggregates into the porous structure of the mesh. This platform can lead to the integration of various other additives in order to allow this class of devices to better assess impacts as well as biosensing.

6.5 Acknowledgments

Chapter 6, in full, is being prepared for submission: Middlebrook, J, Wei, W., Cho, Y. and Sirbuly, D. *Electrospun polymer-ceramic piezoelectric composite nanofiber mats for sensing applications*. The dissertation author was the primary investigator and author of this paper.

6.6 Figures

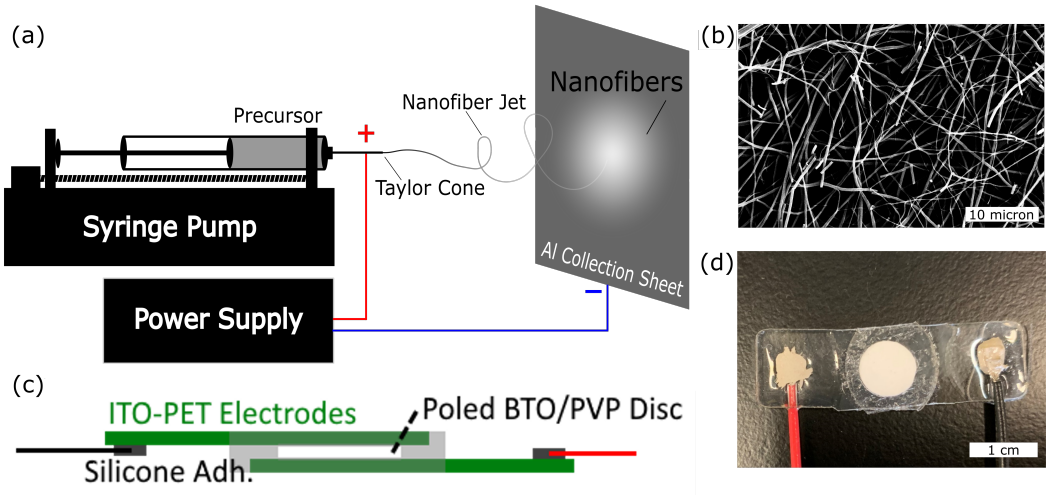

Figure 6.1: *Schematics of electrospinning setup and electrospun composite sensing device, scanning electron micrograph of as-spun barium titanate-polymer nanofibers, and optical image of electrospun composite sensing device*
a) Schematic of electrospinning setup for fabricating unwoven barium titanate-polymer nanofiber mats. b) Scanning electron micrograph of as-spun barium titanate-polymer nanofibers, scale bar of 10 microns. c) Schematic of device fabricated with unwoven barium titanate (BTO)-polymer (PVP) disc, indium tin oxide (ITO) deposited on polyethylene terephthalate (PET) electrodes, and a room temperature vulcanzing silicone adhesive to bind the device d) optical image of fabricated device, scale bar of 1 cm.

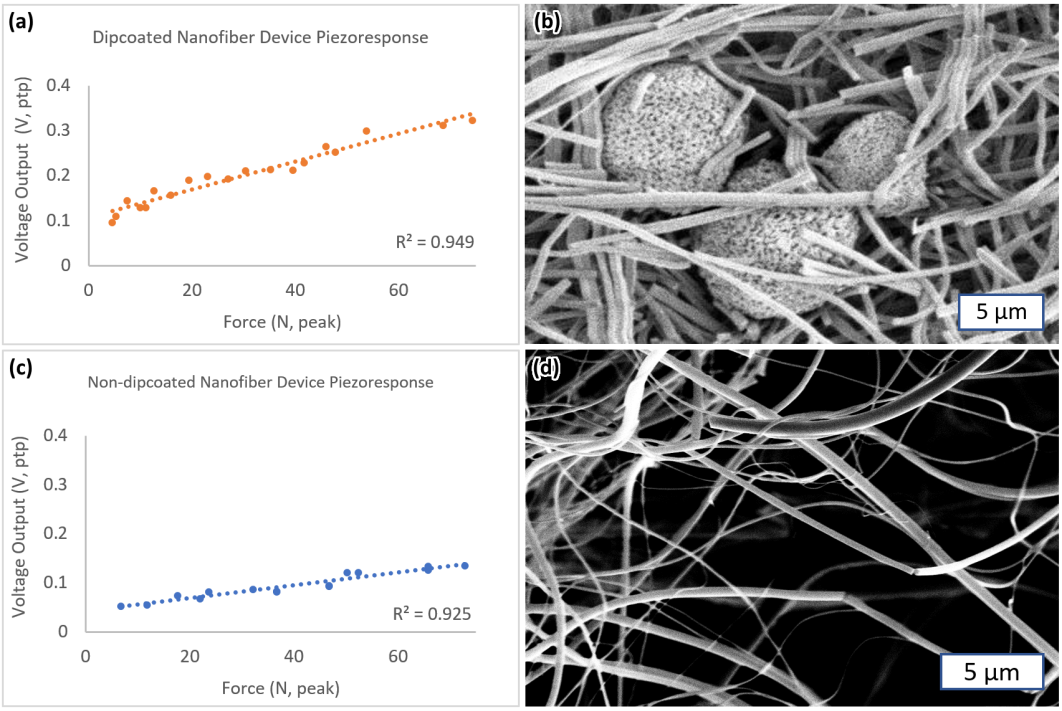

Figure 6.2: *Device piezoresponse and scanning electron micrographs of barium titanate nanoparticle dipcoated nanofibers and non-dipcoated nanofibers*
Piezoresponse to impact forces for barium titanate nanoparticle aggregate nanofiber mat devices for a) dipcoated devices and c) non-dipcoated mat devices. Scanning electron micrographs of barium titanate-polymer mats b) with dipcoating e) and without.

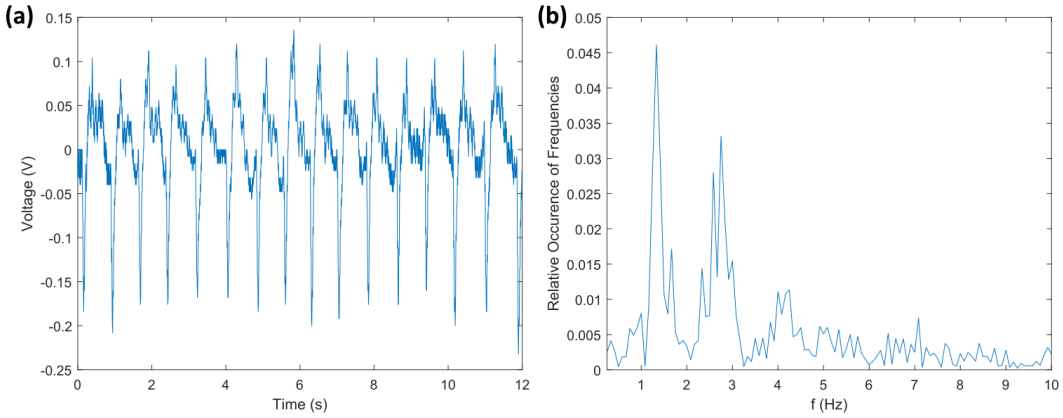

Figure 6.3: *Human heartrate biosensing voltage response and frequency spectrum of non-dipcoated ceramic-polymer composite nanofiber mat device*
Biosensing of human heartrate for a non-dipcoated barium titanate-polymer nanofiber placed on the neck over the carotid artery. a) Device output voltage in response to human heart rate, collected by differential amplifier (A-M Systems, Inc. Model 3000, 1 Hz High Pass, 10 kHz Low Pass) and digital oscilloscope. b) Fast Fourier transformation of device electrical output with a relative occurrence of frequencies peak of 1.35 Hz or 81 heart beats per minute.

6.7 Supplimental Figures

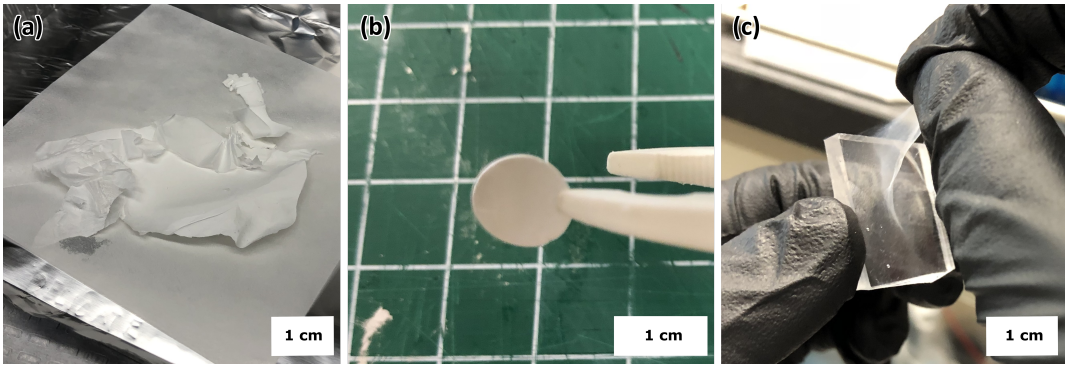

Figure 6.4: *Optical images of as-spun electrospun sheet, punch of electrospun material prior to integration into a device, and a single-layer sheet being hand stretched*
Optical images of (a) as-spun electrospun ceramic-polymer nanofiber nonwoven sheet prior to being punched into discs, (b) 8 mm wide disc of punched electrospun mat prior to polarization or being assembled into a device, and (c) a single layer of the electrospun material that was extracted from the as-spun material in via a polydimethylsiloxane stamping method and hand stretched to show the material's ability to be strained and flexed without breaking.

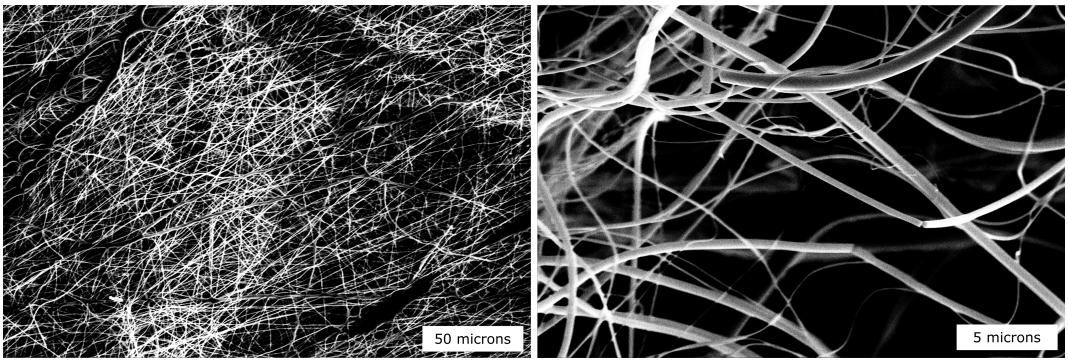

Figure 6.5: *Scanning electron micrographs of as-spun barium titanate-polymer composite nanofibers*
Material viewed with a Zeiss Sigma 500 SEM at an accelerating voltage of 10.00 kV and a current of 0.1 nA.

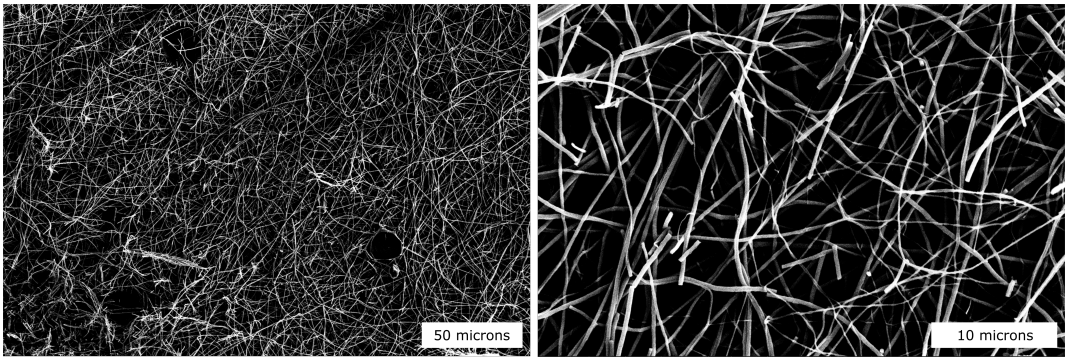

Figure 6.6: *Scanning electron micrographs of calcined barium titanate electrospun nanofibers*
As-spun nanofibers were calcined at 800 deg. C for 4 hours to remove the organic phases and improve the crystallinity of the barium titanate nanofibers. Material viewed with a Zeiss Sigma 500 SEM at an accelerating voltage of 10.00 kV and a current of 0.1 nA.

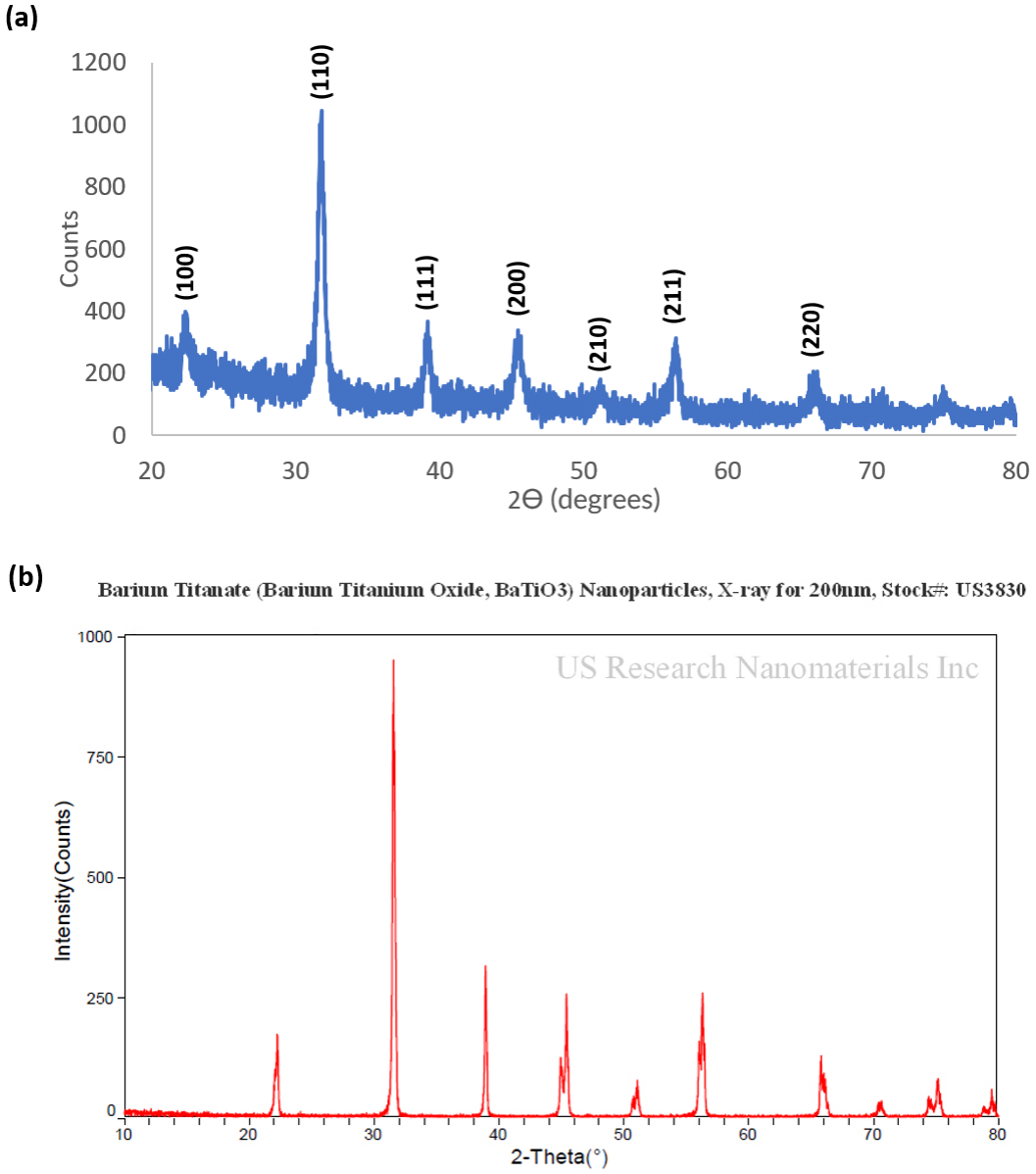

Figure 6.7: *X-Ray diffraction spectrums of calcined barium titanate nanofibers and barium titanate nanoparticle dipcoating additives*
X-ray diffraction (XRD) spectrums of (a) calcined barium titanate nanofibers, recorded from 10 to 80 degrees at a 0.01 degree stepsize and (b) XRD for the commercially sourced barium titanate nanoparticles used (US Research Nanomaterials Inc, 200 nm, Stock US3830) provided by the manufacturer [103].

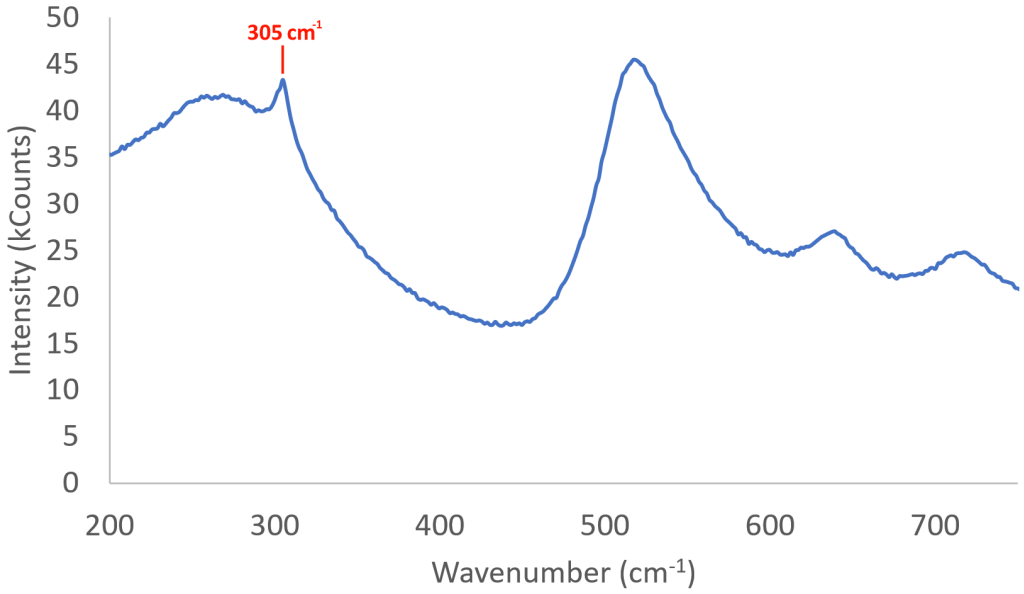

Figure 6.8: *Raman spectrum of calcined barium titanate nanofibers*
Raman spectrum of calcined barium titanate nanofibers. Highlighted in red is the 305 cm-1¬¬ Raman peak that is indicative of the B1 vibration mode for the barium titanate tetragonal phase [104]. Excited at 488 nm, 10 second exposure at 0.25 mW, 10 scan averaging, with Renishaw inVia confocal Raman microscope.

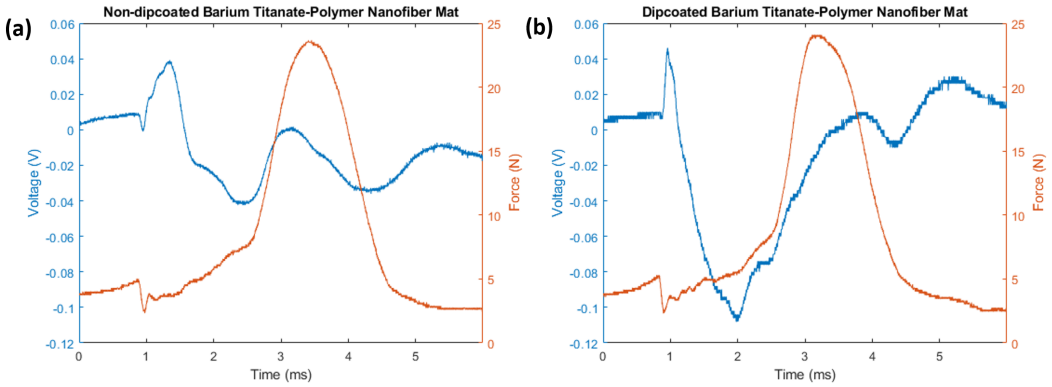

Figure 6.9: *Droptest piezoresponse voltage and force waveforms for non-dipcoated and dipcoated barium titanate-polymer nanofiber mat devices*
Droptest waveforms for device piezoresponse voltage output (blue) and impact force measurement (orange) for (a) non-dipcoated barium titanate-polymer nanofiber mat device and a (b) dipcoated mat device.

Chapter 7

Conclusions

7.1 Summary of Work

Piezoelectric composite materials and devices is a growing field of interest, potential, and investment. The goals set out in this dissertation were to attempt to understand the mechanical limitations of piezoelectric materials, how those can be overcome through the use of composites, and how chemistries and engineering may serve to improve upon those composites to attempt to bridge the electrical gap left in between.

In Chapter 2, it was demonstrated that the piezoelectric performance of optically printed (0—3) piezoelectric nanocomposites is strongly dependent on parameters such as surface linker chemistry, matrix mechanical properties, and nanoparticle size. With continued investigation on the strengthening and maximization of the stress-transfer efficiency at the inorganic-organic interface, it should be possible to fabricate composite materials with properties that exceed their ceramic monolith counterparts with less active material. Finally, optical printing with UV-curable polymers has been shown to be an ideal platform to systematically study and tune the piezoelectric properties of nanocomposites and offers one of the only routes to high precision, rapid, and 3D fabrication of piezoelectric polymers.

Chapter 3 highlighted the development of optically printed piezoelectric polymer–barium

titanate composites into a thin, flexible, and self-powered arrayed force sensor.Leveraging the ability to print extremely thin materials as well as being able to tune the mechanical, optical, and electrical properties of matrix and composite, this allowed for the platform to be able to be integrated into a space suit lining in order to measure and better understand human–space suit interactions.

The compressible foam piezoelectric materials discussed in Chapter 3 were shown to be capable of providing unique sensing solutions to the wearable space. From the initial work with polydimethylsiloxane, substantial improvements in performance, processability, and tunability have been shown by modifying the composition of the foam material and continuing to develop the integration of the material into sensing devices.

In order to help fuel the growing interest for piezoelectric composite materials in the wearable sensor space, Chapter 5 proposed a system allows for the more accessible characterization of devices in that area. Through the use of a voice coil linear actuator as well as force, voltage, and charge measurements, the piezoresponse of devices can be carefully measured during dynamic events that better model real world usage by creating strain profiles that model events like breathing and walking. It is the hope that this will allow researchers to more readily be able to characterize and develop sensors when alternative instrumentation is inaccessible.

Chapter 6 showed the production of barium titanate-polymer nonwoven nanofiber mats as well as their integration into impact and biosensing devices. The charge generation ability for the device was found to be 58 ± 10 pC/N, and the open-circuit voltage generation force sensitivity was improved 140% by the addition of barium titanate nanoparticle aggregates into the porous structure of the mesh. This platform can lead to the integration of various other additives in order to allow this class of devices to better assess impacts as well as biosensing.

Bibliography

[1] Morris H. Shamos, Leroy S. Lavine, and Michael I. Shamos. Piezoelectric Effect in Bone. *Nature*, 197(4862):81–81, January 1963. Number: 4862 Publisher: Nature Publishing Group.

[2] R. Bechmann. Elastic and Piezoelectric Constants of Alpha-Quartz. *Physical Review*, 110(5):1060–1061, June 1958. Publisher: American Physical Society.

[3] C. Lu and A. W. Czanderna. *Applications of Piezoelectric Quartz Crystal Microbalances*. Elsevier, December 2012. Google-Books-ID: cs9CXKuDbPQC.

[4] Eric J Schlosser. Piezoelectric igniter apparatus for gas grill, November 24 1981. US Patent 4,302,181.

[5] Amir Manbachi and Richard SC Cobbold. Development and application of piezoelectric materials for ultrasound generation and detection. *Ultrasound*, 19(4):187–196, 2011.

[6] R. Zeng, K. W. Kwok, H. L. W. Chan, and C. L. Choy. Longitudinal and transverse piezoelectric coefficients of lead zirconate titanate/vinylidene fluoride-trifluoroethylene composites with different polarization states. *Journal of Applied Physics*, 92(5):2674–2679, August 2002. Publisher: American Institute of Physics.

[7] B. Jaffe, W. R. Cook Jr., and H. Jaffe. *Piezoelectric Ceramics*. Academic Press Inc, New York, NY, 1971.

[8] Jean-Michel Kiat, Yoshiaki Uesu, Brahim Dkhil, Masaaki Matsuda, Charlotte Malibert, and Gilbert Calvarin. Monoclinic structure of unpoled morphotropic high piezoelectric pmn-pt and pzn-pt compounds. *Phys. Rev. B*, 65:064106, Jan 2002.

[9] S. Bhagavantam and D. Suryanarayana. Crystal symmetry and physical properties: application of group theory. *Acta Crystallographica*, 2(1):21–26, Mar 1949.

[10] Jon F. Ihlefeld. Chapter 1 - Fundamentals of Ferroelectric and Piezoelectric Properties. In Uwe Schroeder, Cheol Seong Hwang, and Hiroshi Funakubo, editors, *Ferroelectricity in Doped Hafnium Oxide: Materials, Properties and Devices*, Woodhead Publishing Series in Electronic and Optical Materials, pages 1–24. Woodhead Publishing, January 2019.

[11] R. E. Newnham. Composite electroceramics. *Ferroelectrics*, 68(1):1–32, January 1986.

[12] Vlad Alexandru Lukacs, Roxana Stanculescu, Lavinia Curecheriu, Cristina Elena Ciomaga, Nadejda Horchidan, Cipriana Cioclea, and Liliana Mitoseriu. Structural and functional properties of BaTiO3 porous ceramics produced by using pollen as sacrificial template. *Ceramics International*, 46(1):523–530, January 2020.

[13] Khaled S Ramadan, D Sameoto, and S Evoy. A review of piezoelectric polymers as functional materials for electromechanical transducers. *Smart Materials and Structures*, 23(3):033001, March 2014.

[14] Zheng-Ming Huang, Y.-Z. Zhang, M. Kotaki, and S. Ramakrishna. A review on polymer nanofibers by electrospinning and their applications in nanocomposites. *Composites Science and Technology*, 63(15):2223–2253, November 2003.

[15] Shaohua Jiang, Yiming Chen, Gaigai Duan, Changtong Mei, Andreas Greiner, and Seema Agarwal. Electrospun nanofiber reinforced composites: a review. *Polymer Chemistry*, 9(20):2685–2720, 2018.

[16] Luana Persano, Canan Dagdeviren, Yewang Su, Yihui Zhang, Salvatore Girardo, Dario Pisignano, Yonggang Huang, and John A. Rogers. High performance piezoelectric devices based on aligned arrays of nanofibers of poly(vinylidenefluoride-co-trifluoroethylene). *Nature Communications*, 4:1633, 2013.

[17] Junhan Yuh, Juan C. Nino, and Wolfgang M. Sigmund. Synthesis of barium titanate (BaTiO3) nanofibers via electrospinning. *Materials Letters*, 59(28):3645–3647, December 2005.

[18] Ebru Mensur Alkoy, Canan Dagdeviren, and Melih Papila. Processing conditions and aging effect on the morphology of pzt electrospun nanofibers, and dielectric properties of the resulting 3–3 pzt/polymer composite. *Journal of the American Ceramic Society*, 92(11):2566–2570, 2009.

[19] Chris Bowen. High piezoelectric sensitivity and hydrostatic figures of merit in unidirectional porous ferroelectric ceramics fabricated by freeze casting. 2019.

[20] Kenji Uchino, Eiji Sadanaga, and Terukiyo Hirose. Dependence of the crystal structure on particle size in barium titanate. *Journal of the American Ceramic Society*, 72(8):1555–1558, 1989.

[21] Kanguk Kim, James L. Middlebrook, Jeffrey E. Chen, Wei Zhu, Shaochen Chen, and Donald J. Sirbuly. Tunable Surface and Matrix Chemistries in Optically Printed (0–3) Piezoelectric Nanocomposites. *ACS Applied Materials & Interfaces*, 8(49):33394–33398, December 2016.

[22] Huachen Cui, Ryan Hensleigh, Desheng Yao, Deepam Maurya, Prashant Kumar, Min Gyu Kang, Shashank Priya, and Xiaoyu (Rayne) Zheng. Three-dimensional printing of piezoelectric materials with designed anisotropy and directional response. *Nature Materials*, 18(3):234–241, March 2019.

[23] M. J. Moody, C. W. Marvin, and G. R. Hutchison. Molecularly-doped polyurethane foams with massive piezoelectric response. *Journal of Materials Chemistry C*, 4(20):4387–4392, 2016.

[24] Martynas Sborikas and Michael Wegener. Cellular-foam polypropylene ferroelectrets with increased film thickness and reduced resonance frequency. *Applied Physics Letters*, 103(25):252901, December 2013.

[25] Takeo Furukawa, Koji Fujino, and Eiichi Fukada. Electromechanical Properties in the Composites of Epoxy Resin and PZT Ceramics. *Japanese Journal of Applied Physics*, 15(11):2119, November 1976. Publisher: IOP Publishing.

[26] T. Furukawa, K. Ishida, and E. Fukada. Piezoelectric properties in the composite systems of polymers and PZT ceramics. *Journal of Applied Physics*, 50(7):4904–4912, July 1979.

[27] C. K. Wong, Y. M. Poon, and F. G. Shin. Explicit formulas for effective piezoelectric coefficients of ferroelectric 0-3 composites. *Journal of Applied Physics*, 90(9):4690–4700, November 2001.

[28] Michihito Ueda, Yukihiro Kaneko, Yu Nishitani, and Atsushi Omote. Battery-less shock-recording device consisting of a piezoelectric sensor and a ferroelectric-gate field-effect transistor. *Sensors and Actuators A: Physical*, 232:75–83, August 2015.

[29] Nirmal Prashanth Maria Joseph Raj, Nagamalleswara Rao Alluri, Venkateswaran Vivekananthan, Arunkumar Chandrasekhar, Gaurav Khandelwal, and Sang-Jae Kim. Sustainable yarn type-piezoelectric energy harvester as an eco-friendly, cost-effective battery-free breath sensor. *Applied Energy*, 228:1767–1776, October 2018.

[30] X. Ma, B. Zhou, and S. F. Xue. Investigation on Actuation Performance of Continuous Fiber Reinforced Piezoelectric Composite Actuator. *Journal of Mechanics*, 36(3):273–284, June 2020. Publisher: Cambridge University Press.

[31] Shuaidi Zhang, Hu Liu, Shuaiyuan Yang, Xianzhang Shi, Dianbo Zhang, Chongxin Shan, Liwei Mi, Chuntai Liu, Changyu Shen, and Zhanhu Guo. Ultrasensitive and highly compressible piezoresistive sensor based on polyurethane sponge coated with a cracked cellulose nanofibril/silver nanowire layer. *ACS applied materials & interfaces*, 11(11):10922–10932, 2019.

[32] Yanan Ma, Nishuang Liu, Luying Li, Xiaokang Hu, Zhengguang Zou, Jianbo Wang, Shijun Luo, and Yihua Gao. A highly flexible and sensitive piezoresistive sensor based on MXene with greatly changed interlayer distances. *Nature Communications*, 8(1):1207, October 2017. Number: 1 Publisher: Nature Publishing Group.

[33] Lei Gao, Chengxian Zhu, Lin Li, Chengwu Zhang, Jinhua Liu, Hai-Dong Yu, and Wei Huang. All Paper-Based Flexible and Wearable Piezoresistive Pressure Sensor. *ACS Applied Materials & Interfaces*, 11(28):25034–25042, July 2019. Publisher: American Chemical Society.

[34] Ningqi Luo, Wenxuan Dai, Chenglin Li, Zhiqiang Zhou, Liyuan Lu, Carmen C. Y. Poon, Shih-Chi Chen, Yuanting Zhang, and Ni Zhao. Flexible Piezoresistive Sensor Patch Enabling Ultralow Power Cuffless Blood Pressure Measurement. *Advanced Functional Materials*, 26(8):1178–1187, 2016. _eprint: https://onlinelibrary.wiley.com/doi/pdf/10.1002/adfm.201504560.

[35] Jie Qiu, Xiaohui Guo, Ran Chu, Siliang Wang, Wei Zeng, Lei Qu, Yunong Zhao, Feng Yan, and Guozhong Xing. Rapid-Response, Low Detection Limit, and High-Sensitivity Capacitive Flexible Tactile Sensor Based on Three-Dimensional Porous Dielectric Layer for Wearable Electronic Skin. *ACS Applied Materials & Interfaces*, 11(43):40716–40725, October 2019. Publisher: American Chemical Society.

[36] Bolun Li, Qi Tian, Hongxin Su, Xingwei Wang, Tianen Wang, and Dongzhi Zhang. High sensitivity portable capacitive humidity sensor based on In2O3 nanocubes-decorated GO nanosheets and its wearable application in respiration detection. *Sensors and Actuators B: Chemical*, 299:126973, November 2019.

[37] Gengrui Zhao, Yawen Zhang, Nan Shi, Zhirong Liu, Xiaodi Zhang, Mengqi Wu, Caofeng Pan, Hongliang Liu, Linlin Li, and Zhong Lin Wang. Transparent and stretchable triboelectric nanogenerator for self-powered tactile sensing. *Nano Energy*, 59:302–310, May 2019.

[38] He Zhang, Jiwei Zhang, Zhiwei Hu, Liwei Quan, Lin Shi, Jinkai Chen, Weipeng Xuan, Zhicheng Zhang, Shurong Dong, and Jikui Luo. Waist-wearable wireless respiration sensor based on triboelectric effect. *Nano Energy*, 59:75–83, May 2019.

[39] Guoquan Suo, Yanhao Yu, Zhiyi Zhang, Shifa Wang, Ping Zhao, Jianye Li, and Xudong Wang. Piezoelectric and Triboelectric Dual Effects in Mechanical-Energy Harvesting Using BaTiO $_3$ /Polydimethylsiloxane Composite Film. *ACS Applied Materials & Interfaces*, 8(50):34335–34341, December 2016.

[40] P. K. Panda. Review: environmental friendly lead-free piezoelectric materials. *Journal of Materials Science*, 44(19):5049–5062, July 2009.

[41] Hamza Lidjici, Farida Hobar, Mohamed Rguiti, Christian Courtois, and Anne Leriche. SOLID STATE SINTERING PREPARED 0. 935 (Bi 0. 5 Na 0. 5) TiO 3-0. 065 BaTiO 3 LEAD FREE CERAMICS: EFFECT OF POLING CONDITIONS. *Ceramics-Silikaty*, 56(1):36–39, 2012.

[42] X. Wang, J. Song, J. Liu, and Z. L. Wang. Direct-Current Nanogenerator Driven by Ultrasonic Waves. *Science*, 316(5821):102–105, April 2007.

[43] Guang Zhu, Rusen Yang, Sihong Wang, and Zhong Lin Wang. Flexible High-Output Nanogenerator Based on Lateral ZnO Nanowire Array. *Nano Letters*, 10(8):3151–3155, August 2010.

[44] S. Tadigadapa and K. Mateti. Piezoelectric MEMS sensors: state-of-the-art and perspectives. *Measurement Science and Technology*, 20(9):092001, September 2009.

[45] Jun Zhou, Yudong Gu, Peng Fei, Wenjie Mai, Yifan Gao, Rusen Yang, Gang Bao, and Zhong Lin Wang. Flexible Piezotronic Strain Sensor. *Nano Letters*, 8(9):3035–3040, September 2008.

[46] Shujun Zhang, Fei Li, Xiaoning Jiang, Jinwook Kim, Jun Luo, and Xuecang Geng. Advantages and Challenges of Relaxor-PbTiO3 Ferroelectric Crystals for Electroacoustic Transducers- A Review. *Progress in Materials Science*, 68:1–66, March 2015.

[47] Qifa Zhou, Sienting Lau, Dawei Wu, and K. Kirk Shung. Piezoelectric films for high frequency ultrasonic transducers in biomedical applications. *Progress in materials science*, 56(2):139–174, February 2011.

[48] A. Morelli, F. Johann, N. Schammelt, and I. Vrejoiu. Ferroelectric nanostructures fabricated by focused-ion-beam milling in epitaxial $BiFeO_3$ thin films. *Nanotechnology*, 22(26):265303, July 2011.

[49] M. Alexe, C. Harnagea, D. Hesse, and U. Gösele. Patterning and switching of nanosize ferroelectric memory cells. *Applied Physics Letters*, 75(12):1793, 1999.

[50] C. S. Ganpule, A. Stanishevsky, S. Aggarwal, J. Melngailis, E. Williams, R. Ramesh, V. Joshi, and Carlos Paz de Araujo. Scaling of ferroelectric and piezoelectric properties in Pt/SrBi2Ta2O9/Pt thin films. *Applied Physics Letters*, 75(24):3874, 1999.

[51] Heiji Kawai. The Piezoelectricity of Poly (vinylidene Fluoride). *Japanese Journal of Applied Physics*, 8(7):975–976, July 1969.

[52] K. Park, Soo Bin Bae, S. H. Yang, H. Lee, Kisu Lee, and S. Lee. Lead-free batio3 nanowires-based flexible nanocomposite generator. *Nanoscale*, 6 15:8962–8, 2014.

[53] F. Levassort, M. Lethiecq, R. Desmare, and Tran-Huu-Hue. Effective electroelastic moduli of 3-3(0-3) piezocomposites. *IEEE Transactions on Ultrasonics, Ferroelectrics, and Frequency Control*, 46(4):1028–1034, July 1999.

[54] K. Prashanthi, N. Miriyala, R. D. Gaikwad, W. Moussa, V. Ramgopal Rao, and T. Thundat. Vibtrational energy harvesting using photo-patternable piezoelectric nanocomposite cantilevers. *Nano Energy*, 2(5):923 – 932, 2013.

[55] Nagamalleswara Rao Alluri, Balasubramaniam Saravanakumar, and Sang-Jae Kim. Flexible, Hybrid Piezoelectric Film (BaTi(1–x)ZrxO3)/PVDF Nanogenerator as a Self-Powered Fluid Velocity Sensor. *ACS Applied Materials & Interfaces*, 7(18):9831–9840, May 2015.

[56] Kwi-Il Park, Minbaek Lee, Ying Liu, San Moon, Geon-Tae Hwang, Guang Zhu, Ji Eun Kim, Sang Ouk Kim, Do Kyung Kim, Zhong Lin Wang, and Keon Jae Lee. Flexible nanocomposite generator made of batio3 nanoparticles and graphitic carbons. *Advanced Materials*, 24(22):2999–3004, 2012.

[57] Van Son Nguyen, Didier Rouxel, Brice Vincent, Laurent Badie, Fabrice Domingues Dos Santos, Emmanuel Lamouroux, and Yves Fort. Influence of cluster size and surface functionalization of ZnO nanoparticles on the morphology, thermomechanical and piezoelectric

properties of P(VDF-TrFE) nanocomposite films. *Applied Surface Science*, 279:204 – 211, 2013.

[58] Sara Dalle Vacche, Fabiane Oliveira, Yves Leterrier, Véronique Michaud, Dragan Damjanovic, and Jan-Anders E. Månson. Effect of silane coupling agent on the morphology, structure, and properties of poly(vinylidene fluoride–trifluoroethylene)/BaTiO3 composites. *Journal of Materials Science*, 49(13):4552–4564, July 2014.

[59] Kanguk Kim, Wei Zhu, Xin Qu, Chase Aaronson, William R. McCall, Shaochen Chen, and Donald J. Sirbuly. 3D Optical Printing of Piezoelectric Nanoparticle–Polymer Composite Materials. *ACS Nano*, 8(10):9799–9806, October 2014.

[60] Muhammed A. Al-Nasassrah, Fridrun Podczeck, and J. Michael Newton. The effect of an increase in chain length on the mechanical properties of polyethylene glycols. *European journal of pharmaceutics and biopharmaceutics*, 46(1):31–38, 1998.

[61] Hyun-Wook Lee, San Moon, Chang-Hak Choi, and Do Kyung Kim. Synthesis and Size Control of Tetragonal Barium Titanate Nanopowders by Facile Solvothermal Method. *Journal of the American Ceramic Society*, 95(8):2429–2434, August 2012.

[62] Minhui Du and Ying Zheng. Modification of silica nanoparticles and their application in UDMA dental polymeric composites. *Polymer Composites*, 28(2):198–207, April 2007.

[63] Shiva Adireddy, Cuikun Lin, Baobao Cao, Weilie Zhou, and Gabriel Caruntu. Solution-Based Growth of Monodisperse Cube-Like BaTiO $_3$ Colloidal Nanocrystals. *Chemistry of Materials*, 22(6):1946–1948, March 2010.

[64] Maarten Bloemen, Ward Brullot, Tai Thien Luong, Nick Geukens, Ann Gils, and Thierry Verbiest. Improved functionalization of oleic acid-coated iron oxide nanoparticles for biomedical applications. *Journal of Nanoparticle Research*, 14(9), September 2012.

[65] Kanguk Kim, James L. Middlebrook, Jeffrey E. Chen, Wei Zhu, Shaochen Chen, and Donald J. Sirbuly. Tunable Surface and Matrix Chemistries in Optically Printed (0–3) Piezoelectric Nanocomposites. *ACS Applied Materials & Interfaces*, 8(49):33394–33398, December 2016.

[66] William R. McCall, Kanguk Kim, Cory Heath, Gina La Pierre, and Donald J. Sirbuly. Piezoelectric Nanoparticle–Polymer Composite Foams. *ACS Applied Materials & Interfaces*, 6(22):19504–19509, November 2014.

[67] Donald J. Sirbuly, William McCall, and Kanguk Kim. "piezoelectric nanoparticle-polymer composite structure," u.s. patent 20160181506a1, June 2016.

[68] Guangzu Zhang, Peng Zhao, Xiaoshan Zhang, Kuo Han, Tiankai Zhao, Yong Zhang, Chang Kyu Jeong, Shenglin Jiang, Sulin Zhang, and Qing Wang. Flexible three-dimensional interconnected piezoelectric ceramic foam based composites for highly efficient concurrent mechanical and thermal energy harvesting. *Energy & Environmental Science*, 11(8):2046–2056, 2018.

[69] Grand View Research. Wearable Technology Market Size | Industry Report, 2020-2027, June 2020.

[70] X. Q. Fang, Q. Yang, J. X. Liu, and W. J. Feng. Surface/interface effect around a piezoelectric nano-particle in a polymer matrix under compressional waves. *Applied Physics Letters*, 100(15):151602, April 2012.

[71] Dong S. Huh and Stuart L. Cooper. Dynamic mechanical properties of polyurethane block polymers. *Polymer Engineering & Science*, 11(5):369–376, 1971.

[72] Valeriy V. Ginzburg, Jozef Bicerano, Christopher P. Christenson, Alan K. Schrock, and Alexander Z. Patashinski. Theoretical modeling of the relationship between Young's modulus and formulation variables for segmented polyurethanes. *Journal of Polymer Science Part B: Polymer Physics*, 45(16):2123–2135, 2007. _eprint: https://onlinelibrary.wiley.com/doi/pdf/10.1002/polb.21213.

[73] K. S. Challagulla and T. A. Venkatesh. Computational Modeling of Piezoelectric Foams. *JOM*, 65(2):256–266, February 2013.

[74] Limin Huang, Zhuoying Chen, James Wilson, Sarbajit Banerjee, Richard Robinson, Irving Herman, Robert Laibowitz, and Stephen O'Brien. Barium titanate nanocrystals and nanocrystal thin films: Synthesis, ferroelectricity, and dielectric properties. *Journal of Applied Physics*, 100:034316/1–034316/10, 08 2006.

[75] Alexander Russell. XX. *The dielectric strength of air*. *The London, Edinburgh, and Dublin Philosophical Magazine and Journal of Science*, 11(62):237–276, February 1906.

[76] Hyeung Gyu Lee, Ji Hyun Choi, and Eung Soo Kim. Low-temperature sintering and electrical properties of (1- x) pb (zr 0.5 ti 0.5) o 3-xpb (cu 0.33 nb 0.67) o 3 ceramics. *Journal of electroceramics*, 17(2-4):1035–1040, 2006.

[77] A. Tirella, G. Mattei, and A. Ahluwalia. Strain rate viscoelastic analysis of soft and highly hydrated biomaterials. *Journal of Biomedical Materials Research Part A*, 102(10):3352–3360, October 2014.

[78] Amnah S. Khan and William G. Proud. Temperature and strain rate effects on the piezoelectric charge production of PZT 95/5. *AIP Conference Proceedings*, 1793(1):100037, January 2017. Publisher: American Institute of Physics.

[79] R. Panciroli and M. Porfiri. Hydroelastic impact of piezoelectric structures. *International Journal of Impact Engineering*, 66:18–27, April 2014.

[80] Clive R. Siviour and Jennifer L. Jordan. High Strain Rate Mechanics of Polymers: A Review. *Journal of Dynamic Behavior of Materials*, 2(1):15–32, March 2016.

[81] George C. Jacob, J. Michael Starbuck, John F. Fellers, Srdan Simunovic, and Raymond G. Boeman. Strain rate effects on the mechanical properties of polymer composite materials. *Journal of Applied Polymer Science*, 94(1):296–301, September 2004.

[82] IEEE. IEEE Standard on Piezoelectricity. *ANSI/IEEE Std 176-1987*, pages 1–66, 1988.

[83] Ruibin Liu, Qiming Zhang, and L. E. Cross. Experimental investigation of electrostrictive polarization biased direct apparent piezoelectric properties in polyurethane elastomer under quasistatic conditions. *Journal of Applied Polymer Science*, 73(13):2603–2609, 1999.

[84] Qing Guo, G. Z. Cao, and I. Y. Shen. Measurements of piezoelectric coefficient d33 of lead zirconate titanate thin films using a mini force hammer. *Journal of Vibration and Acoustics*, 135(1), 2013.

[85] Morito Akiyama, Yukari Morofuji, Toshihiro Kamohara, Keiko Nishikubo, Masayoshi Tsubai, Osamu Fukuda, and Naohiro Ueno. Flexible piezoelectric pressure sensors using oriented aluminum nitride thin films prepared on polyethylene terephthalate films. *Journal of Applied Physics*, 100(11):114318, 2006.

[86] Hong-Jie Tseng, Wei-Cheng Tian, and Wen-Jong Wu. Flexible PZT Thin Film Tactile Sensor for Biomedical Monitoring. *Sensors*, 13(5):5478–5492, April 2013.

[87] Arun K. Ramanathan, Leon M. Headings, and Marcelo J. Dapino. Near static strain measurement with piezoelectric films. *Sensors and Actuators A: Physical*, 301:111654, January 2020.

[88] M. B. Suresh, Tsung-Her Yeh, Chih-Chieh Yu, and Chen-Chia Chou. Dielectric and ferroelectric properties of polyvinylidene fluoride (pvdf)-pb0.52zr0.48tio3 (pzt) nano composite films. *Ferroelectrics*, 381(1):80–86, 2009.

[89] Gustav Gautschi. *Piezoelectric sensoronics: force, strain, pressure, acceleration and acoustic emission sensors, mateirlas and amplifiers*. Springer-Verlag, Berlin, Germany, 2002.

[90] Yosua Hamonangan and Wigajatri Purnamaningsih. Heartbeat detection system using piezoelectric transducer. *AIP Conference Proceedings*, 1817(1):040016, February 2017.

[91] SeungNam Cha, Seong Min Kim, HyunJin Kim, JiYeon Ku, Jung Inn Sohn, Young Jun Park, Byong Gwon Song, Myoung Hoon Jung, Eun Kyung Lee, Byoung Lyong Choi, Jong Jin Park, Zhong Lin Wang, Jong Min Kim, and Kinam Kim. Porous PVDF As Effective Sonic Wave Driven Nanogenerators. *Nano Letters*, 11(12):5142–5147, December 2011.

[92] Jesse T. McCann, Jennifer I.L. Chen, Dan Li, Zuo-Guang Ye, and Younan Xia. Electrospinning of polycrystalline barium titanate nanofibers with controllable morphology and alignment. *Chemical Physics Letters*, 424(1-3):162–166, June 2006.

[93] Sung Bum Kang, Sang Hyuk Won, Min Ji Im, Chan Ul Kim, Won Il Park, Jeong Min Baik, and Kyoung Jin Choi. Enhanced piezoresponse of highly aligned electrospun poly(vinylidene fluoride) nanofibers. *Nanotechnology*, 28(39):395402, September 2017.

[94] Long Lin, Yannan Xie, Simiao Niu, Sihong Wang, Po-Kang Yang, and Zhong Lin Wang. Robust Triboelectric Nanogenerator Based on Rolling Electrification and Electrostatic Induction at an Instantaneous Energy Conversion Efficiency of 55%. *ACS Nano*, 9(1):922–930, January 2015.

[95] Paymon Shirazi, Gerardo Ico, Christopher S. Anderson, Meghann C. Ma, Bum Sung Kim, Jin Nam, and Nosang V. Myung. Size-Dependent Piezoelectric Properties of Electrospun $BaTiO_3$ for Enhanced Energy Harvesting. *Advanced Sustainable Systems*, 1(11):1700091, November 2017.

[96] Darren J. Lipomi, Michael Vosgueritchian, Benjamin C-K. Tee, Sondra L. Hellstrom, Jennifer A. Lee, Courtney H. Fox, and Zhenan Bao. Skin-like pressure and strain sensors based on transparent elastic films of carbon nanotubes. *Nature Nanotechnology*, 6(12):788–792, December 2011.

[97] Momentive. Technical Data Sheet, RTV100 Series, September 2020.

[98] ChaBum Lee and Joshua A Tarbutton. Electric poling-assisted additive manufacturing process for PVDF polymer-based piezoelectric device applications. *Smart Materials and Structures*, 23(9):095044, September 2014.

[99] Chieh Chang, Van H. Tran, Junbo Wang, Yiin-Kuen Fuh, and Liwei Lin. Direct-Write Piezoelectric Polymeric Nanogenerator with High Energy Conversion Efficiency. *Nano Letters*, 10(2):726–731, February 2010.

[100] Yung Ting, Hariyanto Gunawan, Amelia Sugondo, and Chun-Wei Chiu. A New Approach of Polyvinylidene Fluoride (PVDF) Poling Method for Higher Electric Response. *Ferroelectrics*, 446(1):28–38, January 2013.

[101] Rui Li, Zhenhua Zhao, Zixuan Chen, and Jianzhong Pei. Novel BaTiO3/PVDF composites with enhanced electrical properties modified by calcined BaTiO3 ceramic powders. *Materials Express*, 7(6):536–540, December 2017.

[102] H. L.W. Chan, M. C. Cheung, and C. L. Choy. Study on $BaTiO_3$ /P(VDF-TrFE) 0–3 composites. *Ferroelectrics*, 224(1):113–120, March 1999.

[103] US Research Nanomaterials Inc. Barium Titanate BaTiO3 Nanopowder / Nanoparticles (BaTiO3, 99.9%, 200nm, Tetragonal).

[104] Hiromichi Hayashi, Takashi Nakamura, and Takeo Ebina. In-situ Raman spectroscopy of BaTiO3 particles for tetragonal–cubic transformation. *Journal of Physics and Chemistry of Solids*, 74(7):957–962, July 2013.